$BiVO_4$-Based Nanoparticles for Visible Light Photocatalytic Applications

HAN Mandi

School of Electrical & Electronics Engineering

A thesis submitted to the Nanyang Technological University
in partial fulfillment of the requirement for the degree of
Doctor of Philosophy

2013

Statement of Originality

I hereby certify that the work embodied in this thesis is the result of original research and has not been submitted for a higher degree to any other University or Institution.

Date

Han Mandi

Abstract

In recent years, clean renewable energy and sustainable environment are emerging as the top issues and challenges for humanity. Photocatalysis can be applied to convert solar energy into chemical energy, and is considered as an attractive strategy to tackle the environmental and energy challenges. Since the traditional photocatalyst TiO_2 is limited in ultraviolet (UV) range applications, alternative materials have been widely explored. Among them, $BiVO_4$ has shown great potential to extend beyond the UV region due to its suitable band-gap of 2.4 eV and favorable band edge alignment to water splitting. In this work, monoclinic *m*-$BiVO_4$ nanoparticles were synthesized and surface-modified in order to improve the photocatalytic property.

The present work started from the mechanism study of *m*-$BiVO_4$ synthesis. It was found that a $pH \leq 9$ was essential in the phase formation. Owing to the different reaction mechanisms involved under various pH conditions, the state and morphology of the Bi-precursor played a crucial role in determining the particle size and morphology of the synthesized product. In addition, the photocatalytic activity of these *m*-$BiVO_4$ powders was found to be greatly influenced by both the specific surface area and local structure variation. Synthesis in acid solution was found to benefit complete crystallization with large distortion of the VO_4^{3-} tetrahedron in the local structure, and the product exhibited the highest photocatalytic activity.

In strong acid condition and with the presence of sodium dodecyl benzene sulfonate (SDBS), *m*-$BiVO_4$ octahedral single crystals were successfully obtained with sizes adjustable in a broad range from 200 nm to 5 μm. The influences of SDBS addition, reaction time, and acid concentration were studied while the products were extensively characterized to discover the crystal growth mechanism, which was proposed as a supersaturation process followed by the Ostwald ripening. Compared with irregular shaped particles, these octahedral crystals showed superior visible-light photocatalytic performance.

Further, γ-Bi_2O_3, the best photocatalytic polymorph of Bi_2O_3, was formed on the surface of *m*-$BiVO_4$ octahedral crystals through an alkaline "etching" process. The product resulted in *m*-$BiVO_4$@γ-Bi_2O_3 core-shell heterostructure with p-n junction formation. It was found that such formation and yield of Bi_2O_3 was determined by both the alkaline concentration and reaction time. Moreover, the effect of Bi_2O_3 formation on the specific surface area of the composite particles was investigated. The RhB degradation test indicated that a 34% γ–Bi_2O_3 composite phase provided the highest improvement of photocatalytic performance, which was attributed to a higher specific surface area and improved charge carrier transfer in the p-n heterojunction structure.

In parallel, based on the photocatalytic capability of *m*-$BiVO_4$, Au or Pt nanoparticles were successfully synthesized and loaded onto the surface of the *m*-$BiVO_4$ nanocrystals, as evidenced by extensive characterization. Suitably loaded Au- and Pt-$BiVO_4$ heterogeneous nanoparticles exhibited much higher visible-light photocatalytic activities than the pure *m*-$BiVO_4$ crystals. Further study and comparison between Au and Pt loading revealed that the superior photocatalytic activity of Pt/*m*-$BiVO_4$ composite nanoparticles lied in the better dispersion of Pt nanoparticles, while Au-loading resulted in severe particle agglomeration that decrease the specific surface area. Finally, as a combination of the achievements in the p-n composite formation and Pt nanoparticles loading, *m*-$BiVO_4$/γ-Bi_2O_3/Pt multi-composite nanoparticles were synthesized, which could further improve the photocatalytic performance.

Acknowledgement

I would like to give my sincere acknowledgements to my supervisor, Prof. Tan Ooi Kiang, for his valuable guidance and great support for my project. I would also like to express my deep thanks to Prof. Tse Man Siu, Dr. Chen Xiaofeng and Dr. Huang Hui for their detailed guidance, helpful discussions and valuable advices.

Thanks to my group mates Dr. Leiw Ming Yian, Dr. Zhang Li, Dr. Fang Xiaoqin, Ms. Tan Pei Yun, Ms. Luo Qiong, Dr. Chow Chee Lap, Dr. Lim Chiew Keat, Dr. Chua Chin Sheng for their kind cooperation and useful discussion. Thanks to Mr. Chua Tong Sun, Mr. Ng Yong Chiang and all technicians in microelectronics division for equipment training and safety assistance.

Last but not the least, I would like to thank my husband, Dr. Sun Ting. Thanks for not only being with me all the time, but also helping me on the data analysis. I am also grateful to my parents, my daughter and all my friends for their warm encouragement.

Table of Contents

Statement of Originality i

Abstract ii

Acknowledgement iv

Table of Contents v

List of Figures viii

List of Tables xiv

Chapter 1. Introduction 1

- 1.1 Motivation 1
- 1.2 Objectives 2
- 1.3 Major Contribution of the Thesis 3
- 1.4 Organization of the thesis 5

Chapter 2. Literature Review 7

- 2.1 Photocatalytic Reaction 7
- 2.2 Photocatalytic Materials 9
  - 2.2.1 Historical overview 9
  - 2.2.2 Titanium Dioxide, TiO_2 10
  - 2.2.3 Zinc Oxide, ZnO 12
  - 2.2.4 Cadmium sulfide, CdS, and Cadmium Selenide, CdSe 12
  - 2.2.5 Strontium Titanate, $SrTiO_3$ 12
- 2.3 $BiVO_4$ for Visible light Photocatalysis 14
  - 2.3.1 Visible light induced photocatalysis 14
  - 2.3.2 Bismuth vanadate ($BiVO_4$) 16

2.3.3 Approaches to enhance the photocatalytic performance 19

2.3.4 Strategies to enhance the charge separation in $BiVO_4$ 21

2.4 Summary 24

Chapter 3. Experimental Methods 25

3.1 Sample Fabrication 25

3.2 Characterization 26

3.3 Photocatalytic tests 29

Chapter 4. PH-directed $BiVO_4$ Synthesis Mechanism and Product Morphology 31

4.1 Introduction 31

4.2 The crystalline structure of $BiVO_4$ 32

4.3 The morphologies of $BiVO_4$ 33

4.4 The photo-physical properties of $BiVO_4$ 38

4.5 Concluding remarks 43

Chapter 5. Mono-Dispersed *m*-$BiVO_4$ Octahedral Single Crystals 44

5.1 Introduction 44

5.2 The crystalline structure of m-$BiVO_4$ 45

5.3 The morphologies of m-$BiVO_4$ 47

5.4 The photo-physical properties of m-$BiVO_4$ 55

5.5 Concluding remarks 59

Chapter 6. *m*-$BiVO_4$@γ-Bi_2O_3 Composite with Core-Shell Heterogeneous Structure . 60

6.1 Introduction 60

6.2 Synthesis of m-$BiVO_4$@γ-Bi_2O_3 composite 62

6.3 Crystal phase of m-$BiVO_4$@γ-Bi_2O_3 composite 63

6.4 Morphology of m-$BiVO_4$@γ-Bi_2O_3 composite 64

6.5 Photo-absorption of m-$BiVO_4$@γ-Bi_2O_3 composite 72

6.6 Mechanism of enhanced charge carrier transfer 77

6.7 Concluding remarks 82

Chapter 7. Surface Modification of *m*-$BiVO_4$ crystals by loading Au and Pt 83

7.1 Introduction 83

7.2 Synthesis of Au (or Pt)/m-$BiVO_4$ nanoparticles 84

7.3 Characterization of Au/m-$BiVO_4$ nanoparticles 86

7.4 Photo-physical properties of Au/m-$BiVO_4$ 89

7.5 Enhance mechanism of metal loading 93

7.6 Synthesis and Characterization of Pt/m-$BiVO_4$ 96

7.7 The photo-physical properties of Pt/m-$BiVO_4$ 100

7.8 Comparison of Au- and Pt-loading 103

7.9 m-$BiVO_4$/γ-Bi_2O_3/Pt composite 106

7.10 Concluding remarks 110

Chapter 8. Conclusions and future work 112

8.1 Conclusions 112

8.2 Recommended future work 115

8.2.1 Synthesis-scale-up of *m*-$BiVO_4$ octahedral nano-crystals 115

8.2.2 Preliminary development of *m*-$BiVO_4$ film 119

8.2.3 Magnetization of *m*-$BiVO_4$ octahedral nanocrystals for recycling 124

8.2.4 Other morphologies of *m*-$BiVO_4$ nanoparticles 124

Publication List 126

References 127

List of Figures

Figure 2.1 photocatalytic reaction; generation and recombination of electron-hole pair and redox reactions [22]. 7

Figure 2.2 Ideal ABO_3 perovskite structure. The BO_6 octahedron links through corners to form a three-dimensional cubic lattice, and the A cation is in the center of the cube [51]. 14

Figure 2.3 (a) optical absorption spectra of $TiO_{2-x}N_x$ and TiO_2 films and (b) N1s XPS spectra of TiO_2 and $TiO_{2-x}N_x$ films [3]. 15

Figure 2.4 Various schemes illustrating the possible band-gap electronic structure and excitation processes of visible light responsive TiO_2 materials [59]........ 16

Figure 2.5 Schematic representation of (a) monoclinic scheelite structure, (b) tetragonal scheelite structure and (c) tetragonal zircon structure. 17

Figure 2.6 Mechanisms in heterostructured photocatalytic materials [81]. 20

Figure 2.7 Charge transfer mechanisms in composite photocatalytic materials with p-n junction formation [99]........ 23

Figure 3.1 Synthesis procedure of BVO_4 crystals by hydrothermal method. 26

Figure 3.2 Overview of the Kelvin probe system (from KP Technology). 28

Figure 4.1 XRD patterns of the as-prepared samples (a) BVO-0, (b) BVO-3, (c) BVO-5, (d) BVO-7, (e) BVO-9, (f) BVO-11 and (g) BVO-12........ 33

Figure 4.2 SEM images of as-prepared *m*-$BiVO_4$ powders (a) BVO-0, (b) BVO-3, (c) BVO-5, (d) BVO-7 and (e) BVO-9. 35

Figure 4.3 SEM images of different Bi-precursors (a) $BiONO_3$ pH = 5 (b) $Bi(OH)_3$-based complex in pH = 9. 37

Figure 4.4 Schematic illustration on the formation mechanism of the *m*-$BiVO_4$ particles in the solution with different pH values. 38

Figure 4.5 The photocatalytic degradation of RhB for as-prepared *m*-$BiVO_4$ samples. 39

Figure 4.6 (a) UV-Vis diffused reflectance spectra and (b) plots of $(\alpha h\nu)^2$ versus photon energy ($h\nu$) of the as-prepared $BiVO_4$ samples. 40

Figure 4.7 (a) Raman spectra and (b) the dependence of the RhB degradation efficiency on stretching Raman shift V–O bonds of as-prepared *m*-$BiVO_4$ samples. 42

Figure 5.1 Typical XRD pattern of *m*-$BiVO_4$ as-prepared nano-particles. The insets are zoomed XRD patterns near 19º and 35º, respectively. 46

Figure 5.2 (a) low-magnification, (b) high-magnification FESEM image and (d) EDX spectrum of the as-prepared *m*-$BiVO_4$ octahedral single crystals compared with (c) and (d) the SEM image of the sample synthesized without SDBS.. 47

Figure 5.3 (a), (c) and (e) TEM images of as-prepared single-crystalline *m*-$BiVO_4$ octahedra, with the insets showing the corresponding SEAD patterns observed along different zone axes. The HRTEM images (b), (d) and (f) were taken from the crystal edge in Figure 5.2 (a), (c) and (e), respectively, with the insets giving the schematic illustrations of the octahedra with the corresponding angles.. 49

Figure 5.4 Schematic illustration of the crystal orientation of the *m*-$BiVO_4$ octahedron with specific facets. 50

Figure 5.5 SEM images of the *m*-$BiVO_4$ crystals synthesized at different reaction times with fixed acid concentration 1.2 M (a) 6 h, (b) 12 h, (c) 24 h, & (d) 48 h........ 51

Figure 5.6 Schematic illustration of the proposed growth evolution of an *m*-$BiVO_4$ octahedron... 53

Figure 5.7 SEM images of different acid concentration (fixed reaction time 24 h): (a) 1.5 M, (b) 1.2 M, (c) 1 M, (d) 0.8 M and (e) pH = 2. 54

Figure 5.8 (a) The photocatalytic degradation of RhB for *m*-$BiVO_4$ octahedral crystals and (b) First-order plots for the photocatalytic degradation of RhB by samples S1~S4 showing the linear relationship. 56

Figure 5.9 (a) UV-Vis diffused reflectance spectra and (b) plots of $(\alpha h\nu)^2$ versus photon energy ($h\nu$) of the as-prepared *m*-$BiVO_4$ octahedral crystals. 58

Figure 5.10 The repeated photocatalytic degradation of RhB for the recollected *m*-$BiVO_4$ octahedral crystals after the first test. 58

Figure 6.1 Synthesis procedure of *m*-$BiVO_4$@γ-Bi_2O_3 composites. 62

Figure 6.2 XRD patterns of the as-prepared samples. (a) BB01 (0.1M/6h), (b) BB02 (0.2M/3h), (c) BB03 (0.2M/6h), (d) BB04 (0.3M/6h) and (e) BB05 (0.2M/10h). 64

Figure 6.3 SEM images of as-prepared *m*-$BiVO_4$@γ-Bi_2O_3 composite particles with different reaction durations, (a) & (b) 0 h pure *m*-$BiVO_4$, (c) & (d) 3 h BB02, (e) & (f) 6 h BB03, (g) & (h) 10 h BB05. 65

Figure 6.4 SEM images of as-prepared *m*-$BiVO_4$@γ-Bi_2O_3 composite particles fabricated under different alkaline concentrations, (a) & (b) 0.1 M BB01, (c) & (d) 0.2 M BB03, (e) & (f) 0.3 M BB04. 66

Figure 6.5 (a) TEM image, (b) the corresponding SAED pattern, (e) EDX-line scan and (f) HR-TEM image of *m*-$BiVO_4$@γ-Bi_2O_3 composite BB03, with (c) TEM image and (d) its corresponding SAED pattern of a pure *m*-$BiVO_4$ octahedral single crystal as comparison. 68

Figure 6.6 Crystal structure comparison between (a) cubic γ-Bi_2O_3 and (b) monoclinic scheelite $BiVO_4$. 69

Figure 6.7 Schematic illustration of the surface reaction mechanism and morphology evolution of *m*-$BiVO_4$@γ-Bi_2O_3 core-shell heterostructure. 72

Figure 6.8 UV-Vis diffused reflectance spectra of the as-prepared *m*-$BiVO_4$@γ-Bi_2O_3 composite samples. 72

Figure 6.9 Photocatalytic degradation of RhB for the as-prepared *m*-$BiVO_4$@γ-Bi_2O_3 composite samples. 74

Figure 6.10 XRD patterns of the samples (a) BB02 and (b) BB03 before (lower black) and after (upper red) photocatalytic test in the degradation of RhB. 76

Figure 6.11 the repeated photocatalytic test of the samples BB02 and BB03 in the degradation of RhB. 77

Figure 6.12 Schematic illustrations of the energy band structures (a) for separate phases and (b) after the formation of *m*-$BiVO_4$@γ-Bi_2O_3 p-n hetero junction. . 79

Figure 6.13 Transient SPV spectra of (a) pure *m*-$BiVO_4$ and (b) BB03, and (c) the comparison of average SPV values under different working current. 80

Figure 6.14 Transient SPV spectra of (a) pure *m*-$BiVO_4$ and (b) BB03 after irradiation turned off. 81

Figure 7.1 (a) schematic illustration of Au particle formation on the surface of *m*-$BiVO_4$ crystals and (b) synthesis procedure of Au (or Pt)/*m*-$BiVO_4$ nanoparticles. 84

Figure 7.2 XRD patterns of the as-prepared Au/*m*-$BiVO_4$ nanoparticles. 86

Figure 7.3 (a) low and (b) high magnification SEM images of Au4.0%. 88

Figure 7.4 TEM image of a composite nanocrystal in Au4.0% with elemental mapping under STEM-EDX. 88

Figure 7.5 (a) XPS full scan spectrum of Au4.0% with (b), (c) and (d) fine scan spectra on main elements. 89

Figure 7.6 UV-Vis diffused reflectance spectra of the as prepared pure and Au-loaded *m*-$BiVO_4$ nanoparticles. 90

Figure 7.7 (a) The photocatalytic degradation of RhB and (b) 12-h degradation efficiency of the An/*m*-$BiVO_4$ composite samples. 92

Figure 7.8 (a) SEM image and (b) EDX spectrum of Au 8.0% derived from the marked point in (a), which indicated significant agglomeration by heavy Au-loading. 93

Figure 7.9 Schematic illustration of (a) the Schottky barrier between *m*-$BiVO_4$ and Au and (b) the enhanced separation of electron-hole pair at the interface 94

Figure 7.10 Photoluminescence (PL) spectra of Au/*m*-$BiVO_4$ nanoparticles 95

Figure 7.11 XRD patterns of the as-prepared Pt/*m*-$BiVO_4$ nanoparticles. 97

Figure 7.12 (a) Low and (b) high magnification SEM images of Pt2.0%. 98

Figure 7.13 (a) TEM image and (b) STEM line scan analysis of a Pt/*m*-$BiVO_4$ composite crystal in Pt2.0%. 99

Figure 7.14 (a) XPS full scan spectrum of Pt2.0% with (b), (c) and (d) fine scan spectra on main elements. 99

Figure 7.15 UV-Vis diffused reflectance spectra of the as prepared pure and Pt-loaded *m*-$BiVO_4$ nanoparticles. 100

Figure 7.16 The photocatalytic degradation of RhB for as-prepared Pt/*m*-$BiVO_4$ composite samples. 101

Figure 7.17 Photoluminescence (PL) spectra of Pt/*m*- $BiVO_4$ nanoparticles. 102

Figure 7.18 Comparison between Au- and Pt-loading on *m*-$BiVO_4$ crystals in (a) the photocatalytic degradation of RhB along irradiation time, (b) the photocatalytic enhancement in terms of degradation efficiency and (c) the influences on specific surface area. 104

Figure 7.19 SEM mapping results of Au1.0% (up) and Pt1.0% (down) composite nanoparticles. 105

Figure 7.20 XRD patterns of the as-prepared m-$BiVO_4$/γ-Bi_2O_3/Pt composite nanoparticles. 107

Figure 7.21 STEM image and EDX line scan on one of the *m*-$BiVO_4$/γ-Bi_2O_3/Pt composite nanoparticles........ 108

Figure 7.22 Schematic illustration on the synthesis route and the morphology evolution of the *m*-$BiVO_4$/γ-Bi_2O_3/Pt composite nanoparticles. 109

Figure 7.23 The photocatalytic degradation of RhB for as-prepared m-$BiVO_4$/γ-Bi_2O_3/Pt composite nanoparticles. 110

Figure 8.1 Schematic illustration of (a) the setup and (b) the procedure of the scale-up synthesis of *m*-$BiVO_4$ octahedral nanocrystals........ 116

Figure 8.2 XRD pattern of as-prepared *m*-$BiVO_4$ nanoparticles by the scale-up open system synthesis. 117

Figure 8.3 Typical SEM image of as-prepared *m*-$BiVO_4$ octahedral nanocrystals by the scale-up open system synthesis. 117

Figure 8.4 Comparison of particle size distribution of *m*-$BiVO_4$ nanocrystals between (a) hydrothermal synthesis and (b) scale-up in open-system........ 118

Figure 8.5 Schematic illustration and procedure of *m*-BVO_4 film preparation by hydrothermal chemical bath deposition. 120

Figure 8.6 XRD pattern of *m*-BVO_4 thin film on FTO substrate........ 121

Figure 8.7 (a) low and (b) high magnification SEM images of *m*-BVO_4 thin film on FTO substrate........ 121

List of Tables

Table 2.1 Properties of bulk TiO_2 and its different phases [40]. 11

Table 4.1 Sample name, the solution pH values in corresponding synthesis and resultant crystal phase of the as-prepared *m*-$BiVO_4$ powder samples. 32

Table 4.2 Band gap energies, BET surface area values, Stretching Raman shift V–O bonds, RhB degradation efficiencies after 24 hours and particle morphologies of the as-prepared *m*-$BiVO_4$ powder samples. 38

Table 5.1 Specific surface area, photocatalytic reaction constant k and band gap energy of the samples according to the crystal sizes. 55

Table 6.1 List of sample name, composition, and orthogonal experiment details of the as-prepared *m*-$BiVO_4$@γ-Bi_2O_3 composite samples. 63

Table 6.2 Comparison of crystal structure and lattice mismatch from *m*-$BiVO_4$ of various Bi_2O_3 polymorphs. 70

Table 6.3 Degradation efficiencies of RhB after 10 hours and specific surface area of the as-prepared *m*-$BiVO_4$@γ-Bi_2O_3 composite samples. 75

Table 6.4 Absolute electronegativity, estimated band gap, calculated energy levels of conduction band edge and valence band edge at the zero-charge point for *m*-$BiVO_4$ and γ-Bi_2O_3. 78

Table 7.1 List of sample name, molecular percentage of metal (M = Au, Pt) precursors and resultant weight percentage of metal of the as-prepared M/*m*-$BiVO_4$ nanoparticles. 85

Table 7.2 RhB degradation efficiencies after 12 hours irradiation and specific surface area (BET) of the as-prepared Au/*m*-$BiVO_4$ composite samples. 91

Table 7.3 RhB degradation efficiencies after 10 hours irradiation (12 hours for pure *m*-$BiVO_4$) and specific surface area (BET) of the as-prepared Pt/*m*-$BiVO_4$ composite samples. 101

Chapter 1. Introduction

1.1 Motivation

Nano-materials have been extensively explored due to their attractive chemical and physical properties for potential applications to overcome the energy and environmental problems, which are considered as one of the greatest challenges in the 21st century. Since the photoelectrochemical water splitting (the Honda-Fujishima-effect) was reported in 1972 [1], TiO_2 has become the most widely used semiconductor in photocatalysis for environmental and energy applications. It has many advantageous properties including being highly oxidative, chemically stable, inexpensive and non-toxic. However, because of its large band gap energy around 3.2 eV, TiO_2 can only be excited by UV light, which constitutes only 4% of the solar spectrum [2]. Therefore, the use of visible-light-driven photocatalysts will not only increase the outdoor photocatalytic activity but also enable the extension to indoor application where there is almost no UV irradiation.

There are two main strategies to develop visible-light-driven photocatalysts. The first one is the band-gap modification of TiO_2 to extend its absorption to visible range, through O-site doping, such as $TiO_{2-x}N_x$, $TiO_{2-x}C_x$ [3-5] and metal ions doping using V, Cr, Mn, Fe et al. [6-9]. However, the methods used for the dopant introduction are not easily controlled, and the low thermal stability of these compounds limits their applications. Moreover, these dopants may also work as recombination center between photogenerated electrons and holes and consequently decrease photocatalyst efficiency. The second strategy is to exploit other materials that absorb visible light directly. As highlighted by Kudo A. et al in 2008 [10], monoclinic scheelite structure $BiVO_4$ (*m*-

$BiVO_4$) with a narrow band gap of 2.4 eV has recently been considered as one of the most promising photocatalysts under visible light irradiation and has nowadays attracted much attention. $BiVO_4$ is stable and has neutral characteristic in water without changing the pH value, hence is suitable for environmental applications.

On the other hand, according to the photocatalytic kinetics [11-14], large specific surface area, well crystallization and less structural defects are usually required to achieve excellent photocatalytic performance. Meanwhile, it has been reported that the photocatalytic performance of $BiVO_4$ powders can be greatly influenced by the variation of electronic structure through the slight change of V−O band length, which is related to the crystal phase, crystallization and different morphologies [15]. Thus, synthesis optimization to control the phase, size and morphology of $BiVO_4$ crystals still remains a great challenge.

Besides the synthesis modification, construction of heterogeneous structure, such as p-n junction formation and noble metal surface loading, are considered to be effective strategy to separate electron-hole pairs, thus improve the photocatalytic property. Research work in this field is of great interest and is highly desired.

1.2 Objectives

The objective of this work is to improve the photocatalytic properties of *m*-$BiVO_4$-based nanoparticles under visible light irradiation, which is achieved by the control of synthesis mechanism, crystal size and morphology evolution, as well as surface modification by using hydrothermal-based wet chemical synthesis routes.

Systematic work is firstly conducted to study the pH effect on phase formation mechanism in a hydrothermal synthesis of $BiVO_4$, and the factors affecting their photocatalytic performance, both of which form the basis of further development.

Next, the hydrothermal synthesis process is modified in order to further control the morphology and the crystal size of the as-prepared *m*-$BiVO_4$ particles. The synthesis of well crystallized nanocrystals is explored for the enhancement of the photocatalytic performance.

Further, heterogeneous nanostructures are explored based on these as-prepared *m*-$BiVO_4$ nanocrystals in order to enhance the separation of photogenerated electron-hole pairs, and consequently improve the photocatalytic activity. This goal is achieved by two strategies: the p-n junction formation through the synthesis of Bi_2O_3 on *m*-$BiVO_4$, and the metal-*m*-$BiVO_4$ construction through the surface loading of Au or Pt nanoparticles. These heterogeneous nanostructures are carefully characterized and extensively studied.

Finally, the above two strategies are combined to achieve multi-composite nanostructure, which is promising to achieve further photocatalytic improvement. In addition, preliminary research works, such as scale-up synthesis and thin film deposition are also performed.

1.3 Major Contribution of the Thesis

This thesis has contributed to a better understandings on hydrothermal synthesis mechanism, developments in preparation methods, and improvement of photocatalytic activity of $BiVO_4$-based nanocrystals, which can be summarized as follows:

1. The first part of this work has provided clear understandings on the phase formation mechanisms in the hydrothermal synthesis of $BiVO_4$. It is found that, $pH \leq 9$ is necessary to obtain the monoclinic scheelite phase, *m*-$BiVO_4$. Based on the systematic study on pH effects, for the first time, it is concluded that the phase

formation and the crystal morphology of final $BiVO_4$ product are determined by the state and morphology of various Bi-precursors formed under different pH conditions.

2. Then, for the first time, it is proposed that the strong acid condition benefits good crystallization and size control in the hydrothermal synthesis of *m*-$BiVO_4$ crystals. Under this guidance, mono-dispersed *m*-$BiVO_4$ octahedral nanocrystals are firstly obtained with good crystallization and uniform size adjustable in a wide range. This work also provided detailed crystallography information of these single crystals based on extensive characterization efforts. Moreover, through the well synthesis control, these *m*-$BiVO_4$ octahedral nanocrystals have exhibited superior high photocatalytic performance whereby the degradation of RhB could be completed within 12 hours under visible light of normal indoor fluorescent irradiation.

3. Next, for the first time, a novel “etching” method has been developed to synthesize γ-Bi_2O_3 on the surface of *m*-$BiVO_4$ octahedral crystals, where the great challenge in chemical synthesis of γ-Bi_2O_3 phase was overcome. This method could achieve *m*-$BiVO_4$@γ-Bi_2O_3 core-shell p-n heterostructure with adjustable phase ratio of the two oxides. Based on the p-n junction formation and the combination of these two excellent visible-light photocatalytic materials (both phases are the best photocatalyst among their polymorphs, respectively), the visible-light photocatalytic performance in RhB degradation was greatly improved.

4. Meanwhile, it is the first time to systematically study, compare, and optimize the surface modification effects of Au and Pt nanoparticles on *m*-$BiVO_4$ nanocrystals. The Au/ and Pt/*m*-$BiVO_4$ heterogeneous nanoparticles exhibit much improved visible-light photocatalytic activity, whereby the RhB degradation could be finished within 7 hours under visible light of normal indoor fluorescent irradiation. In comparison, the

origin of such superior photocatalytic activity of Pt/*m*-$BiVO_4$ nanoparticles was found to be in the better dispersion of Pt nanoparticles than Au species.

5. Finally, for the first time, *m*-$BiVO_4$–based multi-composite nanocrystals are developed by combination of p-n junction formation with surface loading of noble nanoparticles. By using these *m*-$BiVO_4$/γ-Bi_2O_3/Pt nanoparticles, the RhB degradation could be finished within 4 hours under visible light of normal indoor fluorescent irradiation. The significance of this part of work is not only the further improvement in photocatalytic performance, but also the successful demonstration of a synergistic strategy, which can guide other materials development for photocatalysis and photoinduced energy conversion applications.

1.4 Organization of the thesis

The thesis contains 9 chapters, including the present introduction as Chapter 1.

Chapter 2 is composed of a literature review on the fundamental of photocatalytic reaction, some typical photocatalysts and their limitations. This chapter also reviews the various strategies to improve the photocatalytic efficiency under visible light irradiation.

Chapter 3 describes the preparation procedures of the $BiVO_4$ by hydrothermal method. Characterization methods of $BiVO_4$ on crystal structure and photocatalytic properties are also presented in details.

Chapter 4 investigates the pH effect and phase formation mechanism in the hydrothermal synthesis of monoclinic $BiVO_4$ particles. The morphology evolution is discussed based on the analysis on different reaction mechanisms and various states of Bi precursors. The factors affecting the photocatalytic performance, such as band gap energy, specific surface area as well as the local structure variation are also discussed.

Chapter 5 presents the size and morphology control of *m*-$BiVO_4$ octahedral nanocrystals through hydrothermal synthesis modification. Based on crystal characterization and property testing, the crystal growth mechanism and photocatalytic activities of as-prepared *m*-$BiVO_4$ nanocrystals are investigated.

Chapter 6 studies the *m*-$BiVO_4$/γ-Bi_2O_3 heterostructure with p-n junctions for photocatalytic performance improvement. The fabrication method through a simple etching process in alkaline solution is introduced. Also, the possible mechanisms in the enhancement of photocatalytic performance are discussed.

Chapter 7 explores the surface modification of *m*-$BiVO_4$ octahedral nanocrystals by loading Au or Pt nanoparticles. The mechanism behind the photocatalytic enhancement is illustrated. In addition, influences of Au- and Pt-loading are compared, and the resulting different photocatalytic performances are explained as well. Moreover, this chapter also illustrates the further improvement of photocatalytic activity by the combination of p-n junction formation with Pt surface loading.

Chapter 8 presents the conclusions as well as the recommended future works.

Chapter 2. Literature Review

2.1 Photocatalytic Reaction

Photocatalytic reactions are induced by photons (light) in the presence of a photocatalyst [16-21]. Photocatalysis on semiconductor particles involves three main steps: (i) absorption of photons with higher energies than the semiconductor band gap, leading to the generation of electron (e^-)–hole (h^+) pairs in the semiconductor particles; (ii) charge separation followed by migration of these photogenerated carriers in the semiconductor particles; and (iii) surface chemical reactions between these carriers with various compounds (e.g., H_2O); electrons and holes may also recombine with each other without participating in any chemical reactions.

Figure 2.1 summarizes the generation of the electron-hole pair, its recombination and the redox reaction [22].

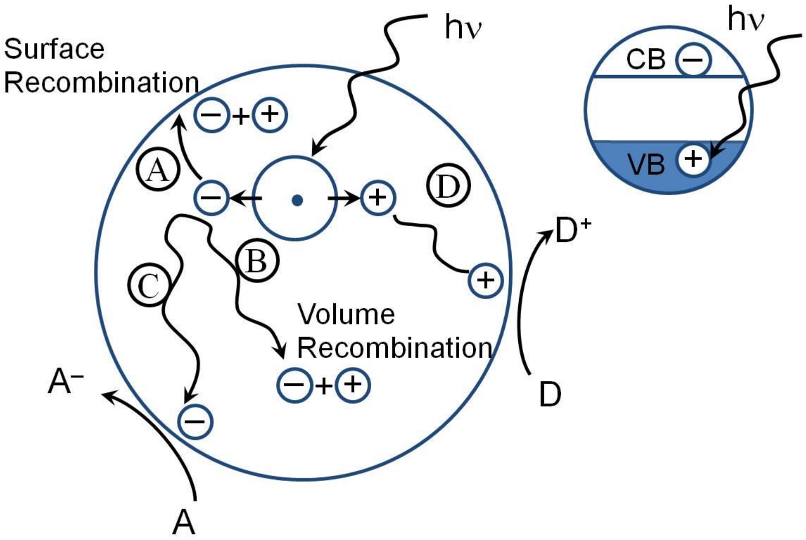

Figure 2.1 photocatalytic reaction; generation and recombination of electron-hole pair and redox reactions [22].

The photocatalytic reaction can be summarized as followed [23]. For the redox reaction, the photogenerated electrons diffuse to the surface and reduce electron acceptor; while the holes oxidize electron donor. The electron donors include absorbed substrate (RX), water or OH ions. As there is a higher concentration of OH from water dissociation, it is more likely to oxidize OH ions:

$$H_2O + h^+ \longrightarrow \bullet OH + H^+ \qquad (2\text{-}1)$$

$$OH^- + h^+ \longrightarrow \bullet OH \qquad (2\text{-}2)$$

$$h^+ + RX \longrightarrow RX^+ \qquad (2\text{-}3)$$

For electron acceptor, oxygen molecules act as the scavenger to absorb electrons and form super-oxide anions, $\bullet O_2^-$:

$$O_2 + e^- \longrightarrow \bullet O_2^- \qquad (2\text{-}4)$$

This super-oxide anions undergo further reactions to form •OH and •OOH radicals and hydrogen peroxide:

$$H_2O + \bullet O_2^- \longrightarrow \bullet OOH + OH^- \qquad (2\text{-}5)$$

$$2\ \bullet OOH \longrightarrow O_2 + H_2O_2 \qquad (2\text{-}6)$$

$$\bullet OOH + H_2O + e^- \longrightarrow H_2O_2 + OH^- \qquad (2\text{-}7)$$

$$H_2O_2 + e^- \longrightarrow \bullet OH + OH^- \qquad (2\text{-}8)$$

The radicals, (•OH, •OOH, H_2O_2) formed from the redox reaction, are able to oxidize organic pollutants to form carbon dioxide and water. The overall reaction is shown in equation (2-9) [16]. The organic pollutant can be volatile organic compound (VOC) [24-27], or bacteria [28-30] and this has created interest as it has potential applications in water splitting, air quality control, water treatment, antibacterial and self-cleaning surfaces.

$$\text{Organic pollutant} + O_2 \longrightarrow CO_2 + H_2O + \text{mineral acids} \qquad (2\text{-}9)$$

2.2 Photocatalytic Materials

2.2.1 Historical overview

In 1921, Renz reported that titania can be partially reduced with sunlight in the presence of an organic compound glycerol, the color of this oxide turning from white to dark; and he also found similar phenomena with CeO_2, Nb_2O_5 and Ta_2O_5. The reaction for TiO_2 was proposed to generate Ti_2O_3 or TiO [31]. In 1924, Baur and Perret first reported the photocatalytic deposition of a silver salt on ZnO to produce metallic silver [32]. At this early date, the authors suspected that both oxidation and reduction happened simultaneously and it is proposed as:

$$\mathrm{ZnO} + h\nu \longrightarrow \mathrm{h}^{+} + \mathrm{e}^{-} \qquad (2.10)$$

$$\mathrm{OH} + h^{+} \longrightarrow 1/4\mathrm{O_2} + 1/2\mathrm{H_2O} \qquad (2.11)$$

$$\mathrm{e}^{-} + Ag^{+} \longrightarrow \mathrm{Ag} \qquad (2.12)$$

After three years of study, they proposed simultaneous oxidation and reduction to explain the production of hydrogen peroxide on ZnO [33]:

$$\mathrm{CH_2O} + 2h^{+} + 2\mathrm{OH}^{-} \longrightarrow \mathrm{CO} + 2\mathrm{H_2O} \qquad (2.13)$$

$$2\mathrm{e}^{-} + \mathrm{O_2} + \mathrm{H}^{+} \longrightarrow \mathrm{H_2O_2} \qquad (2.14)$$

It was not until 8 years later that the proposal was confirmed. In 1932, Renz reported the photocatalytic reduction of silver nitrate to metallic silver and gold chloride to metallic gold with a number of illuminated oxides, including TiO_2 and Nb_2O_5 [34], and subsequently discussed the results according to the Baur redox mechanism. It has been recognized for quite a long time that titania-based exterior paints tend to have “chalking” effect under strong light. This effect was considered resulting from the actual removal of part of the organic component of the paint, leaving the titania itself exposed. In 1938, Goodeve and Kitchener made a study on the photocatalytic decomposition of a dye with titania powder in air [35]. They proposed that titania acts as a catalyst to accelerate the photo chemical oxidation and also studied a number of other oxides.

During the 1950s, ZnO got much more attention for the development of photocatalysis. In these studies, the overall reactions and mechanisms were completely clarified, and it became clear that organic compound was oxidized while oxygen was reduced. Markham with her co-worker constructed and studied a number of different types of photo-assisted fuel cells, using illuminated ZnO as the photo-anode and alcohols as the organic substrates [36-38]. But the inevitable problem of ZnO photo-corrosion prevented this system from reaching practical application. In 1958, Kennedy et al. studied the photo-absorption of O_2 on TiO_2 in order to fully understand the photocatalytic process [39]. They concluded that electrons were transferred to O_2 because of photo excitation, and led to reduced form of O_2 adsorbed on the TiO_2 surface. The authors found a relationship between the ability of the TiO_2 to photocatalytically decompose chlorazol sky blue and the ability of photo-adsorb O_2. This phenomenon is very important for understanding photocatalysis. 1964 in Japan, Kato and Mashio found that different types of titania powders had different photocatalytic activities. With the Fujishima report of the ability to simultaneously generate hydrogen gas in 1972 [1], the photocatalysis field started to receive much more attention, because of its implications for solar energy conversion.

2.2.2 Titanium Dioxide, TiO_2

TiO_2 has always been of great interest. This is mainly because of its unique properties such as being inert, physically and chemically stable, non-toxic, inexpensive, and sensitive to UV light. Under visible light, TiO_2 displays almost no absorption, and hence, it is white. TiO_2 exists in the forms of anatase, rutile and brookite. Table 2.1

summarizes the bulk properties of the three phases [40]. The two crystal phases of titanium dioxide that are commonly used in photocatalytic applications are rutile and anatase.

Table 2.1 Properties of bulk TiO_2 and its different phases [40].

<table>
<tr><th colspan="7">Bulk TiO_2</th></tr>
<tr><td><i>Atomic Radius (nm)</i></td><td colspan="2">O = 0.066 (Covalent)</td><td colspan="4">Ti = 0.146 (Metallic)</td></tr>
<tr><td><i>Ionic Radius (nm)</i></td><td colspan="2">O (-2) = 0.14</td><td colspan="4">Ti (+4) = 0.064</td></tr>
<tr><th colspan="7">Individual Phases</th></tr>
<tr><td rowspan="2"><i>Crystal Structure</i></td><td rowspan="2"><i>System</i></td><td rowspan="2"><i>Density (kg/m^3)</i></td><td colspan="4"><i>Lattice Constants (nm)</i></td></tr>
<tr><td><i>a</i></td><td><i>b</i></td><td><i>c</i></td><td><i>c/a</i></td></tr>
<tr><td>Rutile</td><td>Tetragonal</td><td>4240</td><td>0.4584</td><td>-</td><td>0.2953</td><td>0.644</td></tr>
<tr><td>Anatase</td><td>Tetragonal</td><td>3830</td><td>0.3733</td><td>-</td><td>0.937</td><td>2.51</td></tr>
<tr><td>Brookite</td><td>Rhombohedral</td><td>4170</td><td>0.5436</td><td>0.9166</td><td>0.5135</td><td>0.944</td></tr>
</table>

Of the two phases, anatase shows relatively greater photocatalytic activity and is used more frequently for photocatalytic oxidation reactions, while rutile is primarily used as pigments due to its light scattering properties. The amorphous-anatase-rutile phase transformation temperatures depend on several variables such as: initial particle size [41], doping concentration [42], original phase [43], and reaction atmosphere [44]. At room temperature bulk TiO_2 rutile is the stable phase; however, the phase stability of nanoparticles depends on the particle size. Zhang and Banfield [41] have shown that when particle size becomes less than 14 nm, anatase becomes more stable than rutile.

Among the three phases, rutile has the smallest band gap (3.0 eV), but its photocatalytic reactivity is much lower than anatase, that is mainly because of the higher recombination rate for electron-hole pair in rutile phase than anatase [45]. While, anatase, with a band gap of 3.2 eV, has the highest photocatalytic property, which can be further improved by mixing with rutile. The differences in the band edge position can help holes move to anatase phase while electrons migrate into rutile phase, and hence reduce recombination [46]. This mixed phase TiO_2 makes Degussa P25 as the benchmark for photocatalyst. P25 has a ratio of 8:2 for anatase to rutile with BET measurement at around 50 m^2/g and several hundred nanometers in particle size [47].

2.2.3 Zinc Oxide, ZnO

ZnO is the next best alternative to TiO_2. Similar to TiO_2, it has a band gap of 3.2 eV at the same band edge position. Moreover, it has a direct band gap, that gives rise to a higher efficiency in electron-hole pair generation [48]. In some instances, it has shown better photocatalytic performance than TiO_2. However, ZnO suffers from photocorrosion, where it is oxidized by photogenerated holes to form Zn^{2+}. This leads to the loss of photocatalytic property.

Photocorrosion can be inhibited by removing the photogenerated holes from ZnO. Zhang et al. showed similar degradation rate of methylene blue for 3 cycles with polyaniline-ZnO [49]. They proposed that the hybrid structure enhance electron-hole separation with holes migrating to polyaniline, which prevents the holes from oxidizing ZnO.

2.2.4 Cadmium sulfide, CdS, and Cadmium Selenide, CdSe

CdS and CdSe are studied for its narrow band gap [50]. A narrow band gap is favorable for photocatalytic reaction as it could absorb visible light. However, the major problem with these kinds of materials is the photocorrosion as well. In addition, Cd^{2+} ions can be released which is toxic to our environment, so it would not be feasible for consumer applications.

2.2.5 Strontium Titanate, $SrTiO_3$

The perovskite-type oxides are very famous among the metal oxide photocatalyst because they have wide diversity of properties. Figure 2.2 shows an ideal perovskite-type cubic structure of ABO_3 with the space group Pm3m, the coordination number of cation A is 12-fold and B cation is 6-fold coordinated with the oxygen anions. The corner-sharing BO_6 octahedral forms the skeleton of the cubic structure, in which the center position is occupied by the A cation. A wide range of cations and valences can be accommodated in this simple crystal structure. Due to the susceptibility of partial substitution at both A and B sites, it renders perovskite with diverse and flexible chemical tailoring [51]. As a typical $A^{2+}B^{4+}O^{3-}$ type perovskite, $SrTiO_3$ has been known as a photocatalyst capable of decomposing H_2O into H_2 and O_2 without applying an external bias potential [52]. $SrTiO_3$ has a large band gap (3.2 eV), which can only absorb UV light, many researches focus on the doping of foreign elements, mostly transition metals, into $SrTiO_3$ to improve its absorption to visible light. For example, chromium has been paid much attention because the occupied Cr^{3+} level is usually about 2.2 eV lower than the conduction band bottom formed by Ti 3d or 1.0 eV higher than the valence band top formed by O_{2p} [53].

ABO_3 perovskites have a very important characteristic which is their ability of partial substitution of cations at both A and B sites and the stability of mixed oxidation states or unusual oxidation states in the crystal structure. For example, if the Cr cations are alternatively doped at the Sr^{2+} site rather than the Ti^{4+} site, different photophysical and photocatalytic properties might be obtained.

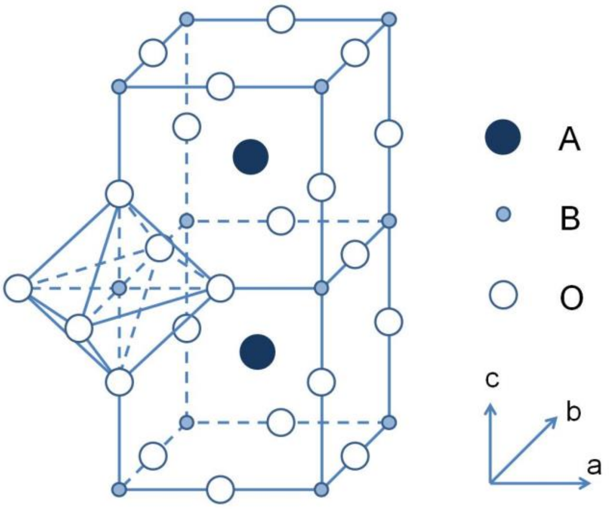

Figure 2.2 Ideal ABO_3 perovskite structure. The BO_6 octahedron links through corners to form a three-dimensional cubic lattice, and the A cation is in the center of the cube [51].

2.3 $BiVO_4$ for Visible light Photocatalysis

2.3.1 Visible light induced photocatalysis

Due to the large band gap, the anatase and rutile TiO_2 photocatalysts mainly absorb UV light. However, the solar spectrum only comprises a small amount of ultraviolet photons (about 4%), and room light lamps emit mainly visible photons. Therefore, many efforts have been devoted to extending the spectral response of pure TiO_2 material to visible light. This includes doping TiO_2 with metal impurities [54], non-metal atoms [55], coupling TiO_2 with narrow band-gap semiconductors [56] and oxygen-deficient TiO_2 [57].

Asahi et al. first reported visible light photocatalysis with N-doped TiO_2 [3]. They prepared the photocatalyst by two methods: one was by sputtering a TiO_2 target in an N_2/Ar mixture gas; the other was by calcinating TiO_2 powder in an NH_3/Ar atmosphere. Both methods produced yellow TiO_2 photocatalyst that absorbed light at less than 500 nm and showed activity under visible light for the decomposition of methylene blue solution (Figure 2.3). As the direct evidence of N doping, XPS studies on N-doped TiO_2 materials often gave two kinds of N1s peaks, one at about 396 eV, and the other one at 400 eV [58]. It was thus believed that at least two kinds of nitrogen doping were responsible for the visible light photo activity. The 396 eV peak is generally assigned to substitution nitrogen doping; while the 400 eV peak is believed to relate to interstitial nitrogen doping.

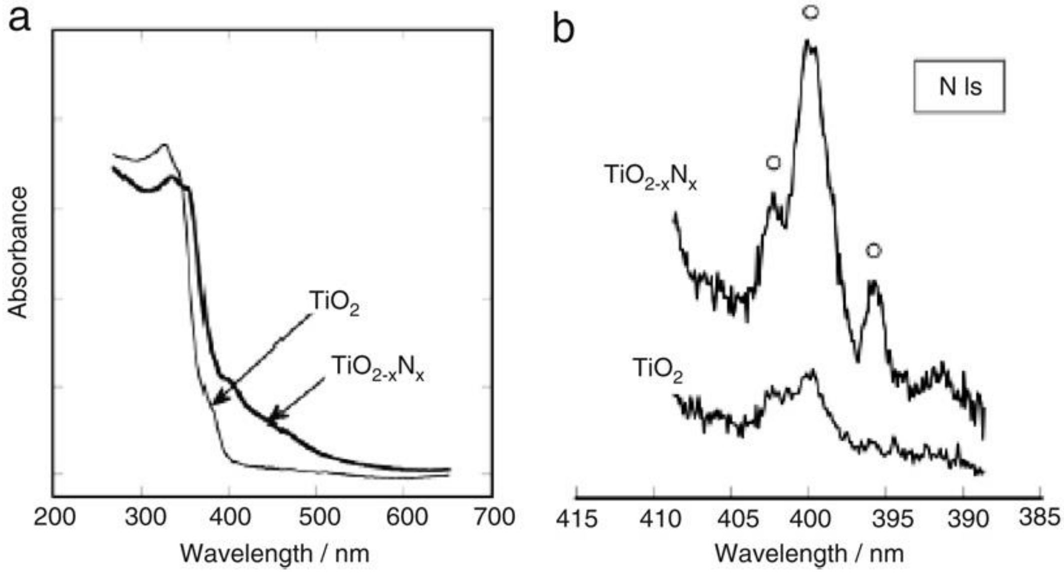

Figure 2.3 (a) optical absorption spectra of $TiO_{2-x}N_x$ and TiO_2 films and (b) N1s XPS spectra of TiO_2 and $TiO_{2-x}N_x$ films [3].

As commented by Serpone, it is impossible that a low level of doping (<2 atomic %) can rigidly shift up the valence band [59]. Irie et al. reported that the quantum yields of gaseous 2-propanol decomposition on N-doped TiO_2 powders under visible light were several times lower than those under UV source [60]. This observation could not be explained by the band gap narrowing model. Instead, it suggested that nitrogen doping led to the formation of localized mid-gap states above the valence band edge as shown in Figure 2.4.

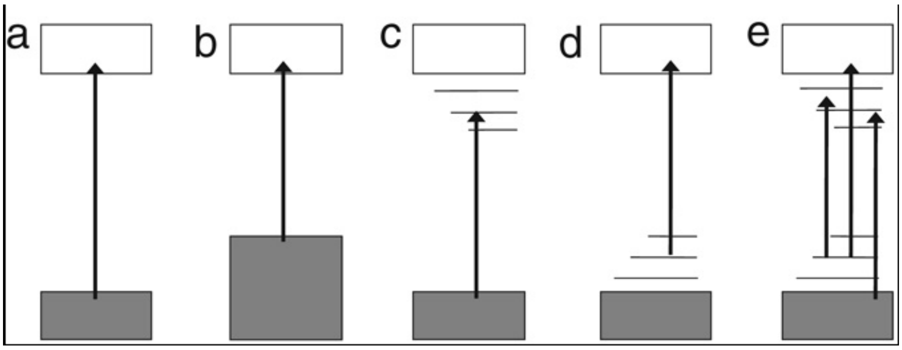

Figure 2.4 Various schemes illustrating the possible band-gap electronic structure and excitation processes of visible light responsive TiO_2 materials: (a) pure TiO_2; (b) band-gap narrowing model for non-metal-doped TiO_2; (c) oxygen-deficient TiO_2; (d) localized mid-gap level model for non-metal-doped TiO_2; (e) oxygen vacancy levels and non-metal-doped mid-gap levels are considered together [59].

Irie et al. also reported the preparation of C-doped TiO_2 by oxidative heating of TiC powders [61]. Either anatase or rutile type C-doped TiO_2 was prepared by controlling of the heating temperature. The prepared materials were yellow with observable shifts to visible light, and the carbon dopant showed a peak at 281.8 eV in the C1s XPS spectra. But the photocatalytic activity of C doped TiO_2 under visible light was quite weak, as evaluated by the decomposition of gaseous 2-propanol.

2.3.2 Bismuth vanadate ($BiVO_4$)

During past decades, the non-titania-based visible-light-driven semiconductor photocatalysts such as $InTaO_4$, $BiVO_4$, $BaCr_2O_4$ and Ta_3N_5, as a rapid growing material family, have been employed for the degradation of organic contaminants and water splitting to generate oxygen and hydrogen [62-66]. As highlighted by Kudo A. et al in 2008 [10], $BiVO_4$ with a low band gap of 2.4 eV has recently been considered as one of the promising photocatalysts under visible light irradiation and has nowadays attracted much attention owing to its stable and neutral characters in water without changing the pH value, which is suitable for environmental applications.

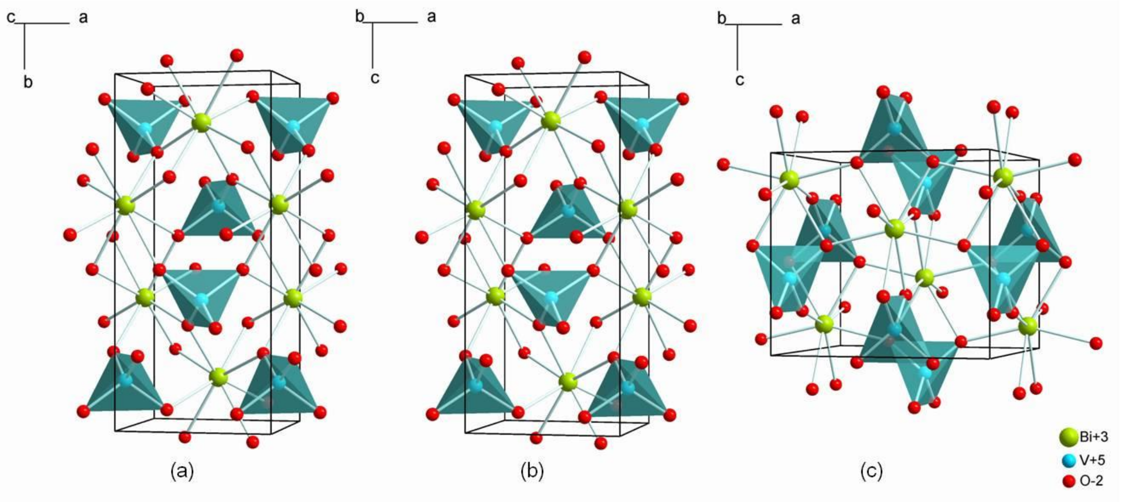

Figure 2.5 Schematic representation of (a) monoclinic scheelite structure, (b) tetragonal scheelite structure and (c) tetragonal zircon structure.

$BiVO_4$ presents in three crystalline phases, monoclinic scheelite structure (s-m), tetragonal scheelite structure (s-t) and tetragonal zircon structure (z-t) [67-69], as shown in Figure 2.5. Among them, $BiVO_4$ with monoclinic scheelite structure (*m*-$BiVO_4$) is found to exhibit the best photocatalytic performance under visible light illumination [70]. The reason lies in its distinct electronic structure due to the asymmetric crystal structure.

Actually, the crystal structure of *m*-$BiVO_4$ is very close to that of the tetragonal scheelite phase (*st*-$BiVO_4$), as shown in Figure 2.5 and compared as follows:

m-$BiVO_4$: a = 5.1966 Å, b = 11.7044 Å, c = 5.0935 Å, and β = 90.383°;

st-$BiVO_4$: a = c = 5.1509 Å, b = 11.730 Å, and β = 90° [71]

Due to the high symmetry of *st*-$BiVO_4$, only one type of V–O bond (V–O = 1.72 Å) exists in the VO_4^{3-} tetrahedron. Then the bismuth cation is coordinated by eight identical VO_4^{3-} tetrahedrons. Therefore, there is no lone-pair distortion around Bi^{3+} due to the balanced symmetry constraints [71]. In contrast, the low symmetry in *m*-$BiVO_4$ results in a distorted VO_4^{3-} tetrahedron, and there are two distinct bond lengths ($V–O^{I}$ = 1.69 Å and $V–O^{II}$ = 1.77 Å). In this condition, the Bi–O bond lengths around the bismuth cation are different and a typical lone-pair distortion can be observed. Such asymmetry of crystal structure provides a distinct electronic structure. The valence band of *m*-$BiVO_4$ is formed by a hybrid of the Bi 6s and O 2p orbitals, while the conduction band is composed of V 3d orbitals [66]. It has been reported that the distortion of the VO_4^{3-} tetrahedron, corresponding to the lone-pair electron of Bi^{3+} in the local structure of $BiVO_4$, can result in the overlap between the Bi 6s and O 2p orbitals, which can greatly benefit the migration of photogenerated holes, thus, its higher photocatalytic performance [15].

Generally, photocatalyst require large surface area to ensure high photocatalytic efficiency, although *m*-$BiVO_4$ has been fabricated for yellow pigment long ago, the ultra fine powder synthesis for photocatalysis has not been studied until early this century. So far, it has been reported that *m*-$BiVO_4$ micro-/nano-particles or thin films can be generated by means of various methods, such as solid-state reaction [72], aqueous approach [66,68], hydrothermal treatment [15,73-75], chemical bath deposition [76] and sonochemical route [77]. Among these strategies, the “bottom up” hydrothermal method has attracted much attention due to its simplicity and effectiveness in producing *m*-$BiVO_4$ with perfect crystalline structures and regular morphologies in an environmentally mild way [74,75]. In order to increase the specific surface area of the material, up to now, there have been a lot of morphologies of $BiVO_4$ powders achieved under different reaction conditions, such as polyhedral and rod-like morphologies by a hydrothermal process with ammonia as pH adjusting agent [15], micro-tubes single crystal structure by a simple reflux method [78], and flower-like $BiVO_4$ mesocrystals by a facile additive-free aqueous strategy [79]. However, the discussion on the reaction mechanism has seldom been reported [78,80], and the control of crystal size and morphology needs further improvement.

2.3.3 Approaches to enhance the photocatalytic performance

Apart from the synthesis process control of a photocatalytic semiconductor itself, the strategies to enhance its photocatalytic property can generally be classified into two categories [81]: doping with metal/ nonmetal species, and constructing heterostructure.

Through modifying the electronic structure and tailoring the surface structure of photocatalyst, doping is a powerful strategy. By properly designing the configuration and distribution of dopants in semiconductor photocatalysts, the modification of electronic structures can realize visible-light activity of wide band gap materials, while the formation of surface heterogeneous structures allow high-efficiency photocatalysis [81]. Since Asahi group first reported N-doped TiO_2 in 2001 [3], almost all metals and non-metals have been explored as dopants to modify the electronic structure of TiO_2 to improve its photocatalytic performance; while the process on other photocatalyst is undergoing. Nonetheless, there are still some great challenges in the development through doping: (1) to exactly control the spectral distribution of dopant-induced electronic states; (2) to control the surface heterogeneous structure, thereby to ensure the sufficient energy of the photogenerated electron-hole pairs in order to migrate to surface for photoreaction, (3) to make sure that the dopant does not act as a defect center; and (4) to realize homogeneous distributions of dopants throughout photocatalyst crystals.

Then, for constructing heterostructure, the objective is to enhance the separation of photogenerated electron-hole pairs through various carrier-transfer pathways, and to extend the light-response range by coupling suitable electronic structures. According to the charge carrier-transfer mechanisms, six heterostructure modes can generally be classified [81], as shown in Figure 2.6. Among them, traditional charge-carrier transfer, sensitization and co-catalyst coupling have been the most widely investigated in recent years.

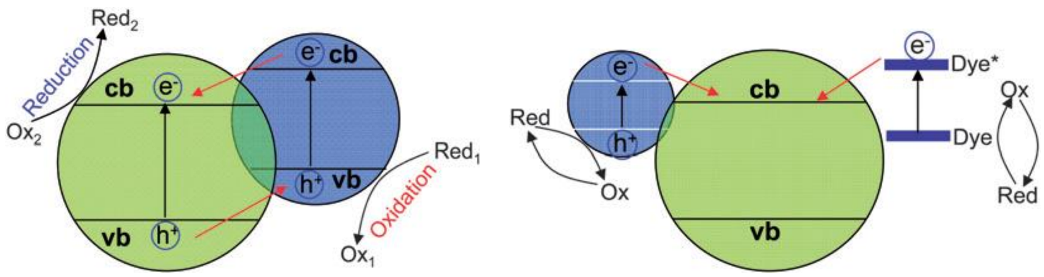

(a) Traditional charge-carrier transfer; (b) Sensitization

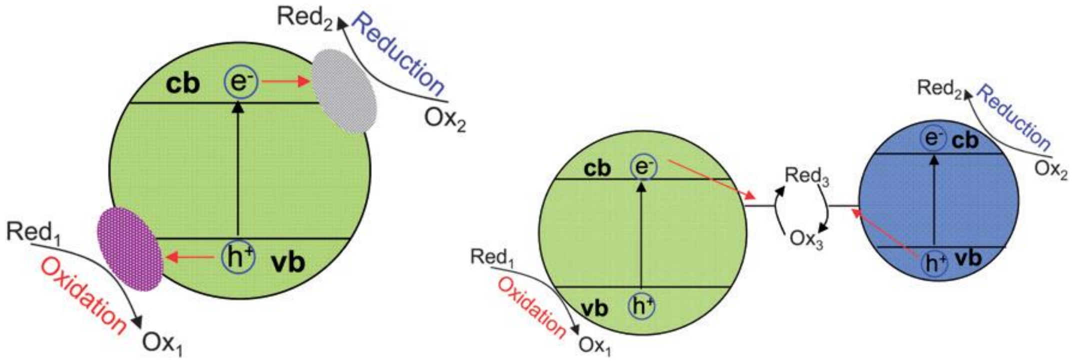

(c) Co-catalyst coupling (d) Indirect Z-Scheme

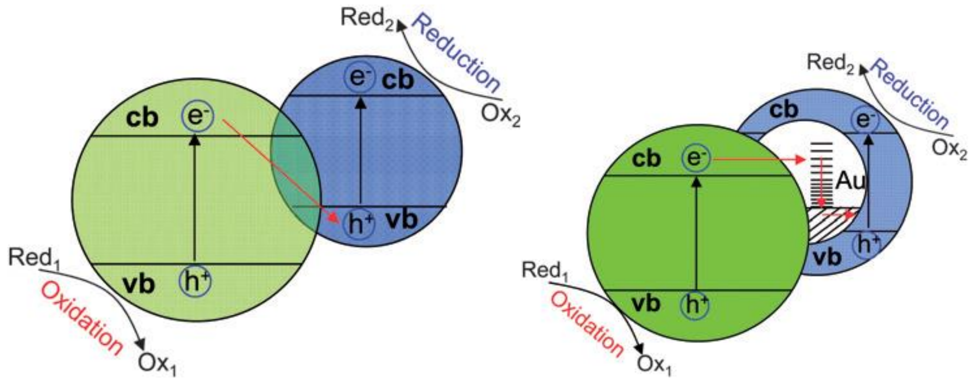

(e) Direct Z-Scheme (f) Vectorial electron transfer

Figure 2.6 Mechanisms in heterostructured photocatalytic materials [81].

The traditional charge-carrier transfer can be involved through the formation of heterojunction between two different semiconductors. In general, electrons can be smoothly transferred from one semiconductor with a higher conduction band (CB) minimum to another with a lower one, while the holes on valance band migrate reversely, which can effectively reduce the recombination of electron-hole pairs by keeping the reduction and oxidation reaction on different materials.

Sensitization process is similar to the traditional one in semiconductor junctions. The difference is that electrons are injected from excited dye to semiconductor rather than from one semiconductor to another. After the absorption of photon energy, the excited states are formed in an organic dye, and the light induced electrons are soon transferred onto the photocatalyst. Efficient dye-sensitizers are helpful in broadening the light response range of wide band gap semiconductors, thus in the improvement of solar energy absorption. This research field has attracted great attention and been widely used in solar cell and photocatalytic applications [82].

Co-catalyst coupling is very useful to improve the eventual efficiency of the actual redox reactions. Noble metals, such as Au, Ru, Ag and Pt, are widely used as reduction catalyst that can improve the utilization of photogenerated electrons in reducing reaction, especially the hydrogen generation in water splitting. The oxygen evolution catalysts are usually transition metal oxides, such as NiO and RuO_2 [83].

2.3.4 Strategies to enhance the charge separation in $BiVO_4$

Although *m*-$BiVO_4$ with band gap around 2.4 eV can utilize a greater portion of the solar light than TiO_2 does, the photocatalytic activity of the pure $BiVO_4$ is comparatively lower, which is mostly due to the rapid recombination of photogenerated electron–hole pairs [84-89]. Thus towards practical applications, the photocatalytic activity of $BiVO_4$ needs to be further improved through the promotion of charge carrier separation. Recent progress has been achieved through the successful preparation of $BiVO_4$ composite materials in combination with metals or metal oxides [90-92]. Especially, the construction of p-n junction by both p- and n-type materials is considered as the most efficient way to enhance the charge carrier transfer. As a matter of fact, the explanations about the migration of photogenerated electron-hole pairs on semiconductor photocatalysis are still under debate. Some viewpoints are summarized as follows:

(1) The migration is totally driven by inner electric field. At the thermodynamic equilibrium of a p-n heterojunction semiconductor, an inner electric field can be established with a direction from n-type material to p-type one. So the electron will move to n-type semiconductor while simultaneously holes can be transferred in the opposite direction. This explanation is accepted and cited by many researchers [93-96].

(2) The migration is determined by the band edge position between two p-n heterojunction interfaces. After combination, the excited electron is easy to transfer to even lower conduction band, and the excited hole will transfer to the material with higher valence band, finally the recombination of charge carries is inhibited [97,98].

(3) Recently, Long’s group indicated that both the inner electric field and band edge position have effect on the migration of electron and hole pairs [99], as illustrated in Figure 2.7. Among three different types of configurations, type (a) is the most efficient one for photocatalytic enhancement, where both the band edge position and inner electric field direction are preferable for the charge carrier. Type (b) is still helpful based on the feasible migration of holes. However, in type (c), both the migration of electrons and holes towards favorable bands are prohibited by the inner electric field.

Despite the debate in the charge transfer mechanism, several statements are widely recognized, and have been followed to guide the design and preparation of the semiconductor composites. In order to improve the photocatalytic performance under visible light irradiation, successful coupling of the two semiconductors should be achieved with the following conditions: (i) semiconductors should be photocorrosion free, (ii) the semiconductor should possess appropriate band gap values for visible light excitation, (iii) the band gap structures of the two semiconductor should be suitable for coupling, and (iv) electron injection should be fast as well as efficient.

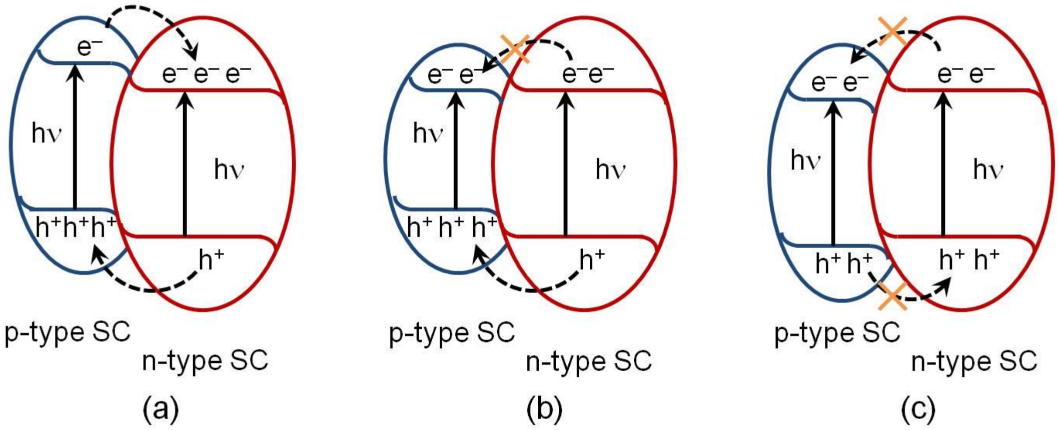

Figure 2.7 Charge transfer mechanisms in composite photocatalytic materials with p-n junction formation [99].

Apart from semiconductor-semiconductor junctions, metal-semiconductor contact, forming Schottky junction, can also be explored to facilitate the charge carrier separation. This can be achieved by loading metal nanoparticles onto the surface of photocatalytic semiconductors. Similar to the semiconductor p-n junctions, the space charge region and a built-in potential in a Schottky junction are able to promote the migration of photogenerated electron-hole pairs. However, the impact of metal-loading can be more complicated due to other possible contributions of metal nanoparticles such as the co-catalyst effect and the surface plasmon resonance (SPR) [100]. For example, in some reported work, it was claimed that the SPR of the loaded metal nanoparticles can provide additional visible light absorption, which can also contribute to the overall photocatalytic activities [101].

So far, varieties of semiconductors and metals were tried to composite with $BiVO_4$, including $Co_3O_4/BiVO_4$ [99], Ag-AgCl/$BiVO_4$ [102], $CeO_2/BiVO_4$ [87],

$CuO/BiVO_4$ [90], $Pt\text{-}RuO_2/BiVO_4$ [103], $WO_3/BiVO_4$ [104], $V_2O_5/BiVO_4$ [105], $Bi_2O_3/BiVO_4$ [106], $Cu/BiVO_4$ [107], $Pd/BiVO_4$ [108,109], $Ag/BiVO_4$ [110-112], $Au/BiVO_4$ [113,114], etc. These results and progresses are exciting and stimulating further investigations on this material.

2.4 Summary

Recently, photocatalytic semiconductor materials have attracted considerable attention due to their potential in organic contaminants degradation and water splitting by utilizing abundant solar light. Since Fujishima and Honda used a TiO_2 photoanode in 1972 to split water, researchers have been attempting to modify or exploit materials that can efficiently use visible light. $BiVO_4$ with a narrow band gap of 2.4 eV has nowadays attracted much attention for its visible light application. Many morphologies have been achieved, but the formation mechanism is not well discussed. In addition, due to the severe recombination of the photogenerated electron-hole pairs, the photocatalytic activity of $BiVO_4$ needs to be improved by constructing composite materials with metal and p-type oxides. Therefore, based on the fundamental understandings of photocatalysis and preliminary developments on this material, synthesis improvement is essential for better size/morphology control, while the preparation and investigation on heterogeneous structured composite are of huge interest for further photocatalytic enhancement.

Chapter 3. Experimental Methods

3.1 Sample Fabrication

Chemicals: $Bi(NO_3)_3 \cdot 5H_2O$ (99.9%), NH_4VO_3 (99.9%), $HAuCl_4 \cdot 3H_2O$ (99.9%), $H_2PtCl_6 \cdot 6H_2O$ (>37.5% Pt basis) and Sodium Dodecyl benzene sulfonate (SDBS, >98%) were purchased from Sigma Aldrich. NaOH (99.9%), nitric acid solution (99.9%), were derived from Fluka. Fluorine-doped tin oxide (FTO) (obtained from USA, sheet resistivity: ~10 Ω/sq) was cut into pieces with a size about 3×7 cm^2 and used as substrate for thin film deposition. De-ionized (DI) Milli-Q water (> 18.2 MW) with total organic carbon (TOC) ~57 ppb, was used as aqueous solvent in the synthesis. Ethanol (>99.9%, from Merck) was used as solvent in the photochemical synthesis of Au or Pt nanoparticles. All chemical reagents were used without further purification.

The syntheses of $BiVO_4$ nano- to micron sized particles, as well as the control of different morphologies were conducted by a simple hydrothermal method, as shown in Figure 3.1. In a typical synthesis, 1 mmol $Bi(NO_3)_3 \cdot 5H_2O$ and 1 mmol NH_4VO_3 were separately dissolved in 2 M nitric acid solution. These solutions were then mixed together, followed by vigorous stirring to obtain an orange solution. Appropriate amount of DI water was also added into the prepared solution to dilute the solution to a total volume of 35 ml. The final solution was transferred into a 50 ml Teflon-lined autoclave and maintained at 150 °C for 20 h, followed by naturally cooling to room temperature. The yellow product was collected and washed with DI water and ethanol for several times to remove ions and possible remnants, and finally dried in oven at 70 °C.

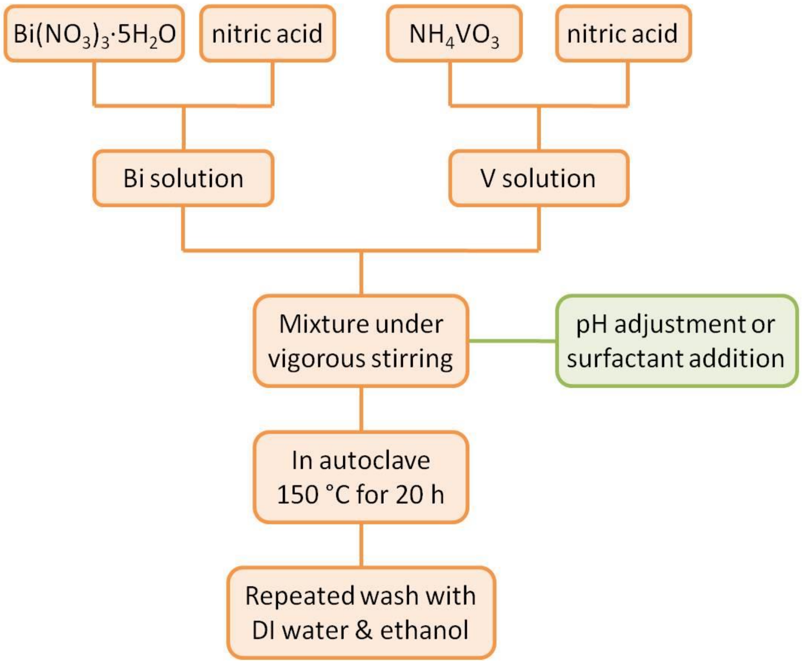

Figure 3.1 Synthesis procedure of BVO_4 crystals by hydrothermal method.

Based on the synthesis of *m*-$BiVO_4$ crystals, further composite processing or modification were also applied in terms of the p-type Bi_2O_3 phase generation, Au/Pt nanoparticles synthesis and thin film deposition. The method and procedure are detailed in the corresponding chapters.

3.2 Characterization

The powder and thin film X-ray diffraction (XRD) patterns were collected by using Shimadzu 6000 X-ray diffractometer with Cu *Ka* radiation ($\lambda = 1.5406$ Å) over the 2θ range of 5º~75º. The crystal structure study and quantitative analysis by Rietveld simulation were conducted by using the software Topas (Version 3, from Bruker).

The morphology, microstructure and chemical composition of the as-prepared samples were analyzed by scanning electron microscopy (SEM) (Model 5410, JEOL) equipped with energy dispersive spectroscopy (EDS) detector (Oxford), as well as a field emission SEM (FESEM) (Model 6340F, JEOL).

Transmission electron microscopy (TEM) was used to further study the microstructure, crystal phase and elemental composition of the powder samples. For lattice imaging and phase identification, high-resolution transmission electron microscopy (HR-TEM) images and selected-area election diffraction (SAED) patterns were taken using a JEM-2100F (JEOL) with point resolution of 1.9 Å and working at 200 kV. The JEOL 2100F was also equipped with EDX systems, which was used for composition analysis under scanning transmission electron microscopy (STEM) mode. The electron probe size for EDX was about 1~1.3 nm.

Optical properties of the samples were analyzed by an UV-Vis diffused reflectance spectrophotometer (UV-2450, Shimadzu), while the photoluminescence (PL) spectra were recorded on a spectrofuorophotometer (RF 5301, Shimadzu).

Raman spectra of $BiVO_4$ powders were recorded using a confocal Raman microscopy system with an excitation line of 488 nm and an air cooling charge coupled device (CCD) as the detector (CRM200, WITec).

The specific surface area values of the samples were analyzed by an adsorption analyzer (ASAP 2020, Micromeritics) using BET method. For all powder samples, the degas was conducted for 12 hours with heating at 180 °C.

The flat band potential of an *m*-$BiVO_4$ thin film was evaluated by the Mott-Schottky plots, which were derived from electrochemical impedance spectroscopy (EIS) measurements. The EIS measurements were conducted in dark condition by using a potentiostat from Solartron Instruments, model SI 1287 Electrochemical Interface, combined with an SI 1255 HF Frequency Response Analyzer. The *m*-$BiVO_4$ thin film was used as a photo working electrode with 4.9 cm^2 geometric area exposure to the electrolyte solution. And the three-electrode configuration was completed by using a Pt-wafer counter electrode and an Ag/AgCl reference electrode (in 3 M KCl solution, 0.21 V vs. NHE). The experiment was carried out in 0.1 M Na_2SO_4 solution with AC amplitude 50 mV at each applied potential, and measurements were conducted at four different frequencies: 200, 300, 500 and 1000 Hz.

Surface photovoltage spectroscopy (SPS) technique is a non-destructive method to study the separation and transfer behavior of photo-induced charge carriers at semiconductor solid surface [115]. Here it was used to demonstrate the photo-induced charge transfer in the synthesized $BiVO_4$ composite powders for photocatalytic applications. This value was characterized by measuring the change of contact potential difference (ΔCPD) in dark and under illumination using a commercial UHV Kelvin probe unit (from KP Technology Ltd) incorporated with an optical monochromatic illumination system through a quartz window, as illustrated in Figure 3.2.

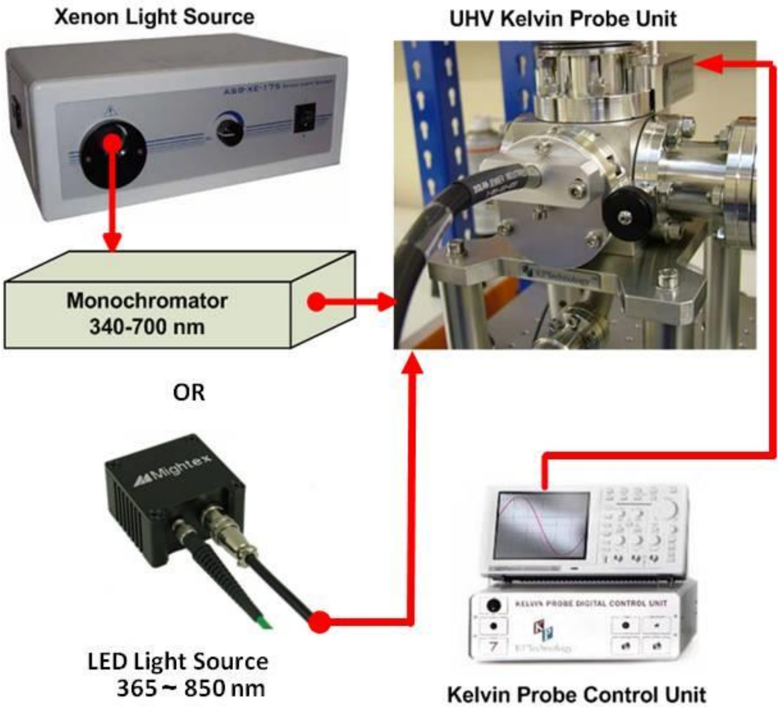

Figure 3.2 Overview of the Kelvin probe system (from KP Technology).

The optical system consisted of an ASB-XE-175 Xenon Fiber Optic Light Source and a linear variable filter with the wavelength range between 340 nm and 700 nm coupled by Oriel VIS liquid light guides. Meanwhile, a switchable high-power LED source from UV (365 nm) to near infrared (850 nm) was also incorporated as an alternative. In the SPS measurement, the CPD is defined as

$$e \cdot CPD = Ws - Wm \qquad (3.1)$$

where Ws is the surface work function of sample powders and Wm is Kelvin probe work function, which was calibrated on Au surface. The ΔCPD is defined as

$$\Delta CPD = CPD_{\text{in dark}} - CPD_{\text{under illumination}} \qquad (3.2)$$

Since the work function of the probe does not change under illumination, it is assumed that

$$e \cdot \Delta CPD = \Delta Ws = - e\, \Delta Vs = - e \cdot SPV, \qquad (3.3)$$

where ΔVs is the change of surface potential, which is the surface photovoltage (SPV) measured in the Kelvin probe system.

3.3 Photocatalytic tests

Photocatalytic activities of the *m*-$BiVO_4$ particles were evaluated by degradation of Rhodamine-B (RhB) in aqueous solution under visible light. Ten fluorescent lamps (8 W × 10) were used with a 400-nm cutoff filter to provide only visible-light irradiation. The illuminance was around 1200 lux, which is about the typical lighting level in office. In each individual photocatalysis experiment, 0.1 g of the as-prepared $BiVO_4$ powder sample was added into 50 ml RhB solution (15 µM). Before irradiation, the solution was stirred in dark condition for at least 4 hours to ensure saturation of RhB adsorption on the photocatalyst powders. During photocatalytic test under irradiation, around 3 ml RhB solution was taken out at given time intervals, to check the absorbance at 553 nm using the Shimadzu UV-2450 UV-Vis spectrometer. The ratio (C_t/C_0) of RhB concentrations after reaction for time *t* (C_t) and at the initial (C_0) was adopted to evaluate the photocatalytic performance. The RhB degradation efficiency η, after irradiation time *t* was calculated by the following:

$$\eta = \frac{C_0 - C_t}{C_0} \tag{3.4}$$

In addition, by plotting $\ln(C/C_0)$ versus the irradiation time (*t*), the first order reaction constant in the dye degradation could be derived from the tangent of the curves:

$$\ln(\frac{C_t}{C_0}) = -kt\,. \tag{3.5}$$

Chapter 4. pH-directed $BiVO_4$ Synthesis Mechanism and Product Morphology

4.1 Introduction

Up to now, there have been a lot of morphologies of $BiVO_4$ powders achieved under different reaction conditions, such as polyhedral and rod-like morphologies [15], micro-tubes single crystal structure [78], and flower-like $BiVO_4$ mesocrystals [79]. However, the discussion on the reaction mechanism over a wide pH range has seldom been reported [78,80]. Especially, there was not enough attention paid to the influence of Bi precursor on the product morphology of $BiVO_4$ particles by aqueous method. In addition, although some morphologies could demonstrate higher specific surface area of $BiVO_4$ powders, there might also be more surface defects introduced resulting in lower photocatalytic performance. Meanwhile, it has been reported that the photocatalytic performance of $BiVO_4$ powders can be greatly influenced by the variation of electronic structure through the slight change of V-O bond length [15]. Thus, the optimization of crystalline structure, morphology and electronic structure of $BiVO_4$ powders still remains a great challenge to enhance their photocatalytic performance.

In this chapter, the hydrothermal synthesis of *m*-$BiVO_4$ in aqueous solution over a wide pH range from 0.4 to 12 is investigated. The evolution of various morphologies of *m*-$BiVO_4$ particles are discussed in terms of the reaction mechanisms involved and the states of Bi precursors presented. The factors affecting the photocatalytic performance are also discussed.

For the sample synthesis, before the mixed solution was transferred into autoclave, the pH of the suspension was adjusted from 0.4 to 3, 5, 7, 9, 11 and 12 with NaOH solution (1 M), and the as-prepared samples were named as BVO-*x* (*x* = 0, 3, 5, 7, 9, 11 and 12) respectively, as described in Table 4.1.

Table 4.1 Sample name, the solution pH values in corresponding synthesis and resultant crystal phase of the as-prepared *m*-$BiVO_4$ powder samples.

Sample Name	pH Value in Synthesis Solution	Crystal Phase in Resultant Powders
BVO-0	0.4	*m*-$BiVO_4$
BVO-3	3	*m*-$BiVO_4$
BVO-5	5	*m*-$BiVO_4$
BVO-7	7	*m*-$BiVO_4$
BVO-9	9	*m*-$BiVO_4$
BVO-11	11	*t*-$BiVO_4$
BVO-12	12	Bi_2O_3 –based complex

4.2 The crystalline structure of $BiVO_4$

The crystal structure of the $BiVO_4$ samples prepared in aqueous solution with various pH values were studied by the XRD analysis as shown in Figure 4.1. It was seen that pure phase of *m*-$BiVO_4$ (JCPDC No. 14-0688) could be successfully obtained in the pH range from 0.4 to 9. The characteristic splitting of peaks at around 19º and 35º of 2θ angles is a clear evidence to differentiate the monoclinic phase from the tetragonal structure (JCPDC No. 48-0744) [80]. When the synthesis was conducted in a solution with pH = 11, the resultant powders were mainly composed of tetragonal zircon $BiVO_4$ (JCPDC No. 14-0133) without much quantity of *m*-$BiVO_4$ phase. For synthesis in stronger alkaline condition (pH = 12), the XRD pattern of collected solid precipitates could not match with any crystal structures of $BiVO_4$ polymorphs. Instead, they were attributed to the complex mixture of many bismuth oxides, oxynitrates, subnitrates, etc. Based on the XRD characterization, it was concluded that both acid and relatively neutral solution (pH ≤ 9) are favorable for the formation of *m*-$BiVO_4$ in hydrothermal process, which is consistent with the reported pH region, although different temperatures were applied in their works [15,116].

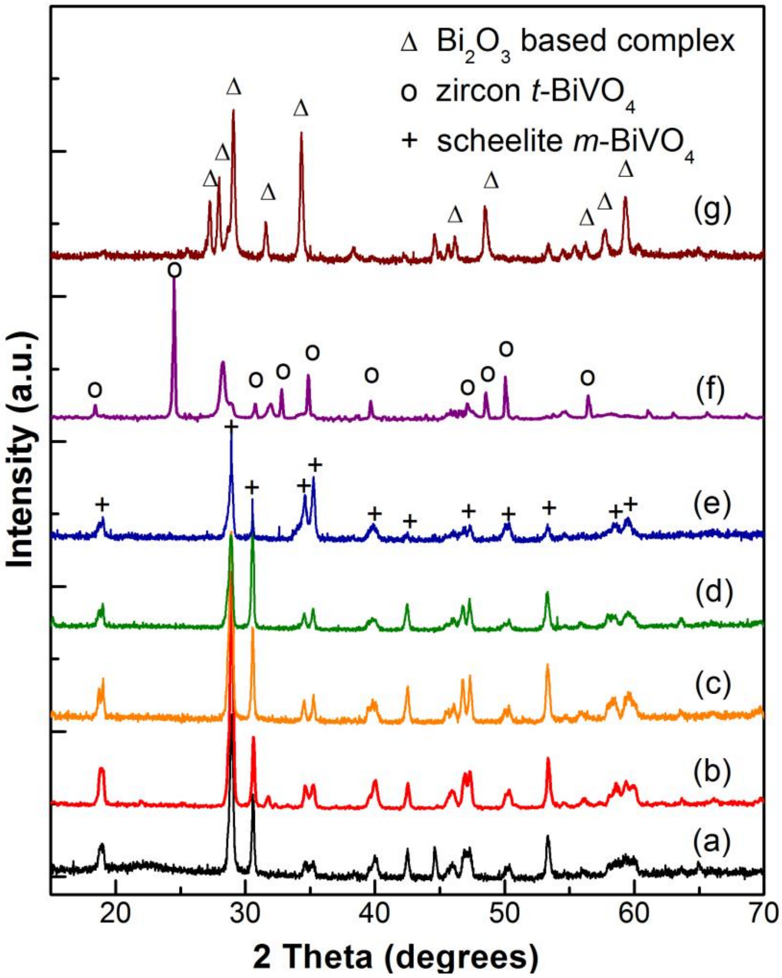

Figure 4.1 XRD patterns of the as-prepared samples (a) BVO-0, (b) BVO-3, (c) BVO-5, (d) BVO-7, (e) BVO-9, (f) BVO-11 and (g) BVO-12.

4.3 The morphologies of $BiVO_4$

Figure 4.2 shows SEM images of the as-prepared *m*-$BiVO_4$ samples fabricated hydrothermally in aqueous solution with different pH values of 0.4, 3, 5, 7 and 9.

Apparently, the morphology of successfully prepared *m*-$BiVO_4$ is strongly related to the pH value of the precursor solution. It is seen that sample BVO-0 exhibited peanut-like morphology with the particle size about 2-3 μm in length and ~ 1 μm in maximum diameter. Meanwhile, when the precursor solution became weakly acidic (pH = 3 and 5), the morphology of the as-prepared samples BVO-3 and BVO-5 have resulted in dendrite shapes, whose hyper-branched structure was composed of a trunk with some ordered branches on the side. For the sample BVO-3, the length of the trunk was about several microns, and for the branches the length ranged from 500 nm to 1 μm. By comparison, the particles of sample BVO-5 were even smaller and thinner with nano-sizes. For the sample BVO-7 synthesized in neutral solution, the particles morphology grew into leaf-like about 10 μm in size and 1 μm in thickness. On the contrary, if synthesized in a soft alkaline solution (pH = 9), flower-like morphology with layered structure was typical for the resultant *m*-$BiVO_4$ particles.

In this work, it was noted that the pH value of the precursor solution plays an important role in controlling the final morphology of the as-prepared *m*-$BiVO_4$ particles. As a matter of fact, this can be associated with the different Bi-precursors after the hydrolysis of bismuth nitrate salts in an aqueous solution. Although some morphologies of *m*-$BiVO_4$ powders, such as dendrites and flower-like, have been reported, the association between product morphology and pH value of synthesis solution has not been sufficiently discussed. In this present work, it was proposed that the morphology of as-prepared *m*-$BiVO_4$ powders is determined by the state and/or morphology of the Bi-precursors presented in the solutions with different pH values. This would result in different reaction mechanisms and morphology evolutions as discussed in the following parts.

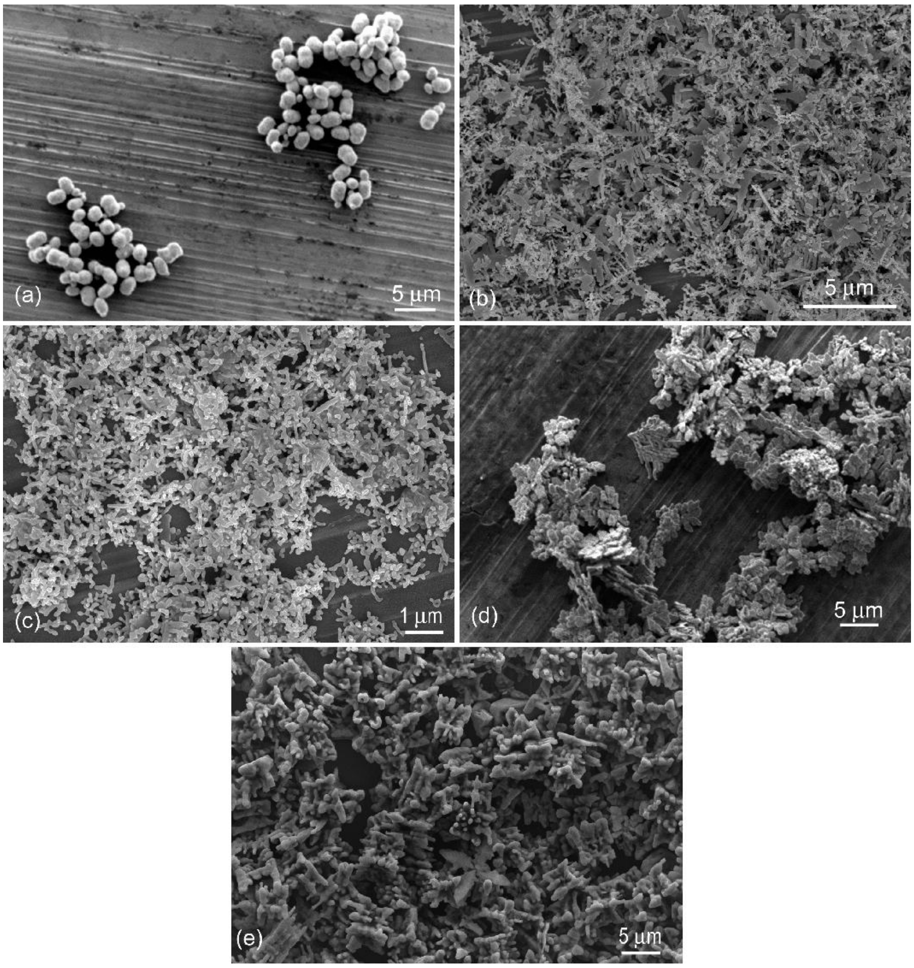

Figure 4.2 SEM images of as-prepared *m*-BiVO$_4$ powders (a) BVO-0, (b) BVO-3, (c) BVO-5, (d) BVO-7 and (e) BVO-9.

In strong acid solution with pH < 1, Bi^{3+} is soluble and the hydrolysis of bismuth nitrate is suppressed. Hence bismuth ions would directly react with VO$_3^-$ during the hydrothermal process, which is regarded as an ionic reaction (Equation 4-1). In this way, the formation of *m*-BiVO$_4$ in the homogeneous solution is simply a solidification process (from supersaturated liquid), followed by agglomeration and Ostwald ripening [117], and the morphology evolution is not restricted by the precursors. Based on such "bottom-up" synthesis, the as-prepared *m*-BiVO$_4$ crystals result in spherical or peanut morphology with uniform size. Subsequently, although the original BiVO$_4$ nuclei can be considerably small in size, crystal growth should be fast due to the great amount of nuclei and sufficient supply of Bi^{3+} and VO_3^- in ambient solution. As a consequence, the as-prepared $BiVO_4$ powders can result in relative large and uniform particle size.

$$Bi^{3+} + VO_3^- + 2OH^- \rightarrow BiVO_4\downarrow + H_2O \qquad (4\text{-}1)$$

At pH > 1, the state of Bi-precursors are dominated by the hydrolysis of bismuth nitrate [118]. Thus, the synthesis of *m*-$BiVO_4$ undergoes different reaction mechanisms, and the final morphology of product is strongly dependent on the morphology of Bi-precursors. In dilute acid solution ($1 < pH < 7$), the hydrolysis of $Bi(NO_3)_3{\cdot}5H_2O$ results in the formation of $BiONO_3$ flocculent precipitates. When $pH \geq 7$, a more intensive and complicated hydrolysis occurs. The precipitates may compose of hydroxides and many other Bi complexes such as oxynitrates, subnitrates, hydroxide nitrate, etc. according to different precipitation conditions [119]. In these two cases, the formation of *m*-$BiVO_4$ can be regarded as solid-liquid reactions as indicated in equations (4-2) to (4-5):

$$Bi(NO_3)_3 + H_2O \rightarrow BiONO_3\downarrow + 2H^+ + NO_3^-; \qquad (4\text{-}2)$$

$$BiONO_3\downarrow + VO_3^- \rightarrow BiVO_4\downarrow + NO_3^-; \qquad (4\text{-}3)$$

$$Bi(NO_3)_3 + 3OH^- \rightarrow Bi(OH)_3\downarrow + 3NO_3^-; \qquad (4\text{-}4)$$

$$Bi(OH)_3\downarrow + VO_3^- \rightarrow BiVO_4\downarrow + OH^- + H_2O; \qquad (4\text{-}5)$$

During the hydrothermal process, the displacement reaction takes place at the solid-liquid interface and the morphology of the final products evolve from those of the solid Bi precursors. For $1 < pH < 7$, the Bi precursors after hydrolysis are of $BiONO_3$ thin sheets or belts, as shown in Figure 4.3 (a). Next, the replacement of the anions can be considered as a 2D etching process along certain crystal direction. Therefore, the $BiONO_3$ thin sheets gradually transform into *m*-$BiVO_4$ dendrites. For $pH \geq 7$, the Bi precursors (hydroxides-based complex) are thick and dense plates, as shown in Figure 4.3 (b). Thus, the displacement reaction moves from the solid surface into the inner parts, like a 3D etching. As a result, the structure evolves into thick leaf or flower-like morphologies for the final *m*-$BiVO_4$ products.

For both conditions, there are hardly any Bi ions soluble in the solution, and the nucleation happens at the surface of large Bi-precursor precipitates. Therefore, intensive size growth may not be involved and the particle size of resultant *m*-$BiVO_4$ particles is directly dependent on the original size of the Bi-precipitates.

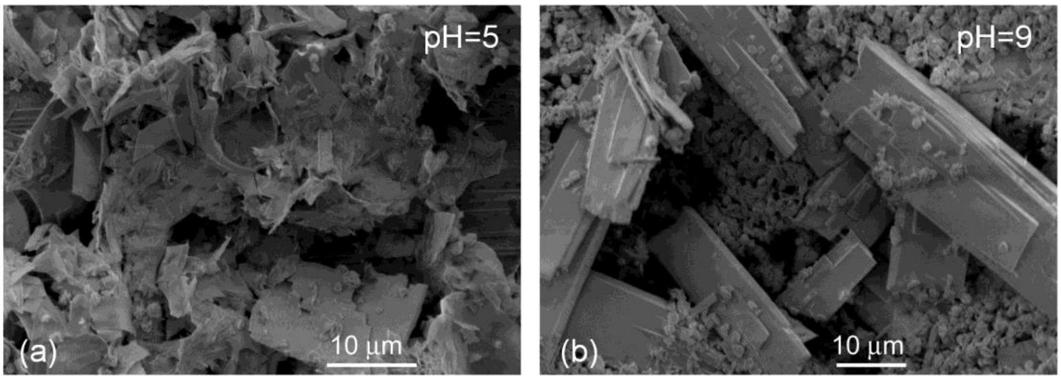

Figure 4.3 SEM images of different Bi-precursors (a) $BiONO_3$ pH = 5 (b) $Bi(OH)_3$-based complex in pH = 9.

The morphology evolution regarding different pH value in the reaction solution is illustrated in Figure 4.4. In addition, based on above discussion, it can be concluded that once the precipitation formed for Bi-precursors, it is relatively difficult for size control and morphology modification of the final product. On the contrary, it would be applicable to achieve small particles with desired morphology for the as-prepared *m*-$BiVO_4$ particles in strong acid solution with $pH < 1$ through synthesis control and/or the addition of template materials.

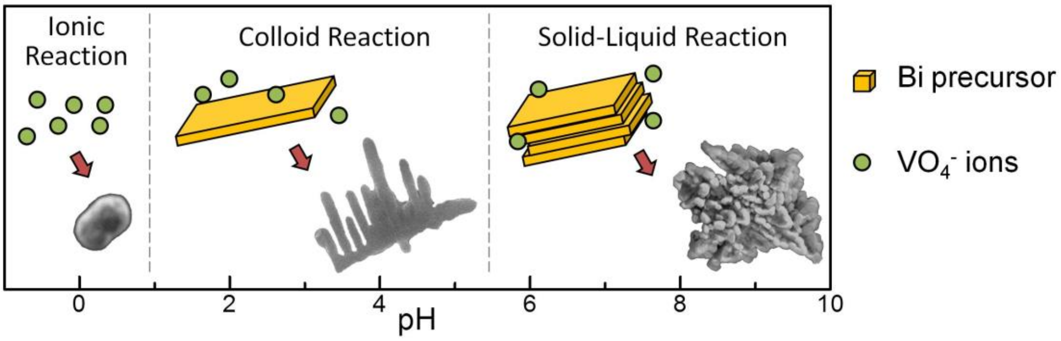

Figure 4.4 Schematic illustration on the formation mechanism of the *m*-$BiVO_4$ particles in the solution with different pH values.

4.4 The photo-physical properties of $BiVO_4$

The photocatalytic performance of the as-prepared *m*-$BiVO_4$ samples were evaluated by the photodegradation of RhB under visible light irradiation as shown in Figure 4.5, and after 24 hours irradiation, the overall degradation efficiencies of each sample are listed in Table 4.2. It is clearly seen that all these *m*-$BiVO_4$ powders exhibited superior photocatalytic activity under visible light. In addition, sample BVO-0 with peanut-like morphology showed best performance with fastest degradation rate among these samples.

Table 4.2 Band gap energies, BET surface area values, Stretching Raman shift V–O bonds, RhB degradation efficiencies after 24 hours and particle morphologies of the as-prepared *m*-$BiVO_4$ powder samples.

Sample Name	Band-gap Energy (eV)	BET Surface Area Value (m^2/g)	Stretching Raman Shift V–O Bonds (cm^{-1})	Degradation Efficiency of RhB (%)	Particle Morphology
BVO-0	2.26	2.50	826.7	75	Peanut-like
BVO-3	2.36	6.47	806.5	52	Dendrite-like
BVO-5	2.40	8.79	807.1	47	Dendrite-like
BVO-7	2.32	0.95	802.4	42	Leaf-like
BVO-9	2.28	0.94	803.9	50	Flower

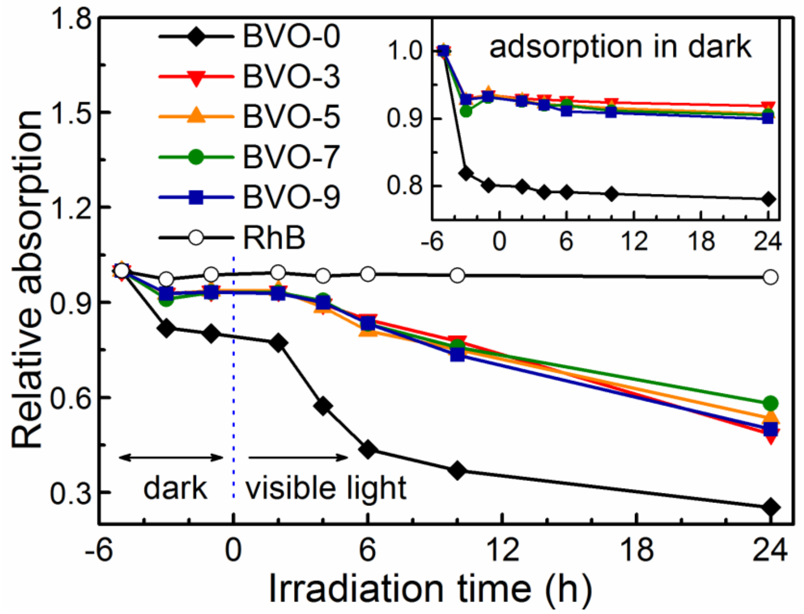

Figure 4.5 The photocatalytic degradation of RhB for as-prepared *m*-BiVO$_4$ samples.

Primarily, the band-gap-energy (E$_g$) associated optical absorption performances of the as-prepared monoclinic BiVO$_4$ powders were evaluated as shown in Figure 4.6. It is found that all the five samples exhibit absorption bands in the visible light region with the estimated E$_g$ values around 2.26 ~ 2.4 eV, which is characteristic for the reported *m*-BiVO$_4$ particles [15,116,120]. Such small E$_g$ ensures the efficient optical absorption for high photocatalytic property in degradation of organic dyes under visible light illumination. Furthermore, the specific surface area of these powder samples were analyzed using BET method. Due to different micro morphologies, these samples resulted in a wide range of specific surface area. Especially, the dendrite-shaped sample (BVO-5) possessed large specific surface area, which was about 10 times larger than that of BVO-7 and BVO-9. However, although higher specific surface area is favorable for better photocatalytic property [116], it is noted that the degradation efficiency of BVO-5 and BVO-3 was still poorer than that of BVO-0. One of the reasons can be proposed that, the dendrite or branched morphology of these two samples may also involve great amount of surface structural defects, where the high energy dangling bonds could be attached with impurity atoms and molecules. This usually happens at the tip or corner of the dendrite particles. It is well recognized that structural defects can also act as the recombination center of electron-hole pairs, which drastically decreases the overall photocatalytic performance of a material [10].

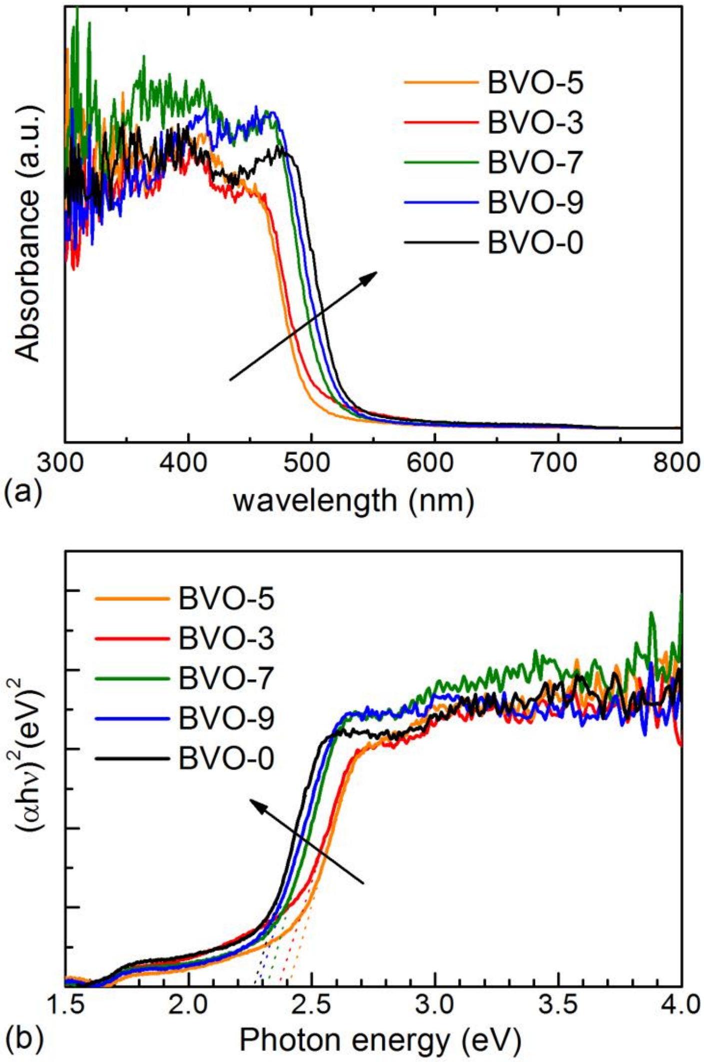

Figure 4.6 (a) UV-Vis diffused reflectance spectra and (b) plots of $(\alpha h\nu)^2$ versus photon energy ($h\nu$) of the as-prepared $BiVO_4$ samples.

Moreover, the significant difference in the photocatalytic properties can also be associated with the local structure variation of these as-prepared *m*-BiVO$_4$ powders. According to the reported simulation of *m*-BiVO$_4$, the valence band is formed by a hybrid of the Bi 6s and O 2p orbitals, while the conduction band is composed of V 3d orbitals [66]. The higher level distortion of Bi-O tetrahedron leads to more orbital overlap, which can support a better transportation of holes in the valence band. As a result, it improves the electron-hole pair separation and benefits the photocatalytic performance [15]. This is also the reason that the monoclinic BiVO$_4$ exhibits better photocatalytic property than the tetragonal phase. For the monoclinic BiVO$_4$ phase, a less distortion corresponds to the tendency towards tetragonal phase, thus, exhibits slightly poorer photocatalytic performance.

According to our study, normal XRD characterization can only give a rough indication of *m*-BiVO$_4$, while the tiny variation of local structure can be verified by the Raman spectroscopy through directly analyzing the vibrational bands of materials. As shown in Figure 4.7 (a), the Raman bands at around 800 ~ 826 cm^{-1} corresponds to one type of V–O bonds of *m*-BiVO$_4$. It is found that, compared with that of BVO-0, the Raman peaks of other samples shifted to lower frequencies. This red-shift of the Raman stretching band corresponds to the longer V–O bond lengths and is considered to give the less distortion of the VO$_4^{3-}$ tetrahedron in the local structure. Therefore, it can be expected that for sample BVO-3~BVO-9, less distortion in the local structure results in their lower photocatalytic performance than that of the sample BVO-0. This can be illustrated in Figure 4.7 (b), where the overall degradation efficiency, after 24 h degradation of RhB, of the *m*-BiVO$_4$ powder samples are plotted as a function of stretching Raman shift V–O bonds.

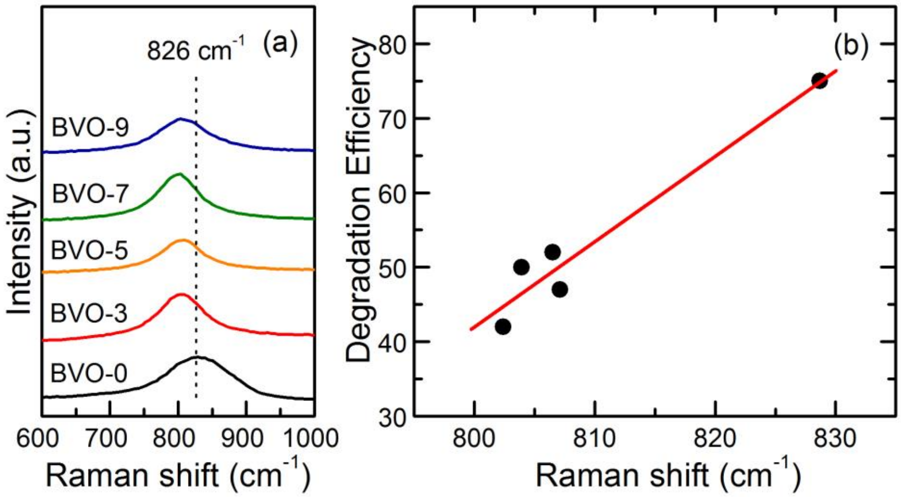

Figure 4.7 (a) Raman spectra and (b) the dependence of the RhB degradation efficiency on stretching Raman shift V–O bonds of as-prepared *m*-$BiVO_4$ samples.

Based on the above discussion, the better photocatalytic performance of BVO-0 than other samples can be summarized as follows: Firstly, it is mostly attributed to its perfect monoclinic structure. Based on our investigation, it can be concluded that higher pH synthesis tends to form tetragonal zircon $BiVO_4$. Although the products from both acid and relatively neutral solution ($pH \leq 9$) can be classified as *m*-$BiVO_4$ by XRD characterization, we found that perfect monoclinic scheelite structure can only be obtained in strong acid condition (pH=0). This can be identified by Raman spectroscopy, where perfect monoclinic structure corresponds to the high level distortion of Bi-O tetrahedron. This ensures the better separation of the excited electron-hole pairs for higher photocatalytic performance. Hence in this work, among these five samples BVO-0 ~ BVO-9, BVO-0 exhibits the perfect monoclinic structure, and thus has the best degradation performance.

Secondly, BVO-0 also exhibits quite high specific surface area (2.5 m^2/g), which is necessary for the dispersion and efficient photocatalytic reaction. For BVO-3 and BVO-5 with even higher specific surface area values, their dendrite morphology may also involve large amount of surface defects, in terms of high dangling bonds attached with impurity atoms and molecules. These may affect the surface red-ox reaction in a photocatalyst test by dye degradation.

4.5 Concluding remarks

In summary, monoclinic scheelite structure $BiVO_4$ particles with various morphologies were synthesized by a simple hydrothermal method in aqueous solution with pH value ≤ 9. Due to different reaction mechanism under various pH values, the state and morphology of Bi-precursor played crucial roles in determining the particle size and morphology of the final *m*-$BiVO_4$ products. Given the small band gap values for visible light response, 2.26 ~ 2.40 eV, these as-prepared *m*-$BiVO_4$ powders showed superior photocatalytic performance in the degradation of RhB under visible light irradiation. In addition, the degradation efficiency was found to be greatly influenced by the specific surface area and the local structure variation. Among these samples, BVO-0, synthesized in pH = 0.4 aqueous solution, exhibited the highest degradation efficiency. And for BVO-3 and BVO-5, despite larger specific surface area, their shorter V–O bond corresponded to less distortion of the VO_4^{3-} tetrahedron in the local structure, which results in lower photocatalytic performance.

Chapter 5. Mono-Dispersed *m*-$BiVO_4$ Octahedral Single Crystals

5.1 Introduction

Based on the study in chapter 4, strong acid condition is found favorable for morphology and particle size control. So in this chapter, a modified hydrothermal synthesis with solution pH<1 is carried out, in order to further control the product morphology and particle size for photocatalytic performance enhancement.

It is well recognized that good crystallization with less structural defects, as well as high specific surface area, are usually required to achieve excellent photocatalytic performance, in accordance to the photocatalytic kinetics [11-14]. The synthesis of $BiVO_4$ with various morphologies has been achieved in the presence of organic additives or surfactants, such as one-dimensional (1D) nanofibrous [74], two-dimensional (2D) nanosheets [75] and hierarchical frameworks [121], with enhanced photocatalytic performance. In addition, photocatalytic properties were found strongly related to the preferred crystallographic facets as well. For example, ZnO nanodisks with (001) face demonstrated excellent photo degradation of methylene blue [122]. Also, {001} facets of TiO_2 single crystals was reported to show superior photocatalytic performance for the degradation of 4-chlorophenol [123]. Moreover, Xi et al reported that monoclinic $BiVO_4$ nanoplates, with highly exposed (010) face, have led to the dramatic enhancement of visible light photocatalytic oxidization reactivity [11], and higher O_2 evolution rate [12]. All of these results indicated that good crystallization and appropriate crystal-facet control of the photocatalysts are of essential importance for photocatalytic performance enhancement.

In this chapter, we report for the first time the successful synthesis of mono-dispersed *m*-$BiVO_4$ octahedral single crystals by hydrothermal route. These single crystals octahedrons exhibit uniform sizes with good crystallization and possess $\{120\}$ and $\{021\}$ facets with clean surfaces. The time-dependent crystal evolution and the growth mechanism are investigated based on the electron microscopy. The photodegradation of RhB is used to evaluate the photocatalytic activities of these octahedral *m*-$BiVO_4$ crystals under visible light irradiation.

The synthesis procedure in the last chapter was slightly modified as follows: 0.1 g sodium dodecyl benzene sulfonate (SDBS) was dissolved in 2 M nitric acid solution separately. It was then mixed together with Bi and V solution, followed by vigorous stirring to obtain a clear orange solution. Appropriate amount of deionized (DI) water and 2 M nitric acid (if applicable) were also added to the prepared solution to adjust the acid concentration from 0.8 M to 1.5 M. In this strong acid condition, both Bi and V precursors were soluble to form a homogeneous solution.

5.2 The crystalline structure of m-$BiVO_4$

Figure 5.1 presents the typical XRD pattern of the as-prepared *m*-$BiVO_4$ products, which can be well-indexed with the pure phase of monoclinic $BiVO_4$ (JCPDC No. 14-0688). Moreover, the peak splitting around 19° and 35° of 2θ angles, zoomed in the insets in Figure 5.1 gives a clear evidence to differentiate the monoclinic phase of synthesized products from the tetragonal structure (JCPDC No. 48-0744) [80].

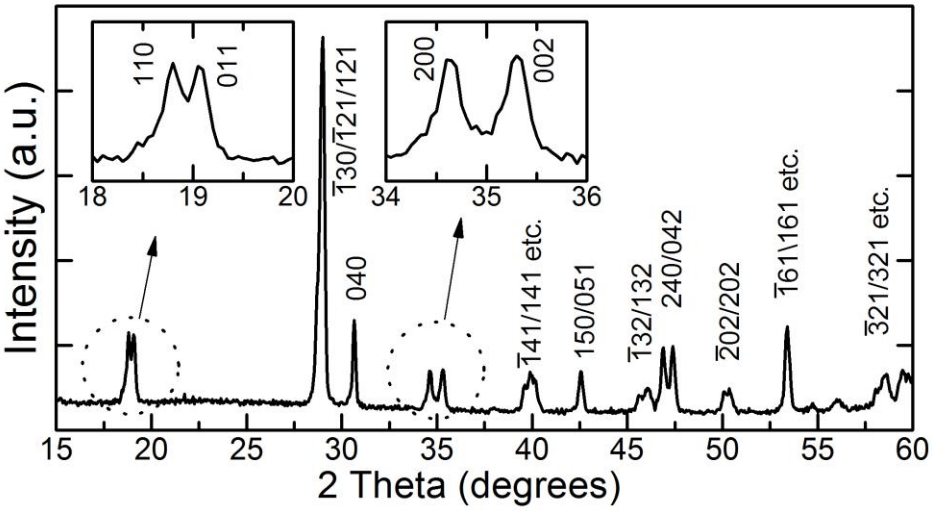

Figure 5.1 Typical XRD pattern of *m*-$BiVO_4$ as-prepared nano-particles. The insets are zoomed XRD patterns near 19° and 35°, respectively.

From the SEM images in Figure 5.2 (a) and (b), it can be seen that $BiVO_4$ particles tended to develop into octahedral crystals in the presence of SDBS. Furthermore, these $BiVO_4$ octahedral particles were mono-dispersed with uniform size distribution, and possessed a smooth surface and sharp edges. The size of as-prepared *m*-$BiVO_4$ octahedra was controllable depending on the synthesis parameters, such as concentration of precursors, acid concentration and reaction time, which is detailed further. The EDX analyses of these octahedral particles showed the calculated Bi: V elemental ratio of 51.1: 48.9, which is close to the theoretical stoichiometric ratio of $BiVO_4$. For comparison, the $BiVO_4$ particles were also synthesized at the same conditions without the presence of SDBS. As shown in Figure 5.2 (c) and (d), the shape of obtained $BiVO_4$ particles was irregular with non-evenly distributed particle size. It indicated that the addition of SDBS surfactant has played a crucial role in the morphology evolution of as-prepared *m*-$BiVO_4$ particles.

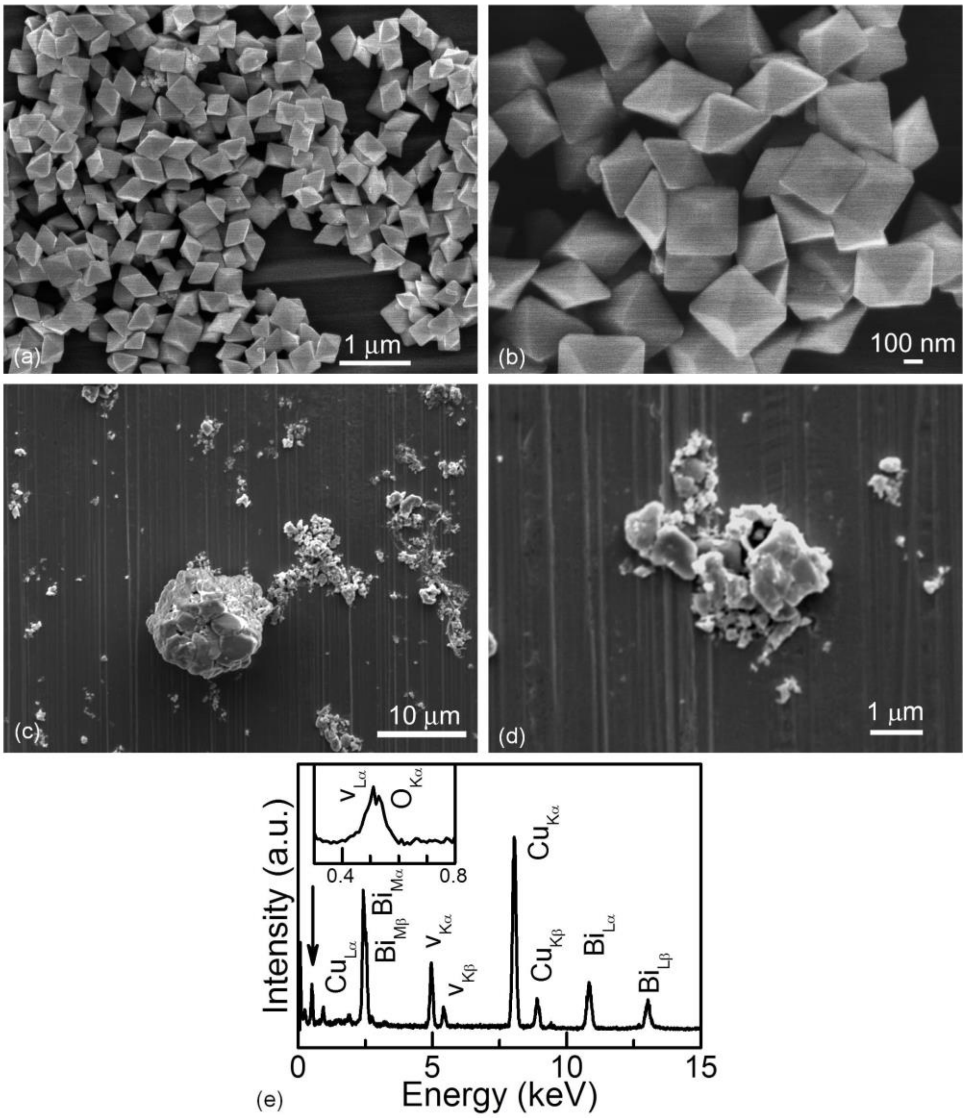

Figure 5.2 (a) low-magnification SEM image, (b) high-magnification FESEM image and (d) EDX spectrum of the as-prepared *m*-$BiVO_4$ octahedral single crystals compared with (c) and (d) the SEM image of the sample synthesized without SDBS. The inset in (e) shows the expanded closely spaced signal peaks of the V and O elements in the EDX spectrum.

5.3 The morphologies of m-$BiVO_4$

The crystal structure and orientation of the *m*-$BiVO_4$ octahedra were further investigated by TEM-SAED observation. Figure 5.3 illustrates the morphology, SAED patterns and lattice images of *m*-$BiVO_4$ octahedra observed along different zone axes. All the SAED patterns were well matched to the single-crystalline structure of *m*-

$BiVO_4$ as indicated in Figure 5.3 (a) (c) and (e), respectively. These SAED patterns clearly indicated that each mono-dispersed octahedron was composed of *m*-$BiVO_4$ single crystal. In particular, the angle about 90.4° between (200) and (002) in the SAED pattern in the inset of Figure 5.3 (a) was consistent with the monoclinic phase (β = 90.38º), which has slight deviation from the scheelite tetragonal structure of (s-t) $BiVO_4$ (β = 90º). Moreover, these octahedral crystals were of high crystalline quality with flat and clean surface morphology. The corresponding HRTEM images were taken at the edge of each *m*-$BiVO_4$ octahedron, as shown in Figure 5.3 (b), (d) and (f), respectively. The facets and orientation of the *m*-$BiVO_4$ single crystal octahedron were further determined by combination of TEM-SAED analysis along different crystal zone-axes. If the crystal was tilted with the TEM zone axis perpendicular to the four edges, the diffraction spots of (200) and (002) indicated that these edges were along [100] and [001] directions, as shown in Figure 5.3 (a) and its inset. Figure 5.3 (b) indicates the *d*-spacing values measured from SAED (zone axis [010]) are 2.55 Å and 2.60 Å, which well agree with the lattice spacing values, 2.546 Å and 2.598 Å for (002) and (200) of monoclinic $BiVO_4$, respectively, in the XRD pattern. When the crystal was tilted to a zone axis parallel to a crystal surface while perpendicular to one of its edges, as shown in Figure 5.3 (e) (left border) and its inset, according to the diffraction spots of $(0\bar{4}2)$ and (200) reflections, the corresponding surface facet and crystal edge were determined as $(0\bar{2}1)$ plane and [100] direction, respectively. From the three groups of TEM-SAED images, it can be concluded that the surface of the octahedral *m*-$BiVO_4$ crystal was composed of {120} and {021} facets. And from the centre of each octahedron, the six corners are pointing along [101], $[\bar{1}01]$, $[10\bar{1}]$, $[\bar{1}0\bar{1}]$, $[0\bar{1}0]$, and [010] directions, respectively. A schematic illustration of the crystal orientation of an *m*-$BiVO_4$ octahedron is shown in Figure 5.4.

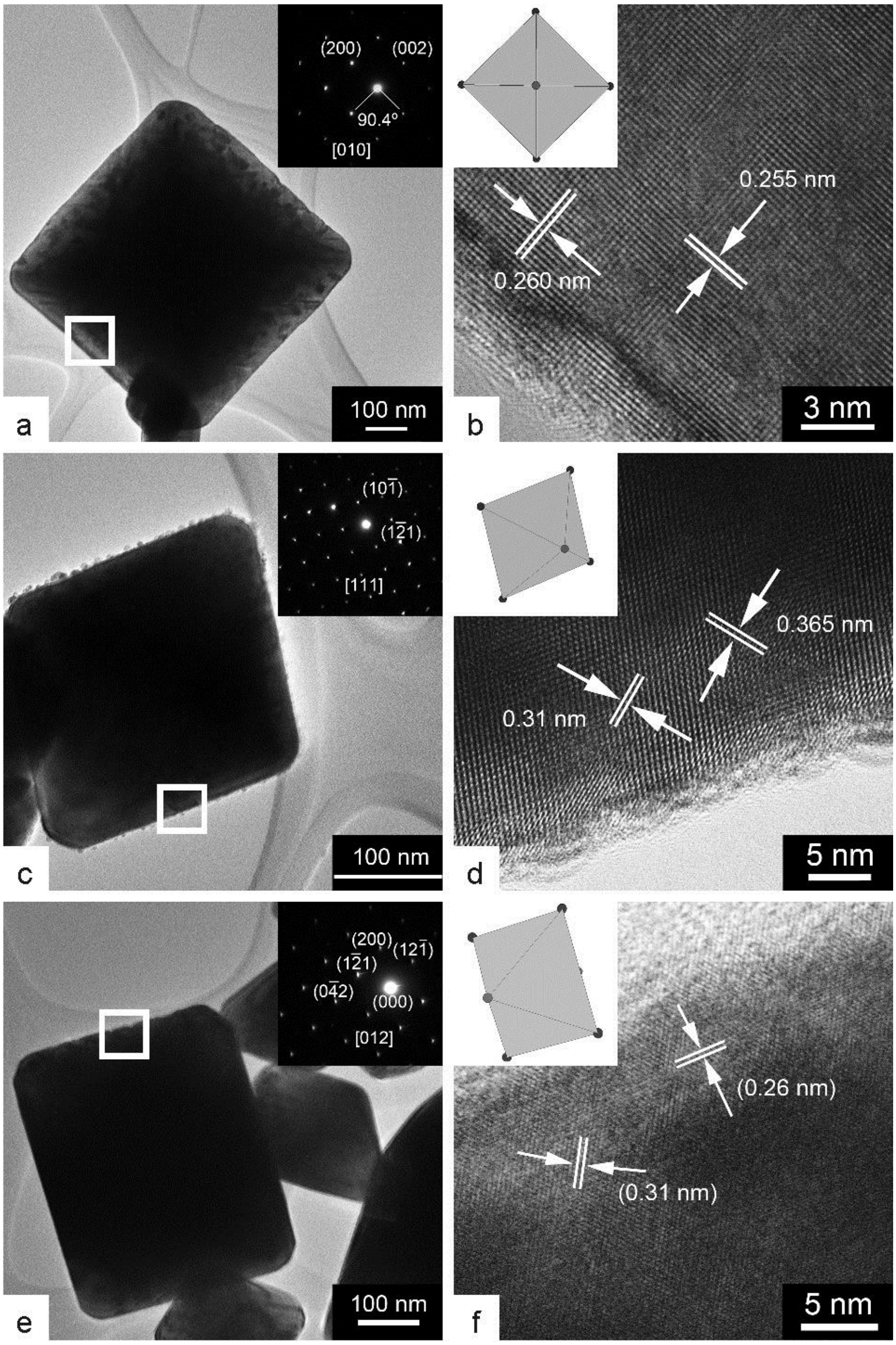

Figure 5.3 (a), (c) and (e) TEM images of as-prepared single-crystalline *m*-$BiVO_4$ octahedra, with the insets showing the corresponding SEAD patterns observed along different zone axes. The HRTEM images (b), (d) and (f) were taken from the edge of the crystals in Figure 5.3 (a), (c) and (e), respectively, with the insets giving the schematic illustrations of the octahedra with the corresponding angles. (The closed circles in the illustrations indicate the corners of the octahedral).

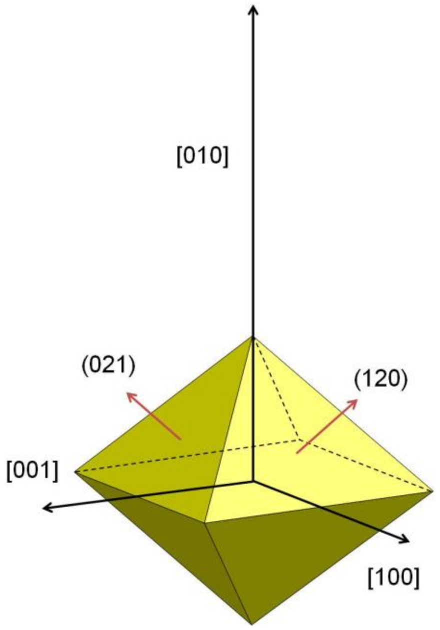

Figure 5.4 Schematic illustration of the crystal orientation of the *m*-$BiVO_4$ octahedron with specific facets.

In order to understand the formation mechanism of these mono-dispersed *m*-$BiVO_4$ octahedral single crystals, the effect of reaction time on crystal size control was investigated by hydrothermal reaction from 3 to 48 hours at fixed acid concentration of 1.2 M and the reaction temperature of 150 ºC. In the first 3 h, there was no precipitate found in the autoclave. Then, with reactions from 3 to 24 h, the yield of $BiVO_4$ powders was gradually increased with longer reaction time. After reacting for 24 h, the solution became clear, and the product yield increased no further when extending the reaction time further to 48 h. In morphology, the *m*-$BiVO_4$ octahedral crystals were found to grow larger gradually with reaction time. The size of *m*-$BiVO_4$ crystals after a 6 h reaction was around 100~200 nm as shown in Figure 5.5 (a). These nanocrystals were already mono-dispersed with spherical and polyhedral shapes, indicating that the evolution toward octahedron was incomplete. After a 12 h reaction, the powder product mainly consisted of well-defined 1-3 μm octahedral crystals, as indicated in Figure 5.5 (b); while uniform size of around 3-4 μm of octahedra could be achieved by reacting for 24 h (Figure 5.5 (c)). The crystal size grew further while the reaction was extended to 48 h.

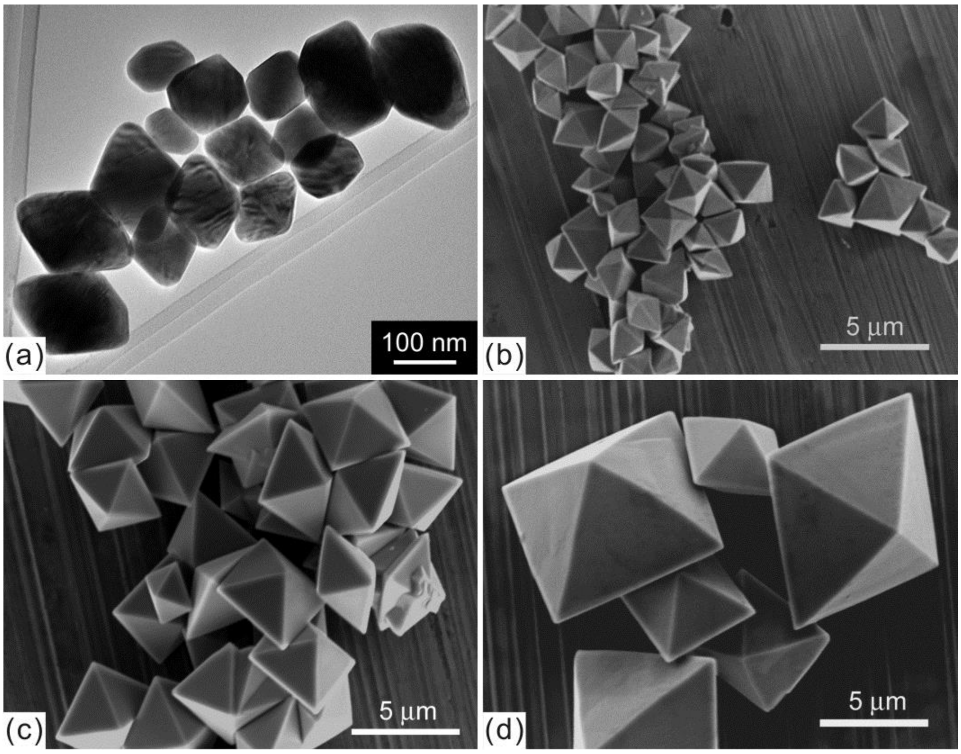

Figure 5.5 SEM images of the *m*-BiVO$_4$ crystals synthesized at different reaction times with fixed acid concentration 1.2 M (a) 6 h, (b) 12 h, (c) 24 h, & (d) 48 h.

Based on these observations, it was concluded that the formation and growth of the octahedral shape is typically a supersaturation process combined with Ostwald ripening [117] at the latter stage. This was consistent with the previous report that *m*-BiVO$_4$ could be successfully synthesized by co-precipitation process in similar acid media, although such a co-precipitation process required a long time (more than a week) without the promotion of high pressure and elevated temperature [124]. Moreover, the strong acid condition was considered to be an essential factor to control the particle size and shape of the final products. In our experiment, the yellow color precursor solution, containing Bi^{3+} and VO$_3^-$ ions, was maintained clear without forming any precipitates before transferred into the autoclave. At pH ≥ 2, hydrolysis of $Bi(NO_3)_3$ would take place to form $BiONO_3$ suspension, giving rise to the solid state phase in the solution [78]. In this case, the formation of *m*-$BiVO_4$ could only take place via the reaction of VO_3^- ions with $BiONO_3$ clusters at the liquid-solid interface. Such a reaction process was relatively difficult for the size control and morphology modification of the final product. Recently, there have been a lot of approaches reported on the synthesis of *m*-$BiVO_4$ particles with various morphologies [75,78,79]. However, the synthesis was mostly processed in aqueous solution with pH > 1, and the efforts towards nano-size and morphology control of *m*-$BiVO_4$ synthesis were limited due to the suspension precursor. In this work, we highlight the essential importance of making a clear precursor solution with pH value below 1 in order to provide a bottom-up synthesis condition to effectively control the particle size and shape of the final products. In this acid condition, Bi^{3+} is soluble and it would directly react with VO^{3-} during the hydrothermal process, which is regarded as an ionic reaction. As shown in Figure 5.7 (a), the surface of ripened octahedral crystal composed of step morphology, which indicates the layer-by-layer growth mode during the crystal growth and Ostwald ripening process. Meanwhile, it is proposed that the *m*-$BiVO_4$ crystals can grow along preferential directions with the assistance of SDBS surfactant. Therefore, without the restraint from the precursor morphologies, an *m*-$BiVO_4$ crystal is able to grow from tiny nuclei into regular octahedron. The growth evolution of an *m*-$BiVO_4$ octahedron is illustrated in Figure 5.6. Compared to the previous synthesis of *m*-$BiVO_4$ in the presence of SDBS [75], the morphology difference of the obtained particles was mostly attributed to the different pH values of the reaction solution.

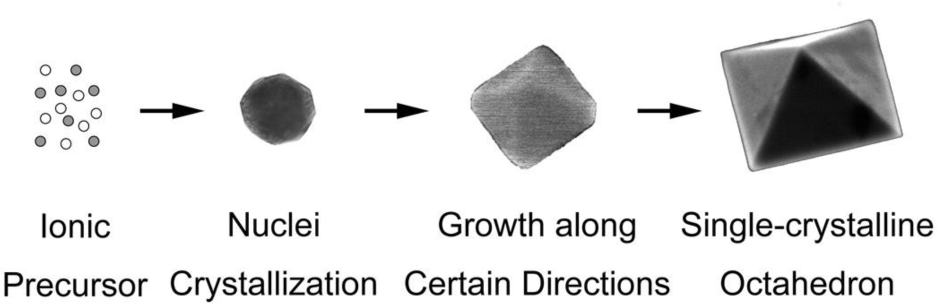

Figure 5.6 Schematic illustration of the proposed growth evolution of an *m*-$BiVO_4$ octahedron.

The above conclusion can be further confirmed by studying the influence of acid concentration on crystal size. This time, the acid concentration was changed from 0.8 M to 1.5 M while keeping the reaction time fixed at 24 hours. Meanwhile, *m*-$BiVO_4$ particles synthesized under pH= 2 were also prepared for comparison. As shown in Figure 5.7, the octahedral crystal size became larger with increasing acid concentration of the solution. The obtained *m*-$BiVO_4$ seed crystals were around 100~200 nm and 500~600 nm in the acid concentration of 0.8 M and 1 M respectively, showing their growth tendency towards octahedral shapes. With the acid concentration increased to 1.2 M, a wider distribution of crystal size was observed, some larger crystals were formed together with the predominantly smaller crystals of around 3~4 μm as shown in Figure 5.7 (b). A further increase of the acid concentration to 1.5 M would result in the formation of larger size octahedra of more than 4 μm as shown in Figure 5.7 (a). In Comparison, the obtained *m*-$BiVO_4$ at pH = 2 demonstrated the dendrites morphology shown in Figure 5.7 (e), which was similar with the structure reported [79]. During the *m*-$BiVO_4$ crystal growth in the latter stage of the reaction, especially the ripening process, mass transportation was dominated by ions in the solutions. Therefore, the crystal growth speed was strongly dependent on the concentration of Bi^{3+} and VO_3^- ions. Our experiment has also indicated that *m*-$BiVO_4$ powders could be totally dissolved in concentrated nitric acid solution (> 4 M), and the solubility of *m*-$BiVO_4$ was found to increase with a higher acid concentration. Thus, when the synthesis was carried out at higher acid concentration, there would be more soluble ions to contribute to the faster crystal growth rate due to the dynamic mechanism, and hence large *m*-$BiVO_4$ octahedra would be obtained. In contrast, crystal size could be successfully suppressed to around 200 nm if synthesized at lower acid concentration, as shown in Figure 5.7 (d).

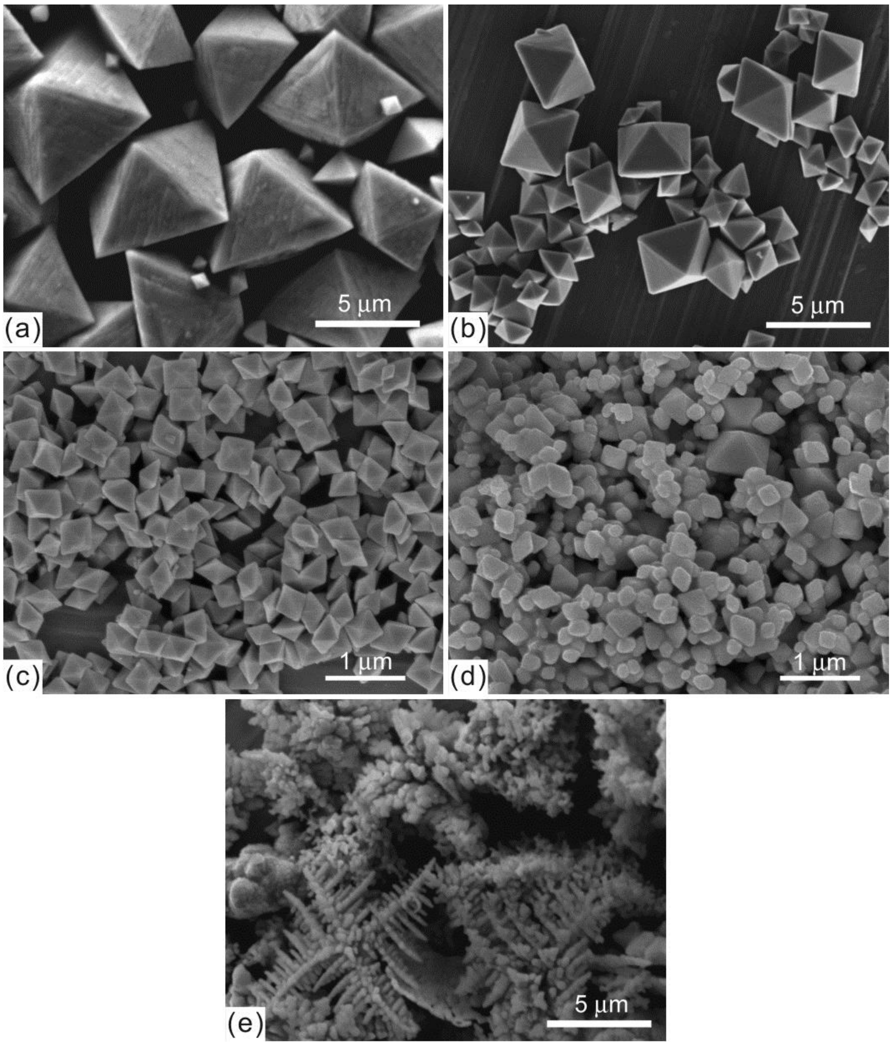

Figure 5.7 SEM images of different acid concentration (fixed reaction time 24 h): (a) 1.5 M, (b) 1.2 M, (c) 1 M, (d) 0.8 M and (e) pH = 2.

5.4 The photo-physical properties of m-$BiVO_4$

The photocatalytic performance of the as-prepared mono-dispersed *m*-$BiVO_4$ octahedral crystals, as well as *m*-$BiVO_4$ sample prepared without SDBS additive (S0), were evaluated by the photodegradation of RhB under visible light irradiation. The tested samples with corresponding synthesis parameter, particle size, specific surface area through BET analyses and geometric calculation, photocatalytic reaction constant K, and band gap energy are listed in Table 5.1. As shown in Figure 5.8 (a), it can be clearly seen that *m*-$BiVO_4$ octahedral crystals showed better photocatalytic performance than the sample S0 with irregular morphology and size distribution by surfactant-free synthesis. Moreover, a smaller octahedral crystal size resulted in a higher photodegradation rate. Among these samples, the sample S4 with 200~300 nm octahedral crystals exhibited the highest activity with fast degradation of RhB within 10 hours under the visible light of normal indoor fluorescent illumination. This result is also consistent with the reaction constant, as shown in Figure 5.8 (b). Such superior photocatalytic activity could be attributed to the good crystallization with less structural defects and preferred crystal facets for surface-controlled photocatalysis.

Table 5.1 Specific surface area, photocatalytic reaction constant k and band gap energy of the samples according to the crystal sizes.

Sample Name	Acid Concen-tration	Crystal Sizes (μm)	BET Surface area (m^2/g)	Calculated Surface area (m^2/g) *	Reaction Constant K (h^{-1})	Band Gap (eV)
S1	1.5 M	4~5	0.30	0.21	0.0488	2.29
S2	1.2 M	1~1.5	1.50	1.06	0.084	2.26
S3	1.0 M	0.5	2.34	2.12	0.2454	2.25
S4	0.8 M	0.2~0.3	3.97	3.53-5.29	0.3783	2.25

*Geometric calculation was done by regular octahedron approximation.

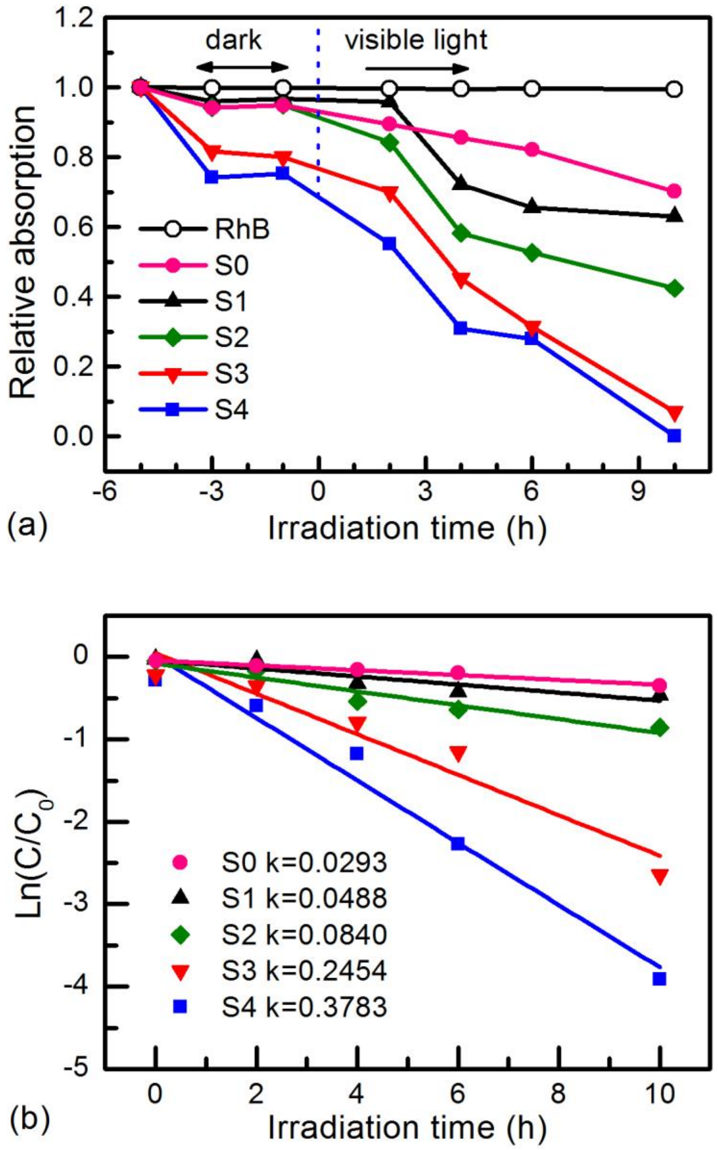

Figure 5.8 (a) The photocatalytic degradation of RhB for *m*-BiVO$_4$ octahedral crystals and (b) First-order plots for the photocatalytic degradation of RhB by samples S1~S4 showing the linear relationship for ln(C/C$_0$) versus irradiation time (t), ln(C/C$_0$) = kt, where C is the concentration of the RhB, C$_0$ is the initial concentration of the RhB, and k is the first order reaction constant.

Additionally, photocatalytic performance was strongly related to the optical absorption property and specific surface area [125]. The UV-Vis diffused reflectance spectra of the as-prepared *m*-BiVO$_4$ powders were collected in order to further investigate the band-gap energy (E_g) values of the octahedral crystals. As shown in Figure 5.9, all the four samples showed absorption bands in the visible light region. The estimated E_g values of all the octahedral crystalline powders were similar, around 2.25 to 2.29 eV, which is characteristic of monoclinic scheelite $BiVO_4$ [10]. Thus, despite different crystal sizes, the band gap of the m-$BiVO_4$ crystals was unlikely to be affected; nor should the optical absorption behavior be influenced. Alternatively, the superior photocatalytic performance of smaller m-$BiVO_4$ octahedra could originate from their higher specific surface area. As shown in Table 5.1, the tested specific surface area of the powder m-$BiVO_4$ octahedra agreed well with the geometric calculation results. With the decrease of crystal size from 5 μm to around 200 nm, a higher specific surface area value of 3.97 m^2/g was achieved, which is among the highest values reported for m-$BiVO_4$ powders [116].

Finally, the recyclability of the as-prepared m-$BiVO_4$ octahedral crystals was also tested, as shown in Figure 5.10. Samples after photodegradation reaction were recollected and dried for the repeat test. It was found that the degradation curves were maintained during the repeated test, indicating the good chemical and photocatalytic stabilities of these mono-dispersed octahedral m-$BiVO_4$ crystals.

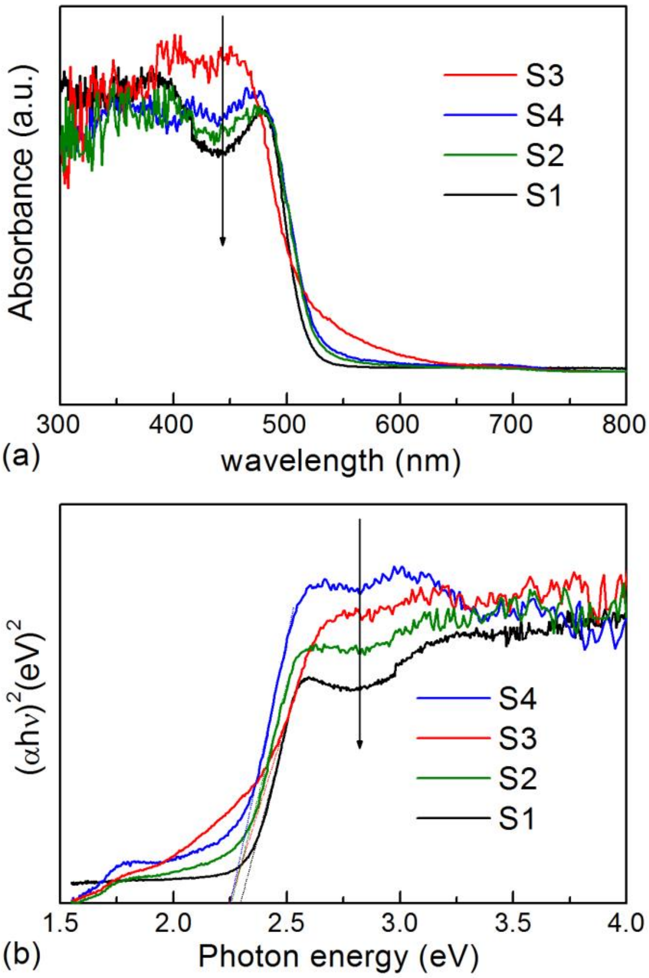

Figure 5.9 (a) UV-Vis diffused reflectance spectra and (b) plots of (αhν)^2 versus photon energy (hν) of the as-prepared *m*-BiVO$_4$ octahedral crystals.

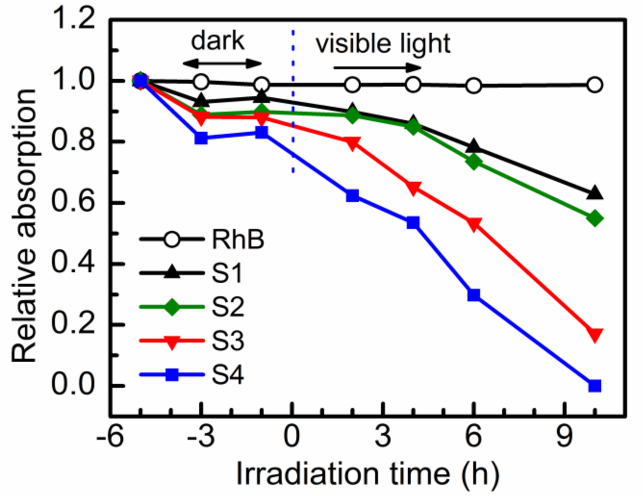

Figure 5.10 The repeated photocatalytic degradation of RhB for the recollected *m*-BiVO$_4$ octahedral crystals after the first test.

5.5 Concluding remarks

In summary, mono-dispersed *m*-$BiVO_4$ octahedral single crystals have been synthesized by a simple hydrothermal method with the assistance of SDBS. These single crystals showed uniform sizes and preferred {120} and {021} crystalline facets with good degree of crystallization. The formation and growth of the octahedral shape was considered to be a typical supersaturation process combined with Ostwald ripening process. The crystal size of *m*-$BiVO_4$ octahedra could be facially adjusted in a broad range from 5 μm to less than 200 nm. Moreover, these octahedral single crystals showed superior high photocatalytic performance in the degradation of RhB under visible light irradiation. The successful synthesis of *m*-$BiVO_4$ octahedra with preferred facets validated the further investigation of the different facet effects on the photocatalytic performance, and also led to an alternative strategy for the facet-engineering towards chemical, biomedical and environmental applications.

Chapter 6. *m*-$BiVO_4$@γ-Bi_2O_3 Composite with Core-Shell Heterogeneous Structure

6.1 Introduction

Although mono-dispersed *m*-$BiVO_4$ octahedral single crystals have been successfully synthesized, and they exhibit superior high photocatalytic performance in the degradation of RhB under visible light irradiation, their photocatalytic activity is not ideal for practical application yet, and the efficiency is still low as compared to TiO_2 (under UV light). One of the main reasons is the rapid recombination of photogenerated electrons and holes in *m*-$BiVO_4$, because of the limited migration of photogenerated electrons and holes.

As reviewed in Section 2.3.4, composite semiconductors can reduce the recombination rate of photogenerated electrons and holes and thus have been widely employed for improved photocatalytic efficiency. Among various the composite structures, the formation of a p-n heterojunction has been considered as the most efficient way to separate the generated electron-hole pairs. This is mainly because of the inherent establishment of internal electric field directed from the n-type to p-type semiconductor [90,126]. Recently, many efforts for photocatalytic performance enhancement through p-n composite fabrication have been attempted, such as $Co_3O_4/BiVO_4$, $CuO/BiVO_4$, $Bi_2O_3/BiVO_4$, etc. [90,126-128]. To a certain extent, they can enhance the separation of electron-hole pairs and improve the photocatalytic performance of $BiVO_4$. However, Co and Cu are transition elements with variable valences and low chemical stability, and are not suitable for recyclable photocatalysis.

In addition, due to the much narrower band gap of some p-type oxides than that of $BiVO_4$ (1.20 for CuO and 2.40 for *m*-$BiVO_4$), the resultant composite materials would exhibit a much lower redox capability in photocatalytic application. Alternatively, as a main group element, Bi has a much more stable cation valence, and its chemical property is closer to $BiVO_4$ than other p-type oxides. Furthermore, the conduction band edge and valence band edge of Bi_2O_3 are close to those of $BiVO_4$. Therefore, photoinduced electrons in Bi_2O_3 would easily transfer to $BiVO_4$ under the inducement action of the internal p-n electric field, leaving holes in the Bi_2O_3 valence band. In such a way, the photoinduced electrons and holes could be effectively separated, thus further improve the photocatalytic activity of materials.

Recently, intrinsic p-type semiconductor bismuth oxide (Bi_2O_3) has attracted much attention because of their extensive applications in solid oxide fuel cells, gas sensors and catalysts [129]. Bi_2O_3 has several polymorphs, such as α–, β–, γ-and δ-phase [130]. And among them, γ-Bi_2O_3 has been reported as the best photocatalyst mainly due to its unique valence band structure [131-133]. However, because of the meta-stable nature of γ-Bi_2O_3, synthesis and study of this crystal phase has seldom been reported. In this chapter, we proposed a novel "etching" method to fabricate γ-Bi_2O_3 on the surface of *m*-$BiVO_4$ to form the *m*-$BiVO_4$@γ-Bi_2O_3 core-shell hetero-structure. Moreover, by controlling the "etching" condition and duration, *m*-$BiVO_4$@γ-Bi_2O_3 composite with various ratios can be prepared. We also demonstrated that by combining the two excellent photocatalytic materials together, the visible-light photocatalytic performance in RhB degradation can be greatly improved.

6.2 Synthesis of m-$BiVO_4$@γ-Bi_2O_3 composite

The synthesis procedure is given in the flow chart in Figure 6.1. In this part, the as-prepared *m*-$BiVO_4$ octahedral single crystals with size around 1-2 μm were used (for ease of characterization). 0.2 g as-prepared *m*-$BiVO_4$ crystals were dispersed in 40 ml NaOH solution followed by ultrasonic treatment. The NaOH solution, 0.1 ~ 0.3 M, was prepared by adding certain amount of NaOH powder into de-ionized (DI) water under vigorous stirring. The mixed solution was then transferred into an autoclave, heated at 130 °C for 3 ~ 10 h, and cooled down naturally to room temperature. The final yellow orange solid products obtained were collected and washed for further characterization and testing. The amount of alkaline reagent and reaction duration were used to control the phase ratio between γ-Bi_2O_3 and *m*-$BiVO_4$ in the final product. 5 typical samples synthesized are listed in Table 6.1. The phase ratios (in percentage) of *m*-$BiVO_4$@γ-Bi_2O_3 composite samples were calculated based on the Rietveld analysis of the corresponding XRD patterns. For simplification, the samples with increasing γ-Bi_2O_3 content were named as BB01 to BB05 in the subsequent test and discussion.

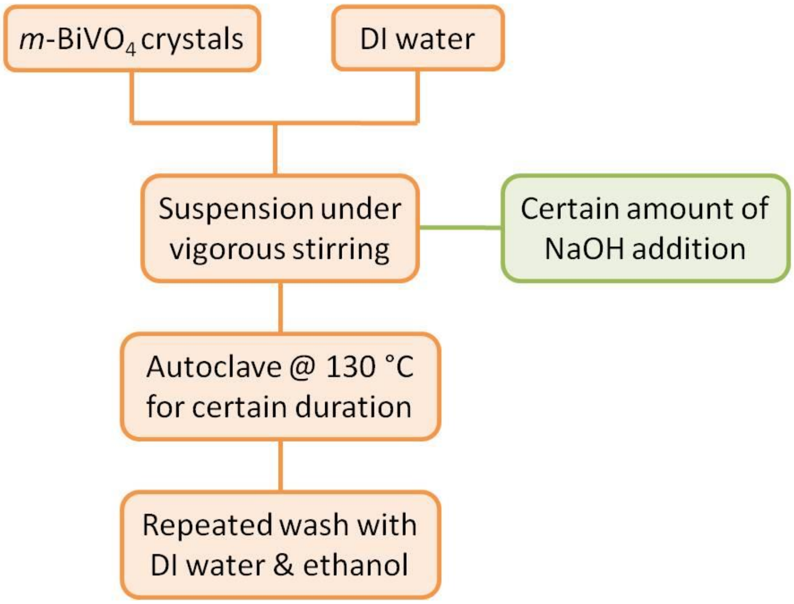

Figure 6.1 Synthesis procedure of *m*-$BiVO_4$@γ-Bi_2O_3 composites.

Table 6.1 List of sample name, composition, and orthogonal experiment details of the as-prepared *m*-$BiVO_4$@γ-Bi_2O_3 composite samples.

Sample Name	Composition (Calculated through XRD Rietveld Analysis)	Reaction Duration (h)	NaOH Concentration (M)
BB01	95% *m*-$BiVO_4$/5% γ-Bi_2O_3	6	0.1
BB02	86% *m*-$BiVO_4$/14% γ-Bi_2O_3	3	0.2
BB03	66% *m*-$BiVO_4$/34% γ-Bi_2O_3	6	0.2
BB04	25% *m*-$BiVO_4$/75% γ-Bi_2O_3	6	0.3
BB05	1% *m*-$BiVO_4$/99% γ-Bi_2O_3	10	0.2

6.3 Crystal phase of m-$BiVO_4$@γ-Bi_2O_3 composite

The crystal structure of the *m*-$BiVO_4$@γ-Bi_2O_3 composite samples was studied by the XRD analysis as shown in Figure 6.2. It can be seen that all five samples were composed of scheelite monoclinic $BiVO_4$ (JCPDC No. 14-0688) and γ-Bi_2O_3 (JCPDC No. 45-1344). In addition, by increasing the reaction duration from 3 hours to 10 hours (Sample BB02, BB03 and BB05), the amount of *m*-$BiVO_4$ phase was reduced and more γ-Bi_2O_3 phase was formed. Especially for sample BB05, only trace amount of *m*-$BiVO_4$ could be detected in the XRD pattern, and it has become γ-Bi_2O_3 dominant. It was evident that given longer reaction time, more *m*-$BiVO_4$ crystals could change into γ-Bi_2O_3 phase. Meanwhile, alkaline concentration was found to accelerate the formation of γ-Bi_2O_3 phase. As the alkaline increased from 0.1 M to 0.3 M, less *m*-$BiVO_4$ phase can be found in the resultant powders, as indicated by samples BB01, BB03 and BB04. Base on the XRD analysis, it was concluded that both alkaline amount and reaction duration are favorable for the formation of γ-Bi_2O_3 from *m*-$BiVO_4$ in this hydrothermal synthesis method.

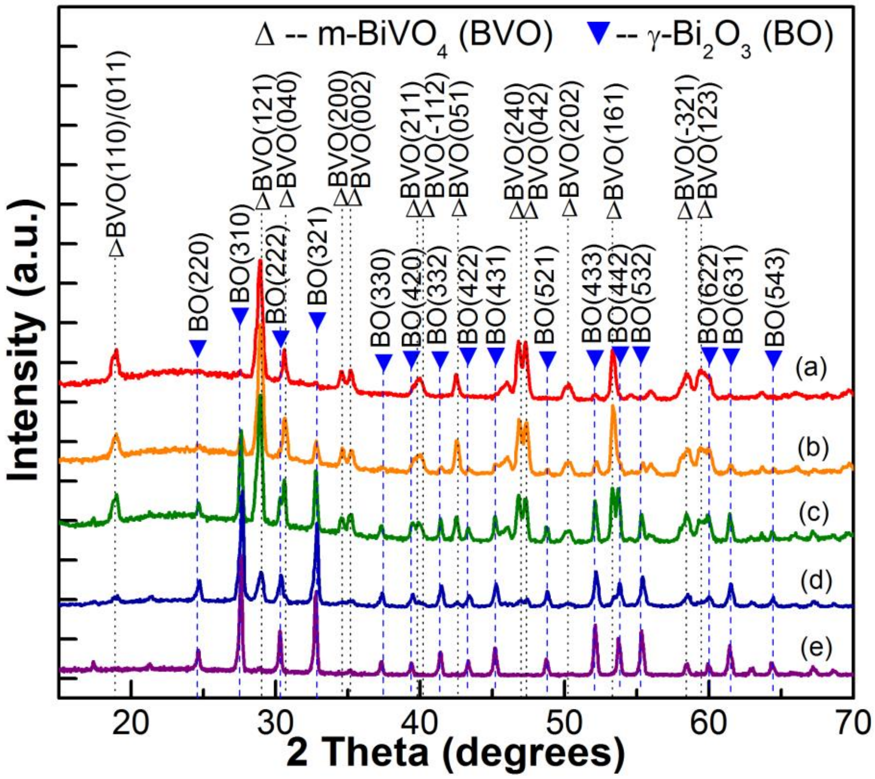

Figure 6.2 XRD patterns of the as-prepared samples. (a) BB01 (0.1 M/6 h), (b) BB02 (0.2 M/3 h), (c) BB03 (0.2 M/6 h), (d) BB04 (0.3 M/6 h), and (e) BB05 (0.2 M/10 h).

6.4 Morphology of m-$BiVO_4$@γ-Bi_2O_3 composite

The SEM images in Figure 6.3 show the morphology change of the *m*-$BiVO_4$@γ-Bi_2O_3 composite particles with different reaction durations. Apparently, for BB02 and BB03, the surface of the composite particles became rough and corroded when compared with that of the pure *m*-$BiVO_4$ octahedral crystals. As the reaction time increased, the surface corrosion went deeper, although the particles still remained in octahedral shape. Sample BB05 was an exception. After long-time reaction (10 hours), γ-Bi_2O_3 phase has become dominant in BB05 and the crystals have grown into a tetrahedron based shape with much larger crystal size up to ~5 μm. This indicates an intensive crystal growth and ripening process at the final stage of the synthesis reaction.

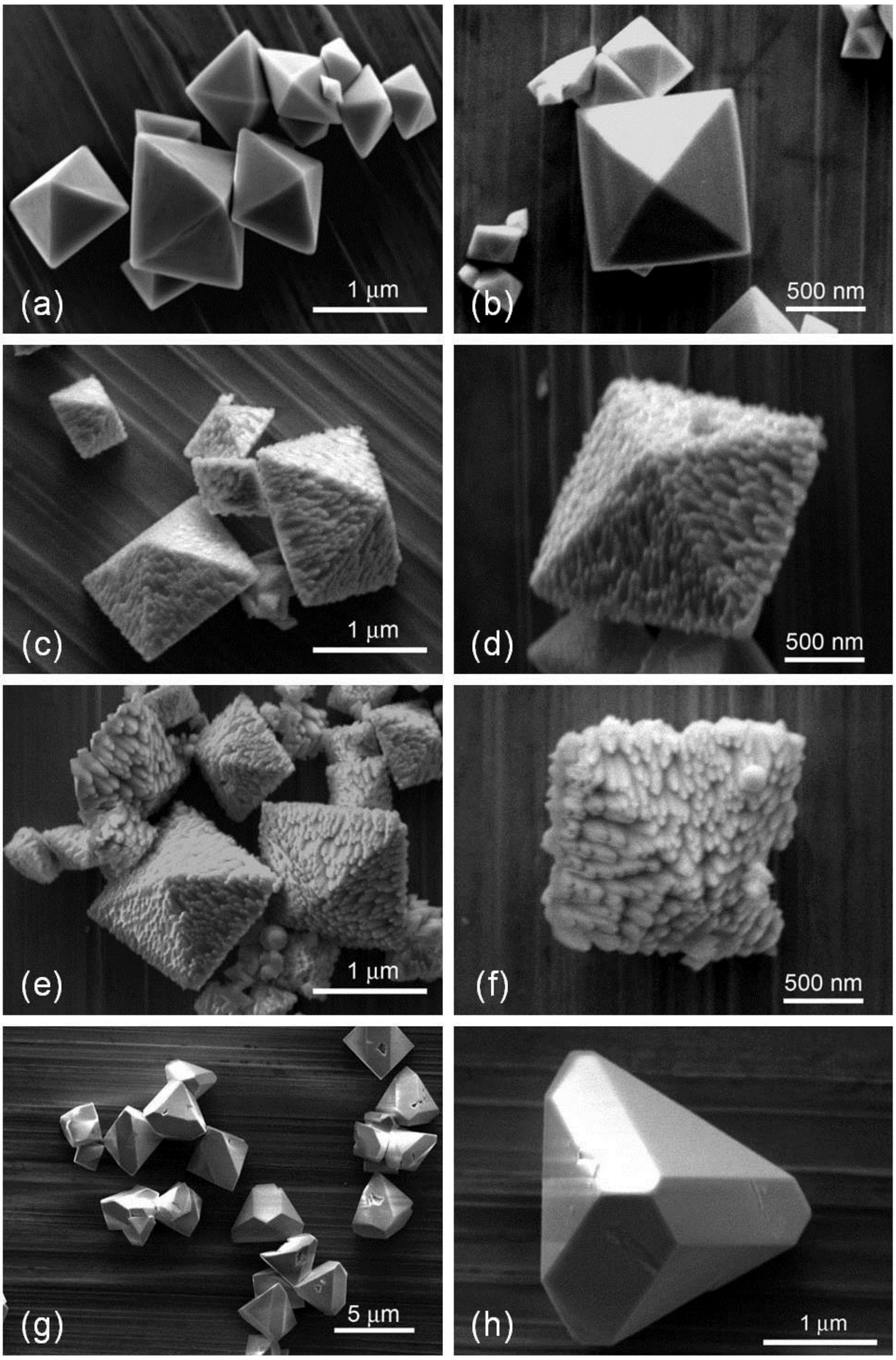

Figure 6.3 SEM images of as-prepared m-BiVO$_4$@γ-Bi$_2$O$_3$ composite particles with different reaction durations, (a) & (b) 0 h pure m-BiVO$_4$, (c) & (d) 3 h BB02, (e) & (f) 6 h BB03, (g) & (h) 10 h BB05.

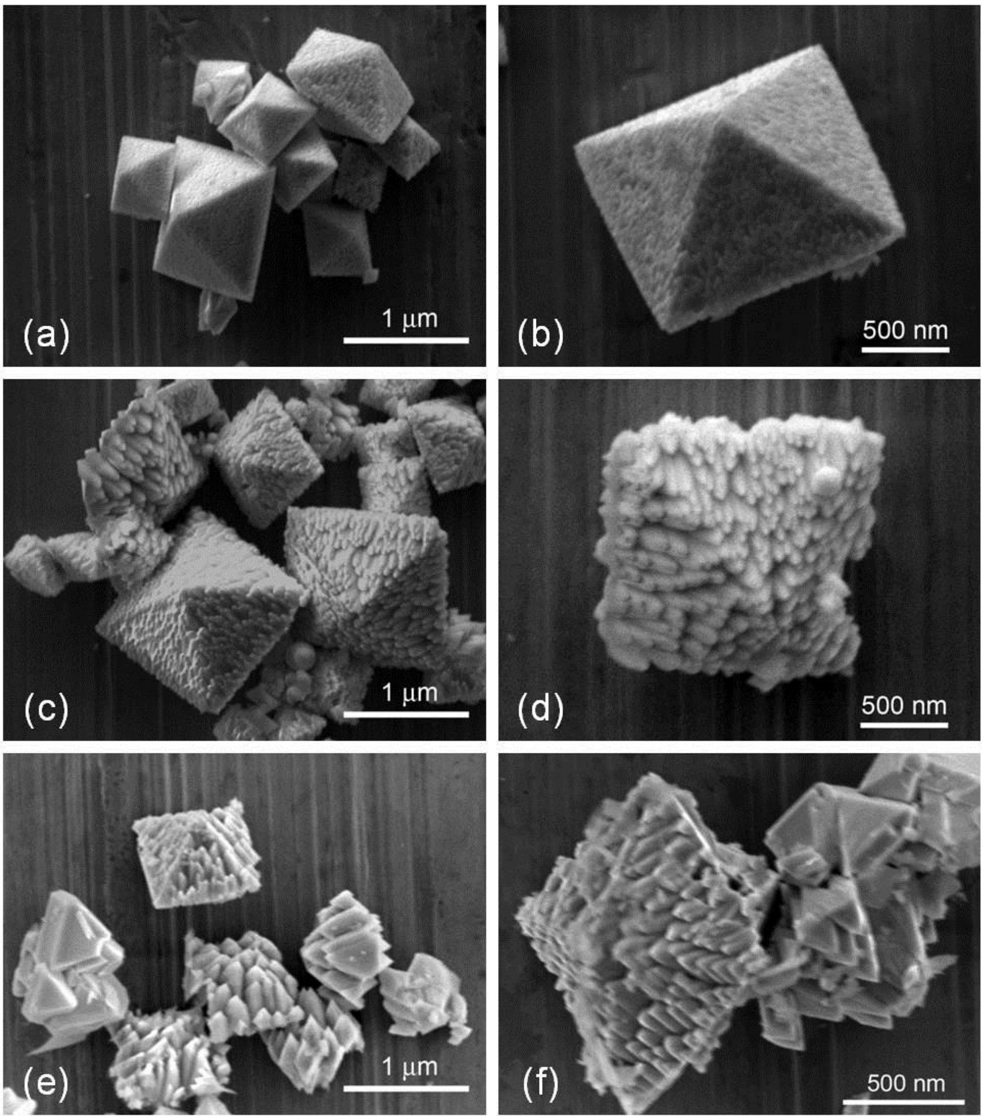

Figure 6.4 SEM images of as-prepared *m*-$BiVO_4$@γ-Bi_2O_3 composite particles fabricated under different alkaline concentrations, (a) & (b) 0.1 M BB01, (c) & (d) 0.2 M BB03, (e) & (f) 0.3 M BB04.

The SEM images of the *m*-$BiVO_4$@γ-Bi_2O_3 composite particles prepared under different alkaline concentration are compared in Figure 6.4, where different degrees of corrosion on crystal surface could be obviously observed. Despite slight roughness, crystals in sample BB01 still exhibited complete octahedra and sharp edges, which were least different from pure *m*-$BiVO_4$ crystals. By increasing the alkaline concentration, BB03 and BB04 resulted in deeper corroded surface and destruction tendency of octahedral shape. Especially, some of the crystals in BB04 have been deeply corroded and the sharp corner parts start to peel-off or crack. These cracked pieces are supposed to grow rapidly along certain directions during the ripening process, and finally evolve into large polyhedrons, as shown in Figure 6.3 (g) and (h) for BB05.

Figures 6.3 and 6.4 together clearly illustrate the surface corrosion and morphology evolution of the *m*-$BiVO_4$@γ-Bi_2O_3 composite particles. Importantly, the degree of surface corrosion was found corresponding to the content of γ-Bi_2O_3 phase. For example, BB01 with least surface corrosion corresponds to the least amount of γ-Bi_2O_3 phase among 5 composite samples. This correlation strongly indicated the surface "etching" mechanism in the formation of *m*-$BiVO_4$@γ-Bi_2O_3 composite.

The crystal structure of *m*-$BiVO_4$@γ-Bi_2O_3 composite was further investigated by TEM-SAED observation. Figure 6.5 (a) indicates the rough particle surface in BB03, as compared to the smooth octahedron in pure *m*-$BiVO_4$, Figure 6.5 (c). The morphology change was consistent with the SEM observations. More importantly, the SAED pattern in Figure 6.5 (b) clearly implies a composite structure composed of both *m*-$BiVO_4$ and γ-Bi_2O_3 crystal phases. In detail, some additional diffraction spots could be found and indexed to single crystal phase of γ-Bi_2O_3. In comparison, the diffraction pattern of pure *m*-$BiVO_4$ is given in Figure 6.5 (d).

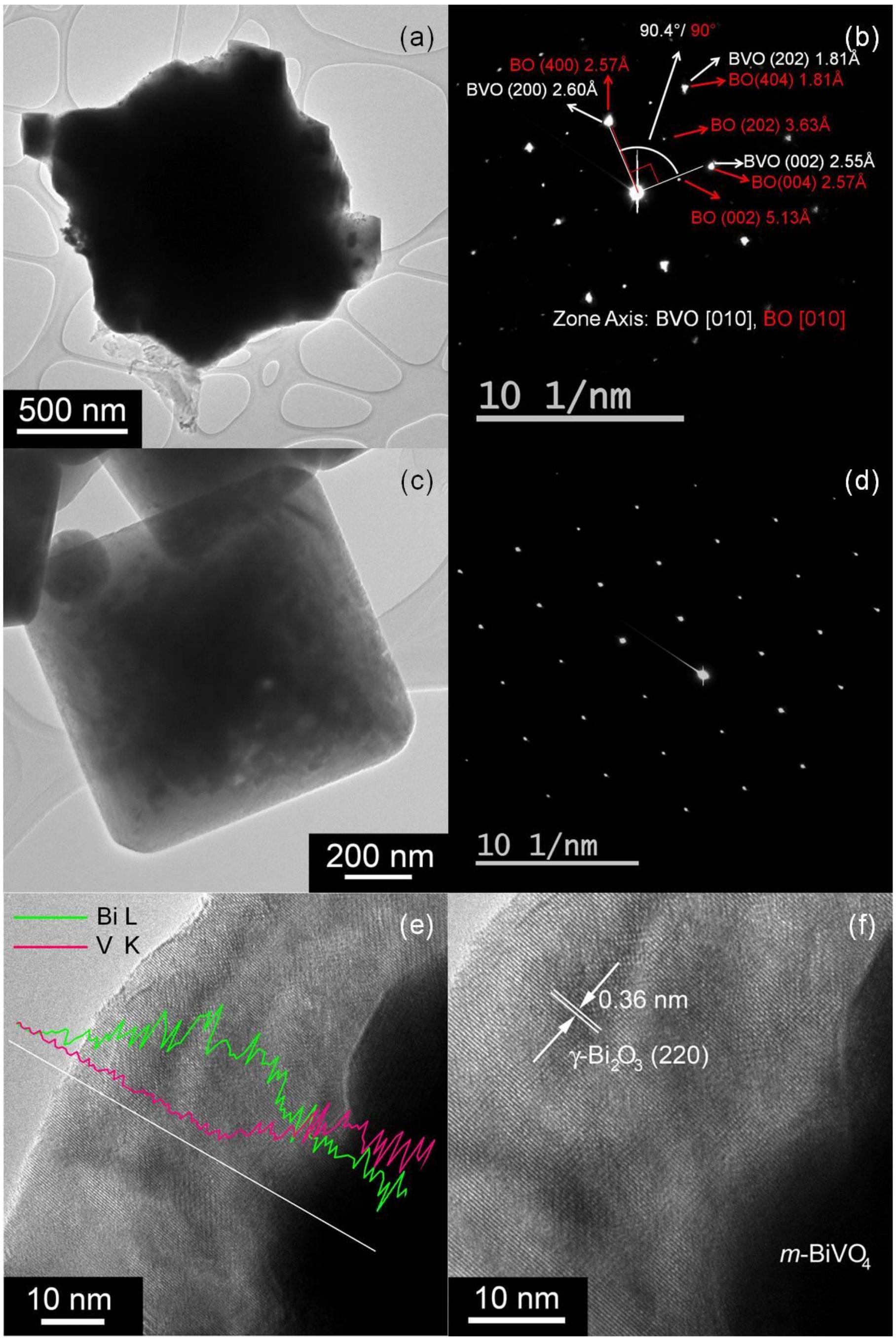

Figure 6.5 (a) TEM image, (b) the corresponding SAED pattern, (e) EDX-line scan and (f) HR-TEM image of *m*-$BiVO_4$@γ-Bi_2O_3 composite BB03, with (c) TEM image and (d) its corresponding SAED pattern of a pure *m*-$BiVO_4$ octahedral single crystal as comparison.

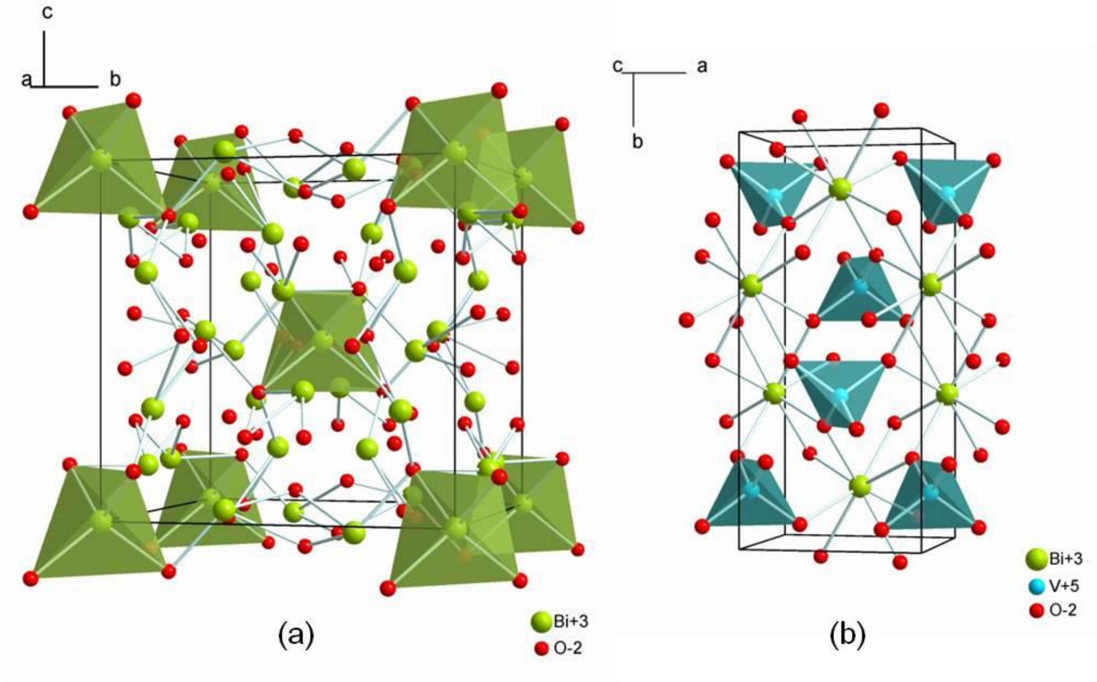

Figure 6.6 Crystal structure comparison between (a) cubic γ-Bi_2O_3 and (b) monoclinic scheelite $BiVO_4$.

It was also noticed that some diffraction spots of γ-Bi_2O_3, such as (400) and (004), overlapped with or were very close to the *m*-$BiVO_4$ phase, (200) and (002), respectively. This could be explained by the relationship of the two crystal structures with certain alignment. Figures 6.6 (a) and (b) represent the structure illustrations of the two crystal phases. The lattice parameter of γ-Bi_2O_3 is 10.267 Å, which is nearly twice of *a* and *c* values of *m*-$BiVO_4$ phase, 5.195 Å and 5.092 Å, respectively. In addition, β of *m*-$BiVO_4$ is 90.4°, which is only a slight deviation from the right angle. As a result, $d_{(200)}$ = 2.598 Å and $d_{(002)}$ = 2.546 Å for *m*-$BiVO_4$ are very close to $d_{(400)}$ = 2.567 Å for γ-Bi_2O_3. Thus, the diffraction pattern in Figure 6.5 (b) not only represents a composite structure, but also indicates the locally crystal alignment or epitaxial relationship of the latter grown γ-Bi_2O_3 on the *m*-$BiVO_4$ crystals. The orientation relationship could be given as follows: [010] γ-Bi_2O_3 || [010] *m*-$BiVO_4$, approximately [100] γ-Bi_2O_3 || [100] *m*-$BiVO_4$, and approximately [001] γ-Bi_2O_3 || [001] *m*-$BiVO_4$. In addition, the lattice mismatch of γ-Bi_2O_3 from *m*-$BiVO_4$ in *a* and *c* directions, about 1.25% and 0.75%, respectively, were found to be the least among those of other Bi_2O_3 polymorphs, as listed in Table 6.2. Such small lattice mismatch, as well as the hydrothermal synthesis conditions, is considered to be some probable reasons for the successful formation of γ-Bi_2O_3 rather than other crystal phases.

Table 6.2 Comparison of crystal structure and lattice mismatch from *m*-$BiVO_4$ of various Bi_2O_3 polymorphs.

Polymorph	Crystal Structure (Space group)	Crystal Parameters (Å / °)	Lattice-mismatch From *m*-$BiVO_4$ at *a* & *c* directions	Reference PDF Card Number
γ-Bi_2O_3	Cubic (197)	*a*: 10.26	2*a*: –1.25% 2*c*: +0.75%	45-1344
α-Bi_2O_3	Monoclinic (14)	*a*: 5.849 *b*: 8.169 *c*: 7.512 *β*: 112.98	*a*: +12.6% *c*: +47.5%	41-1449
β-Bi_2O_3	Tetragonal (114)	*a*: 7.742 *c*: 5.631	*a*: +49.0% *c*: +52.0% 1.5a: –0.65% 1.5c: +1.36%	27-0050
δ-Bi_2O_3	Cubic (224)	*a*: 5.525	*a*: +6.35% *c*: +8.50%	27-0052

Figure 6.5 (e) represents the STEM-EDX line scan result of the *m*-$BiVO_4$@γ-Bi_2O_3 composite at the surface region. It clearly shows that the γ-Bi_2O_3 phase is located at the surface, while the inside dark area of image corresponds to the thick *m*-$BiVO_4$ octahedral crystals. Such core-shell structure could be further confirmed by the HRTEM observation as shown in Figure 6.5 (f). The lattice distance of the outer crystal about 0.36 nm is consistent with the *d*-spacing of γ-Bi_2O_3 (202) plane (and cannot be indexed with any *d*-spacing values for *m*-$BiVO_4$ phase).

Based on the above analysis and discussion, the formation mechanism of γ-Bi_2O_3 on the surface of *m*-$BiVO_4$ crystals could be elaborated as follows: Firstly, VO_4^- is quite soluble in alkaline solution, while Bi^{3+} ions are not. Although *m*-$BiVO_4$ is quite chemically stable in aqueous solution at room temperature under open system, the dissolving of VO_4^- ions can be significant in strong alkaline solution in the high temperature and high pressure conditions in an autoclave. This can be considered as an "etching" reaction. With the surface part of a $BiVO_4$ crystal losing VO_4^- ions, Bi^{3+} ions can only precipitate as γ-Bi_2O_3 phase and re-construct as the outer shell. Hence, the single phase *m*-$BiVO_4$ crystals can transfer into *m*-$BiVO_4$@γ-Bi_2O_3 core-shell structure to form the p-n hetero structure. Further, as the reaction duration increased, more VO_4^- ions dissolved in the alkaline solution, and more *m*-$BiVO_4$ phase would gradually decompose into γ-Bi_2O_3 crystals. The decomposition of *m*-$BiVO_4$ happened at the surface and progressed deep into the crystals. At the same time, the latter γ-Bi_2O_3 formation exhibited a fast crystal growth and ripening. Such fast growth of Bi_2O_3 has been widely reported elsewhere [134-137]. Therefore, the final product after 10 hour reaction has resulted in much larger γ-Bi_2O_3 crystals, as indicated in Figure 6.3 (g) and (h). The overall synthesis route of γ-Bi_2O_3 from *m*-$BiVO_4$ crystals can be summarized in Equation 6-1 as below:

$$2\ m\text{-}BiVO_4 \downarrow + 2\ OH^- \rightarrow \gamma\text{-}Bi_2O_3 \downarrow + 2\ VO_4^- + H_2O \qquad (6\text{-}1)$$

The surface morphology transformation and core-shell heterostructure formation could be schematically illustrated in Figure 6.7.

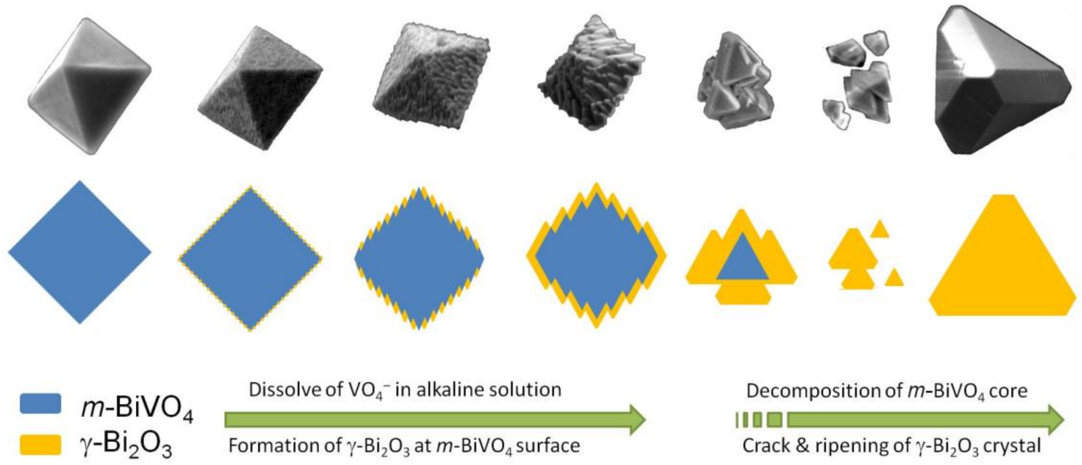

Figure 6.7 Schematic illustration of the surface reaction mechanism and morphology evolution of *m*-$BiVO_4$@γ-Bi_2O_3 core-shell heterostructure.

6.5 Photo-absorption of *m*-$BiVO_4$@γ-Bi_2O_3 composite

The color of pure *m*-$BiVO_4$ octahedral crystals is vivid yellow. After the “etching” reaction to form *m*-$BiVO_4$@γ-Bi_2O_3 composite, the color changes to yellow-orange.

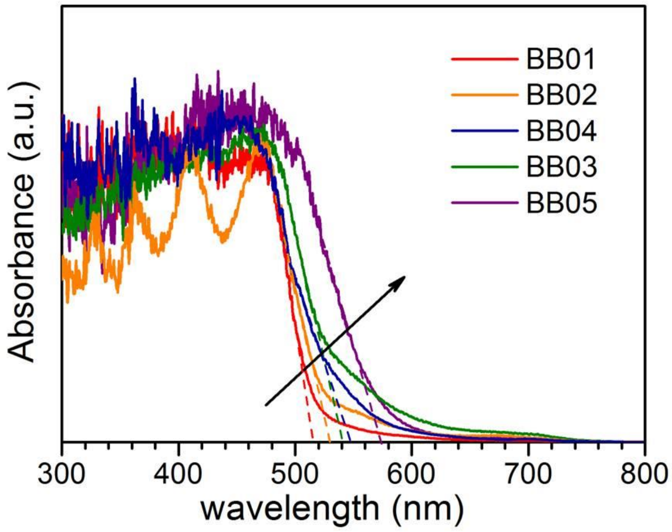

Figure 6.8 UV-Vis diffused reflectance spectra of the as-prepared *m*-$BiVO_4$@γ-Bi_2O_3 composite samples.

Figure 6.8 shows the UV–Vis diffused reflectance spectra of these five as-synthesized *m*-$BiVO_4$@γ-Bi_2O_3 composite samples, respectively. The optical absorptions of BB01 start at around 520 nm, and as the amount of γ-Bi_2O_3 shell phase increases, the beginning of absorption can be extended to around 580 nm for BB05. Therefore, the visible-light absorption range of *m*-$BiVO_4$ octahedral crystals can be enlarged by the coupling of p-type γ-Bi_2O_3.

The photocatalytic performance of the five as-prepared composite samples, as well as the pure *m*-$BiVO_4$ octahedral crystals, were evaluated by the photodegradation of RhB under visible light irradiation and shown in Figure 6.9. The overall degradation efficiencies (after 10 hours irradiation) of each sample were calculated and listed in Table 6.3. It can be clearly seen that the photocatalytic performance of sample BB01, BB02 and BB03 has been greatly enhanced, as compared with that of pure *m*-$BiVO_4$ sample. Typically, BB03 shows the best performance with fastest degradation rate among these samples, with 31% improvement, as compared to that of the pure *m*-$BiVO_4$ octahedral crystals. The enhancement mechanism involved by heterojunction structure is elaborated in the Section 6.6.

It was also noticed that sample BB04 and BB05 exhibit lower photocatalytic activity than pure *m*-$BiVO_4$ despite their composite heterostructure. Thus, besides the p-n heterojunction formation induced prohibited electron-hole pair recombination, other factors should also be involved to determine the final photocatalytic performance of these *m*-$BiVO_4$@γ-Bi_2O_3 composites. Based on our experiments and analysis, possible factors are proposed as follows:

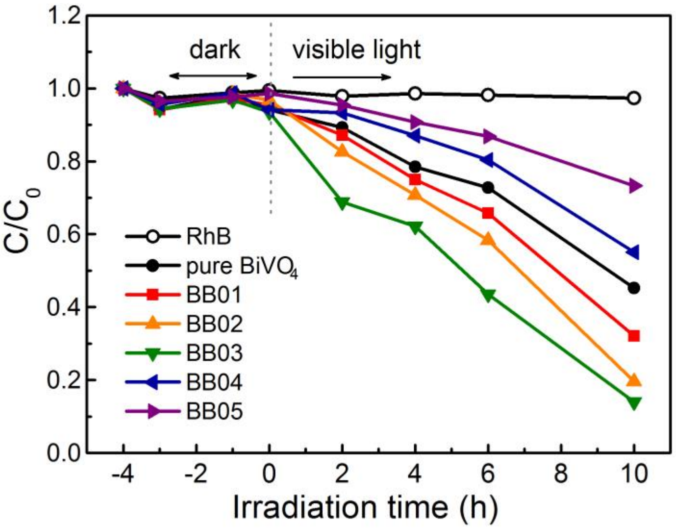

Figure 6.9 Photocatalytic degradation of RhB for the as-prepared *m*-BiVO$_4$@γ-Bi$_2$O$_3$ composite samples.

Firstly, by forming γ-Bi$_2$O$_3$ phase on *m*-BiVO$_4$ octahedral crystals, the specific surface area of the powder samples was influenced. A high specific surface area can cater for a high photocatalytic performance. As illustrated in Section 6.4, the synthesis of γ-Bi$_2$O$_3$ phase could be considered as an "etch" process of *m*-BiVO$_4$ octahedral crystals. At early stage, the dissolution of V ions not only leaves γ-Bi$_2$O$_3$ phase, but also results in a rough surface. The specific surface area values of these samples were investigated through BET method, and the results are listed in Table 6.3. It is clearly indicated that as the "etching" reaction at early stage goes further, rougher surface with larger specific surface area could be achieved. BB03 possessed the largest value, around 3.17 m^2/g. However, at the later stage, the dissolving of V ion from inside crystals could not influence much on surface morphology. Meanwhile, the increase of γ-Bi$_2$O$_3$ phase also combines with fast crystal growth and rapid ripening. Especially sample BB05 is composed of smooth crystals with much larger particle size. Thus, crystal surface area drops greatly, and sample BB04 and BB05 exhibit a decreasing trend in specific surface area.

Table 6.3 Degradation efficiencies of RhB after 10 hours and specific surface area of the as-prepared *m*-$BiVO_4$@γ-Bi_2O_3 composite samples.

Sample Name	Degradation Efficiency of RhB ($1-C_{10}/C_0$)	Specific Surface Area (m^2/g)
Pure $BiVO_4$	55%	1.50
BB01	68%	2.24
BB02	80%	2.54
BB03	86%	3.17
BB04	45%	1.75
BB05	27%	0.52

Secondly, despite the formation of p-n heterojunction, whether photocatalytic performance can be improved or not also relies on the thickness of γ-Bi_2O_3 outer shell. Too thin a layer, such as in BB01, cannot induce sufficient electrons or holes although their recombination could be inhibited. On the contrary, if the shell material is too thick, like in BB04 & BB05, the light that arrived at the space charge layer can be attenuated dramatically, and the recombination cannot be suppressed efficiently since the γ-Bi_2O_3 layer is much thicker than the space charge layer. Similar results that the thickness of shell material can significantly affect the electron transfer ability of the heterojunction have also been reported for TiO_2-based core-shell materials [138,139]. In this work, although it was practically difficult to estimate the exact thickness of γ-Bi_2O_3 layer in each sample, an increasing shell thickness upon higher γ-Bi_2O_3 contents was quite reasonable according to the "etching" reaction mechanism, and could be evidenced by the crystal morphology evolution. Among five heterostructured samples, BB03 may possess an optimal shell thickness that contributes much to its best photocatalytic performance.

In short, although p-n heterostructure is an effective method to suppress the recombination of photogenerated electron-hole pairs, the formation of the heterojunction may also involve other issues that influence the final photocatalytic performance. In this study, both specific surface area and shell thickness are considered as important contributing factors, which could be a useful guideline in the design and development of heterostructured photocatalytic materials.

Finally, the recyclability of the best two samples, BB02 and BB03, was examined by repeated photodegradation test. Their chemical stability was studied by crystal phase characterization after photodegradation reaction. Figures 6.10 (a) and (b) clearly indicate that there was no phase change in the two samples before and after photocatalytic test. Meanwhile, the degradation efficiency was maintained during the repeated photodegradation test, as shown in Figure 6.11. Thus, the good chemical and photocatalytic stabilities of these composite particles can be concluded.

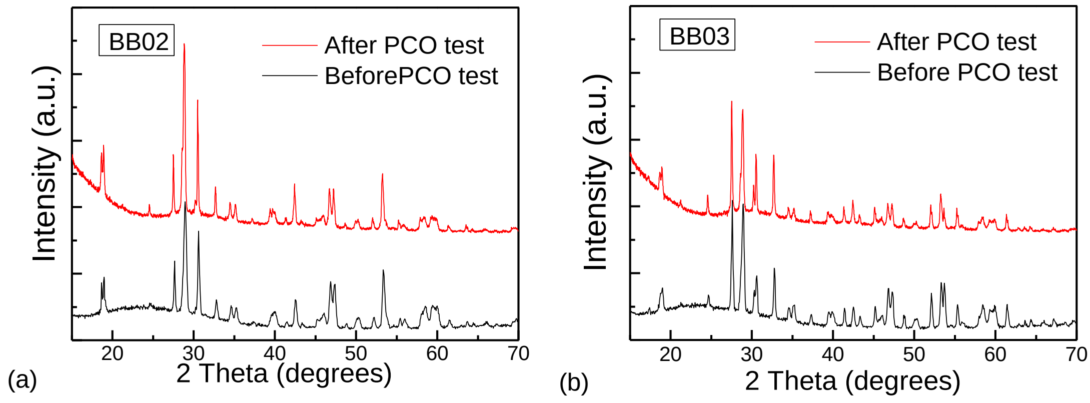

Figure 6.10 XRD patterns of the samples (a) BB02 and (b) BB03 before (lower black) and after (upper red) photocatalytic test in the degradation of RhB.

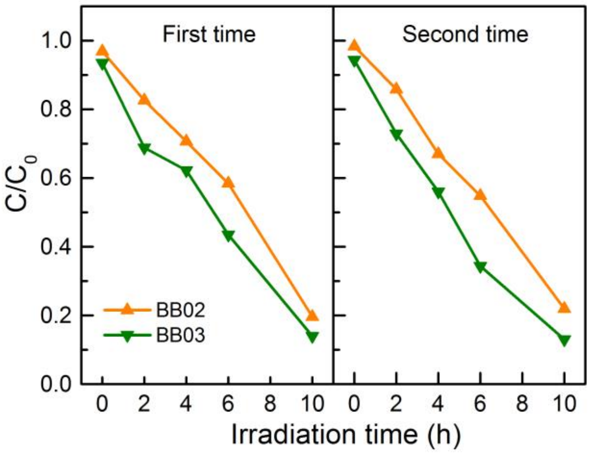

Figure 6.11 the repeated photocatalytic test of the samples BB02 and BB03 in the degradation of RhB.

6.6 Mechanism of enhanced charge carrier transfer

In our experiment, Bi_2O_3 phase was formed on the surface of *m*-$BiVO_4$ during the *m*-$BiVO_4$ phase decomposition. As we know, Bi_2O_3 is a p-type semiconductor, and *m*-$BiVO_4$ is determined as an n-type material. Therefore, at the interface region, p-n heterojunction would be formed. Compared to single-phase photocatalysts, hybrid-semiconductor systems possess significant advantages in promoting the separation of electron-hole pairs and keeping reduction and oxidation reactions at two different reaction sites. Among different constructions of heterostructure, p-n junction was the mostly efficient way to enhance the charge carrier transfer. This is one of the most announced mechanisms for the great photocatalytic improvement in our *m*-$BiVO_4$@γ-Bi_2O_3 composite samples, which could be illustrated as follows:

Before the contact of the two materials, the band edge positions of their conduction band (CB) and valence band (VB) at the point of zero charge (pH_{zpc}) can be predicted by the empirical equation:

$$E_{CB}^{0} = X - E^{c} - 1/2\ E_{g} \qquad (6\text{-}2)$$

where E_{CB}^{0} is the CB edge potential; X is the absolute electronegativity of the semiconductor, which is the geometric mean of the absolute electronegativity of the constituent atoms (X values for $BiVO_4$ and Bi_2O_3 are 6.04 [99] and 5.95 eV [106], respectively); E^c is the energy of free electrons on the hydrogen scale (about 4.5 eV); and Eg is the band gap of the semiconductor. The predicted band edge positions of Bi_2O_3 and $BiVO_4$ by the above equation are shown in Table 6.4, and illustrated in Figure 6.12 (a).

When the p-n junction between Bi_2O_3 and $BiVO_4$ is formed and thermodynamic equilibrium is reached, an inner electrical field can be established with a direction from n-type semiconductor to p-type semiconductor. Meanwhile, the energy bands of Bi_2O_3 shift upward while those of the $BiVO_4$ shift downward until the Fermi levels of both semiconductors join at a same level. According to this band edge position, the photogenerated electrons on the conduction band of the p-type semiconductor are transferred to that of the n-type one, and simultaneous holes on the valence band of n-type material can move to that of p-type one under the potential of the band energy difference. In addition, the migration of photogenerated carriers can be promoted by the internal field near the p-n junction. Therefore, the recombination of electron-hole pairs can be significantly suppressed, and the photocatalytic reaction can be greatly enhanced. This can be schematically illustrated in Figure 6.12 (b).

Table 6.4 Absolute electronegativity, estimated band gap, calculated energy levels of conduction band edge and valence band edge at the zero-charge point for *m*-$BiVO_4$ and γ-Bi_2O_3.

Oxide Material	X, Absolute Electronegativity	Estimated Band Gap (eV)	Calculated CB (eV)	Calculated VB (eV)
$BiVO_4$	6.04	2.26	0.41	2.67
Bi_2O_3	5.95	2.04	0.43	2.47

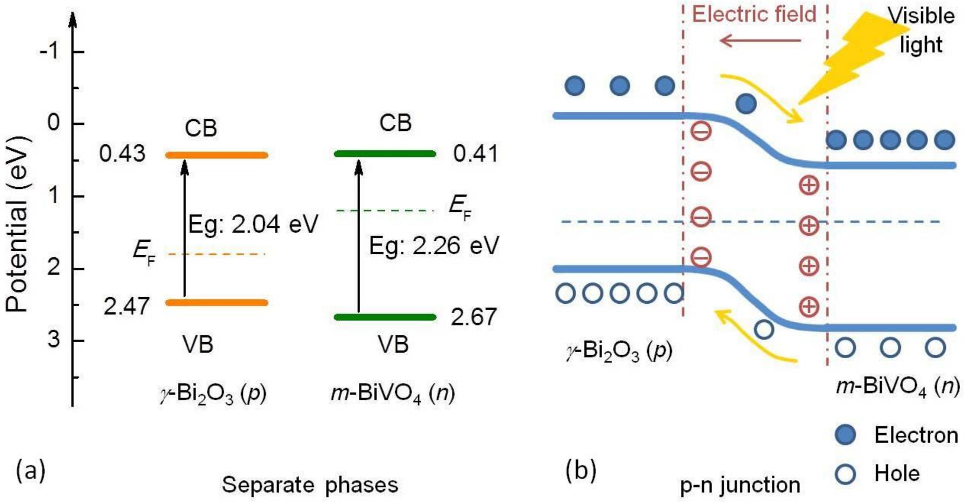

Figure 6.12 Schematic illustrations of the energy band structures (a) for separate phases and (b) after the formation of *m*-BiVO$_4$@γ-Bi$_2$O$_3$ p-n hetero junction.

Furthermore, the enhanced charge carrier transfer by p-n heterostructure can also be evidenced by the surface photovoltage (SPV) spectra. Figure 6.13 shows the transient light-on/light-off SPV response of pure *m*-BiVO$_4$ crystals (a) and BB03 powders (b), respectively, under the irradiation of LED light with the wavelength of 455 nm. When the working current was higher than 50 mA, the light-on SPV values of both samples exceeded 200 mV, which indicated their excellent photocatalytic performance. The averaged light-on SPV of the two samples are compared in Figure 6.13 (c), which clearly shows the saturation trends of light-on SPV under the increasing working current for the two samples. Specifically, the SPV of pure *m*-BiVO$_4$ crystals saturated at around 220 mV; while BB03 exhibited a distinctly higher SPV level higher than 300 mV. According to the surface photovoltage spectroscopy technique, a high SPV response corresponds to the more efficient charge carrier separation and transfer [140]. Therefore, the higher SPV response of BB03 indicated that the introduction of p-n heterojunction structure is beneficial to the separation of the photogenerated electron-hole pairs in $BiVO_4$ and eventually improve the photocatalytic performance.

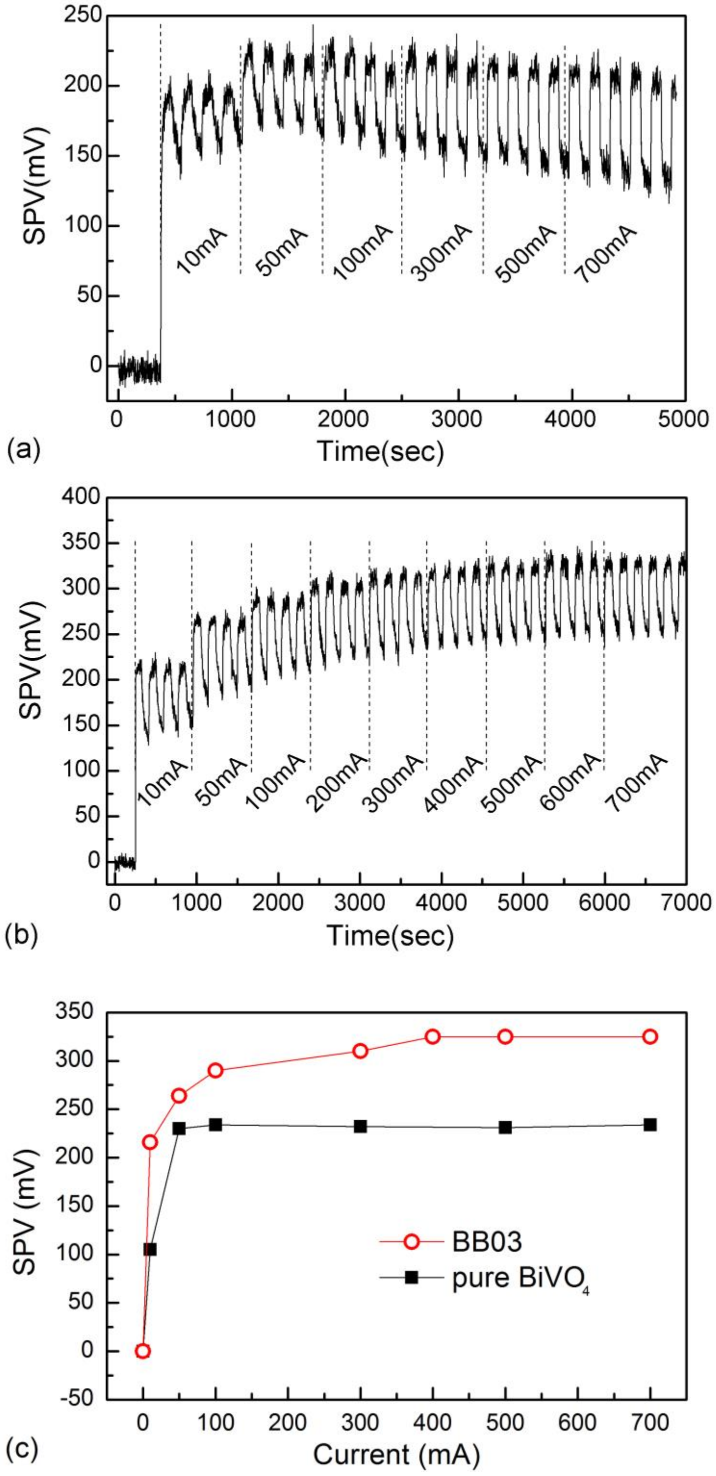

Figure 6.13 Transient SPV spectra of (a) pure *m*-$BiVO_4$ and (b) BB03, and (c) the comparison of average SPV values under different working current.

Finally, the recombination property of these two samples was also investigated based on the light-off transient response in SPV spectra, as indicated in Figure 6.14 (a) and (b). It can be seen that the recombination rate of BB03 was slightly lower than that of pure *m*-$BiVO_4$. This could also be ascribed to the p-n heterojunction structure where the electron-hole pairs are separated onto different material surfaces, and the recombination has to overcome the inner electrical field in the p-n junction.

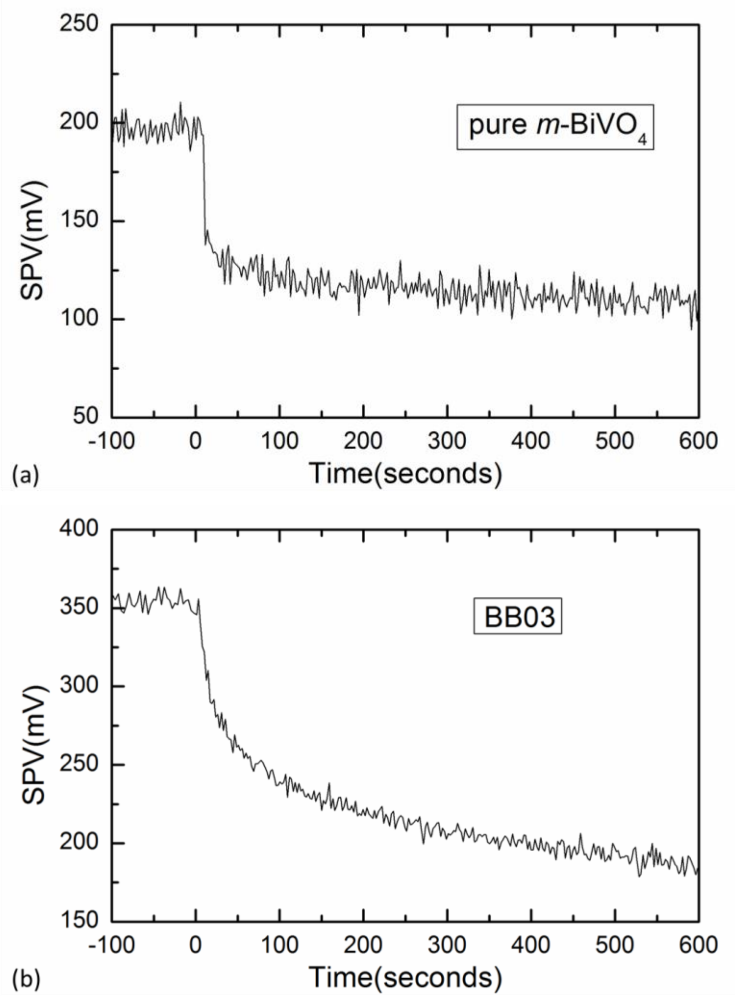

Figure 6.14 Transient SPV spectra of (a) pure *m*-$BiVO_4$ and (b) BB03 after irradiation turned off.

6.7 Concluding remarks

In summary, *m*-$BiVO_4$@γ-Bi_2O_3 composite crystals with core-shell heterostructure have been successfully synthesized based on *m*-$BiVO_4$ crystals under alkaline hydrothermal condition. Such reaction could be considered as a simple "etching" process that the surface V ions of *m*-$BiVO_4$ octahedra dissolve in strong alkaline solution, while the Bi ions precipitate as γ-Bi_2O_3 phase on the *m*-$BiVO_4$ core. It was found that the degree of etching, corresponding to the Bi_2O_3 phase content, was determined by the alkaline concentration and reaction time. In addition, the specific surface area could be increased at the beginning of Bi_2O_3 formation, because of the roughening of the *m*-$BiVO_4$ surface. In the latter reaction, the specific surface area would decrease promptly, which was due to the rapid ripening of Bi_2O_3 phase. The optical property analysis indicated that the *m*-$BiVO_4$@γ-Bi_2O_3 composite crystals exhibited a slightly wider range of visible light response as compared to pure *m*-$BiVO_4$ crystals. And most importantly, these composite powders showed superior photocatalytic performance in the degradation of RhB under visible light irradiation. Besides the increase in specific surface area, such enhancement could be mostly attributed to the p-n heterojunction structure that can promote the charge carrier transfer and reduce their recombination probability. This could also be evidenced by the surface photovoltage spectra. Based on our analysis, the degradation efficiency of RhB after 10 hours reached 86% for the sample BB03, which was 31% higher than pure *m*-$BiVO_4$ crystals.

Chapter 7. Surface Modification of *m*-BiVO$_4$ crystals by loading Au and Pt

7.1 Introduction

In Chapter 6, enhancement of *m*-BiVO$_4$ photocatalytic performance has been derived from the improved charge carrier transfer by compositing *m*-BiVO$_4$@γ-Bi$_2$O$_3$ p-n junctions. As reviewed in Section 2.3, another type of heterogeneous structure, metal/semiconductor Schottky junction, can also effectively promote the charge carrier transfer in a photocatalytic reaction. In addition, the surface plasmon resonance (SPR) effect of noble metal nanoparticles, such as Au, Ag and Pt, has recently been applied in the field of photocatalysis for organic decomposition [101,141-143]. Based on the SPR effect, noble metal nanoparticles can show strong absorption in a wide range of visible light region, thus, can contribute to the overall photocatalytic performance when they are loaded onto the semiconductor surface. So far, variety of metals have been used to achieve metal/BiVO$_4$ heterogeneous structure, including Cu/BiVO$_4$ [107], Pd/BiVO$_4$ [108], Fe/BiVO$_4$ [144], etc.

In this chapter, we report the surface modification of *m*-BiVO$_4$ with either Au or Pt by loading gold or platinum nanoparticles, respectively, on octahedral *m*-BiVO$_4$ crystals through a simple photochemical reduction method. The synthesis method is briefly introduced, followed by extensive characterization and analysis. Significantly, these Au/*m*-BiVO$_4$ and Pt/*m*-BiVO$_4$ heterogeneous nanoparticles exhibited much higher visible-light photocatalytic activities than the pure *m*-BiVO$_4$ nanoparticles. The possible mechanisms behind the photocatalytic enhancement are discussed. Moreover, the photocatalytic performances of Au- and Pt-loaded nanoparticles are also compared and explained.

7.2 Synthesis of Au (or Pt)/m-BiVO$_4$ nanoparticles

As a great effort towards the green chemistry, the photochemical route has been developed for synthesis of noble metal nanoparticles [82,145,146]. In a typical photochemical reaction, as shown in Figure 7.1 (a), electron and hole pairs are generated in the photocatalyst particles under irradiation, where the photogenerated electrons can be transferred to and thus reduce the related ions, while the holes are scavenged by the ethanol. This method has many advantages, such as: the process can be carried out without using any other reducing agent; the reduction reaction is uniform by continuous stirring; and for practical application, this photochemical method is cost-effective and can be scaled up easily.

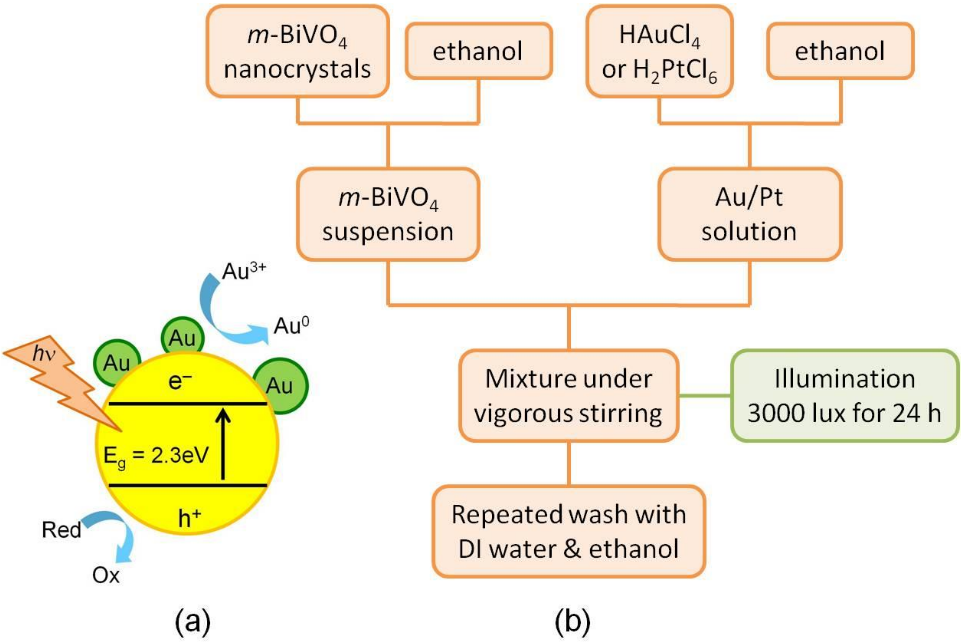

Figure 7.1 (a) schematic illustration of the Au particle formation on the surface of *m*-BiVO$_4$ crystals and (b) synthesis procedure of Au (or Pt)/*m*-BiVO$_4$ nanoparticles.

In our synthesis of Au (or Pt) based on $BiVO_4$ nanoparticles, the synthesis procedure is shown in flow chart Figure 7.1 (b). Small amount of as-obtained octahedral monoclinic *m*-$BiVO_4$ powders, about 500 nm in size, were dispersed in high purity ethanol (99.95%) under vigorous stirring and ultrasonic treatment. Meanwhile, certain amount of $HAuCl_4$ (or H_2PtCl_6) was dissolved in other high purity ethanol to achieve a homogeneous solution. The $HAuCl_4$ (or H_2PtCl_6) solution was then mixed with *m*-$BiVO_4$ suspension, followed by continuous stirring. After that, the mixture was placed under photoirradiation for 24 hours by the fluorescent lamps (8W × 10) with the illuminance around 3000 lux. Finally, the products were repeatedly washed and dried. Based on the wide range investigation on Au-loading (0 ~ 8%), a slightly narrower range (0.5% ~ 4%) was studied for Pt-loading. The Au- and Pt-loaded samples were named as "Au *x*" and "Pt *x*", respectively, where *x* indicating the molecular percentage of noble metals.

Table 7.1 List of sample name, molecular percentage of metal (M = Au, Pt) precursors and resultant weight percentage of metal of the as-prepared M/*m*-$BiVO_4$ nanoparticles.

Sample Name	Molecular percentage of $HAuCl_4$ / H_2PtCl_6 (mol%)	Weight percentage of Au /Pt (wt%)
Au0.3%	0.3	0.18
Au0.5%	0.5	0.30
Au1.0%	1.0	0.61
Au2.0%	2.0	1.23
Au4.0%	4.0	2.47
Au8.0%	8.0	5.02
Pt0.5%	0.5	0.30
Pt1.0%	1.0	0.60
Pt2.0%	2.0	1.21
Pt4.0%	4.0	2.45

7.3 Characterization of Au/m-BiVO$_4$ nanoparticles

Figure 7.2 presents the XRD patterns of the as-prepared *m*-BiVO$_4$ powders with Au loading from 0.3% to 8.0%. It can be seen that all the samples were composed of monoclinic BiVO$_4$ (JCPDC No. 14-0688) as main phase. Moreover, for the powder samples with Au amount more than 1.0%, diffraction peaks of gold metal with cubic structure (JCPDC No. 65-2870) could be found, which clearly indicated the formation of Au secondary phase besides *m*-BiVO$_4$ crystals. Apparently, the intensity of Au diffraction peaks gradually increased with the more Au loading. Although no obvious Au phase could be found in the XRD patterns of the samples Au0.3% and Au0.5%, we suspected that some Au metallic phase was also formed. The slight amount could be lower than the XRD detection limit.

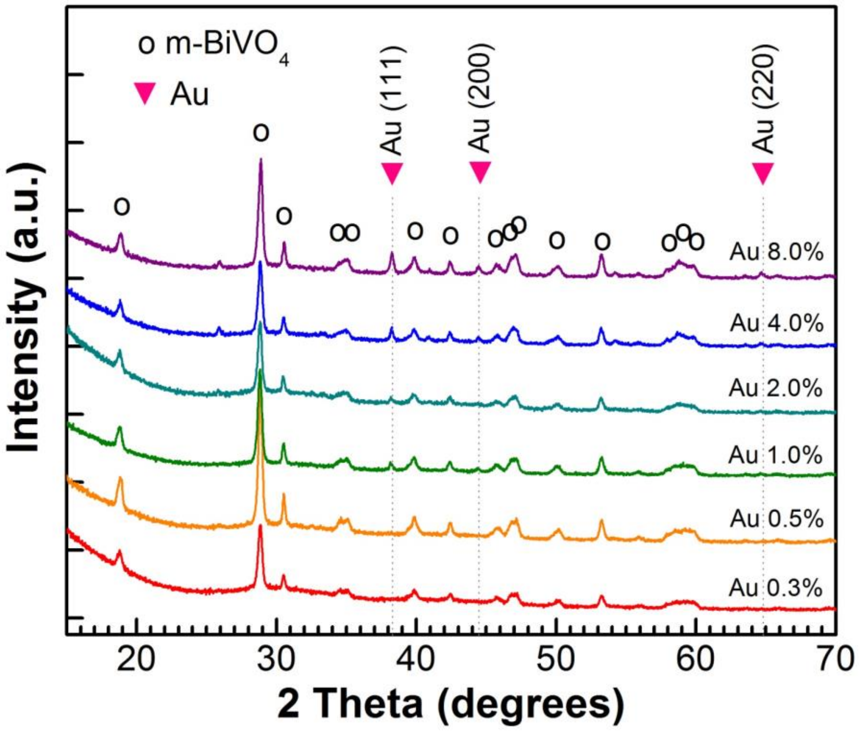

Figure 7.2 XRD patterns of the as-prepared Au/*m*-BiVO$_4$ nanoparticles.

It is also worth to mention that the diffraction peaks of the *m*-$BiVO_4$ phase had not shifted for these Au/*m*-$BiVO_4$ samples. This implied that *m*-$BiVO_4$ crystal structure was not influenced, and Au atoms should not be doped into its crystal lattice. In short, based on the XRD characterization, it was concluded that Au metallic phase could be successfully synthesized through the photochemical reduction method based on the photocatalytic property of *m*-$BiVO_4$, which resulted in binary-phased composite nanocrystals.

The typical SEM images of Au/*m*-$BiVO_4$ nanoparticles in Au4.0% are shown in Figure 7 3 (a) and (b). It was revealed that the *m*-$BiVO_4$ crystals still maintained the octahedral morphology, while some gold nanoparticles were stuck onto the surface of *m*-$BiVO_4$ octahedra. The size of these gold nanoparticles was around 50~100 nm. In the EDX area analyses, the Au content in the composite sample Au4.0% was found around 4.04%, which was close to the reagent amount ratio present. Thus, the composition analysis of product powder was consistent and most of the $HAuCl_4$ were successfully reduced into Au particles by our photocatalytic synthesis. Moreover, the SEM and TEM observations revealed that most Au nanoparticles were well attached onto the *m*-$BiVO_4$ surface, while few could be found separated. This could be well evidenced by the TEM-mapping analysis as shown in Figure 7.4. It can be seen that Au crystals were formed at the corner of an *m*-$BiVO_4$ octahedral crystal, while leaving a spherical surface outside for lower surface energy. Such good connection between gold nanoparticles and *m*-$BiVO_4$ crystals was considered to be the key factor for the efficient separation of photogenerated electron-hole pairs in the enhancement of photocatalytic performance.

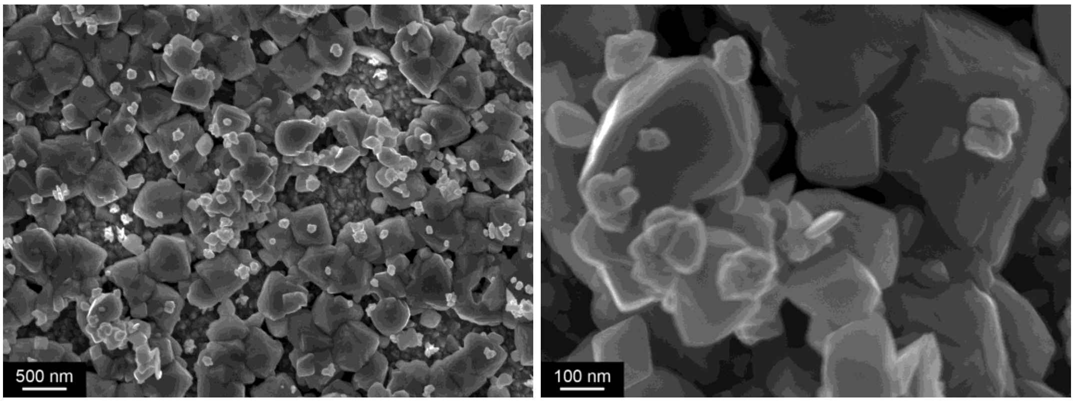

(a) (b)

Figure 7.3 (a) low and (b) high magnification SEM images of Au4.0%.

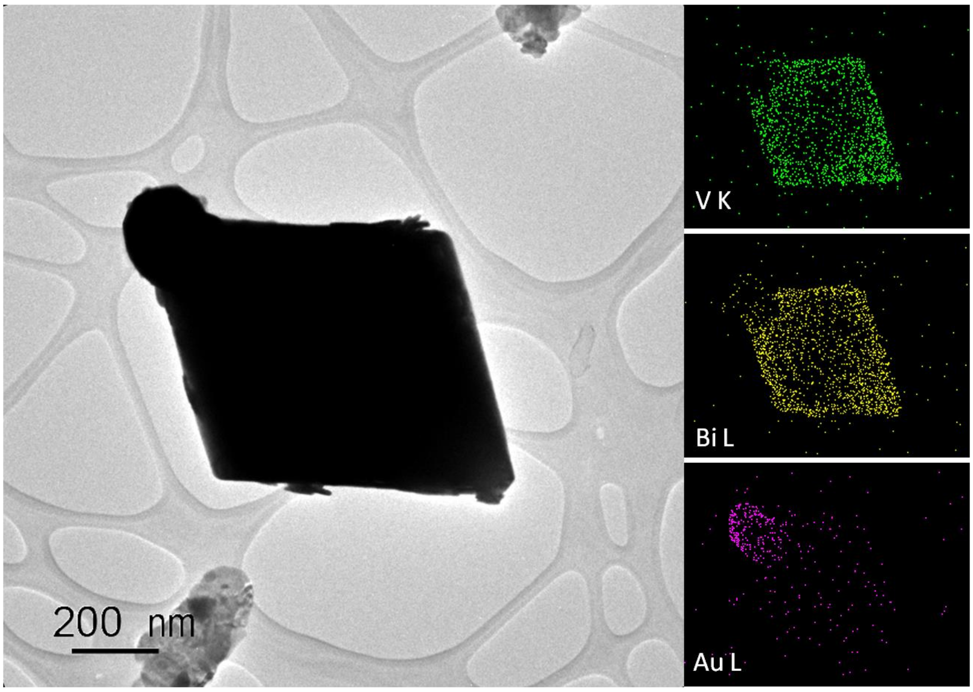

Figure 7.4 TEM image of a composite nanocrystal in Au4.0% with elemental mapping under STEM-EDX.

The Au species in these Au/*m*-$BiVO_4$ composite nanoparticles were also investigated by the X-ray photoelectron spectroscopy (XPS). Figure 7.5 (a) represents the typical XPS spectra for Au/*m*-$BiVO_4$ composite nanoparticles (Au4.0%), which clearly indicated the existence of Au species. Moreover, the fine scan of Au 4f doublet in Figure 7.5 (b) indicated the binding energy of 87.8 eV and 84.1 eV for Au 4f (5/2) and 4f (7/2), respectively, with the spin energy separation about 3.7 eV. The binding energy values correspond to metallic gold [147,148]. Thus, it could be deduced that the gold atoms were not oxidized into compound, but presented as gold metal among the *m*-BiVO$_4$ crystals. At this point, both XRD results and XPS analysis have indicated the formation of Au/*m*-BiVO$_4$ composite material with mixed crystal phases.

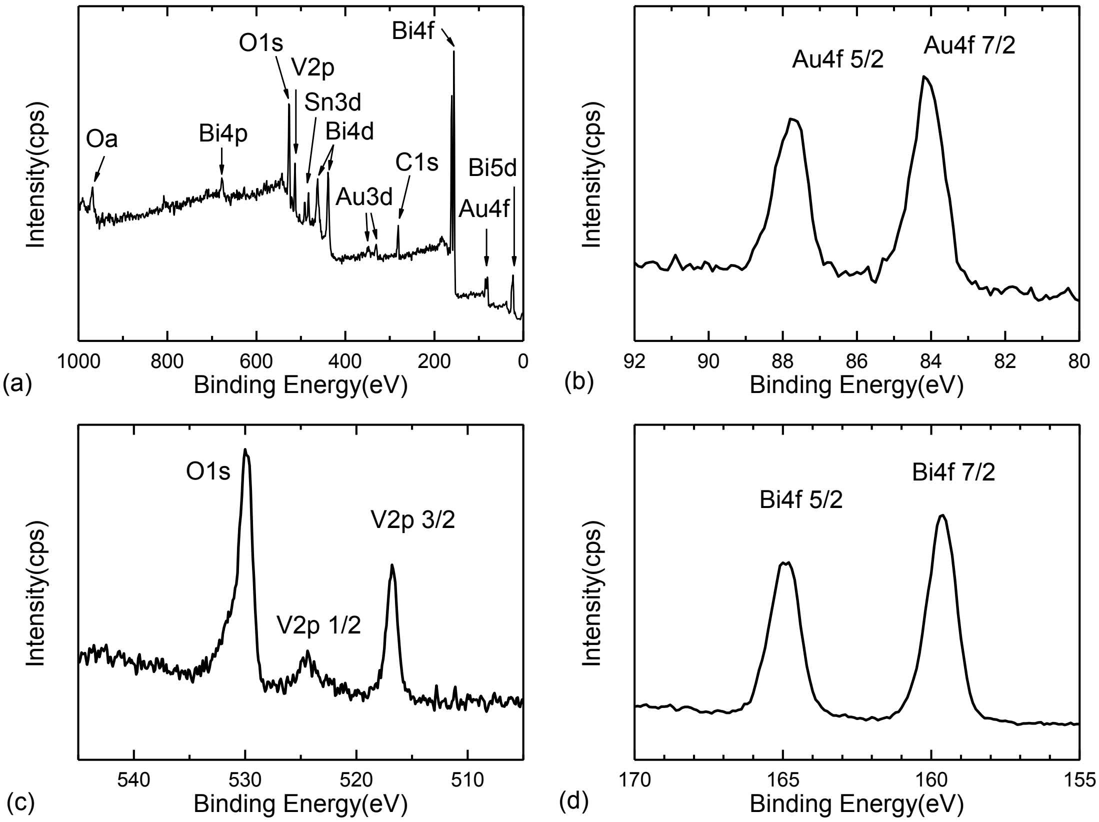

Figure 7.5 (a) XPS full scan spectrum of Au4.0% with (b), (c) and (d) fine scan spectra on main elements.

7.4 Photo-physical properties of Au/m-BiVO$_4$

The energy band structure feature of a semiconductor is considered as the key factor in determining its optical properties, thus influencing the photocatalytic activity. Figure 7.6 shows the UV-Vis diffused reflectance spectra of these six as-synthesized Au/*m*-BiVO$_4$ composites, as well as the pure *m*-BiVO$_4$ sample. All the six modified samples showed absorption bands in the visible light region, 520 ~ 530 nm, which were slightly blue shift compared to that of the pure octahedral *m*-$BiVO_4$.

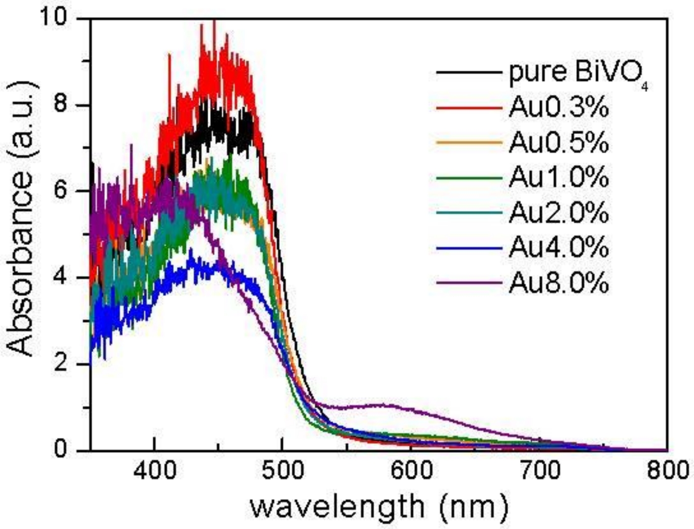

Figure 7.6 UV-Vis diffused reflectance spectra of the as prepared pure and Au-loaded *m*-$BiVO_4$ nanoparticles.

On the contrary, along with much darker color in appearance, the absorption edge of Au4.0% and Au8.0% shifts to red light, around 535 nm and 550 nm, respectively. This opposite change could be explained by the heavy loading of gold in these two samples. Since more gold particles were formed on *m*-$BiVO_4$ nanocrystals, they could cover the most surface area of the oxide, or could even constitute a metallic shell. Eventually, the high coverage or shell formation of gold nanoparticles significantly hindered the light absorption of *m*-$BiVO_4$, and resulted in the abrupt change of overall optical property of the composite.

Table 7.2 RhB degradation efficiencies after 12 hours irradiation and specific surface area (BET) of the as-prepared Au/*m*-BiVO$_4$ composite samples.

Sample Name	Degradation efficiency ($1-C_{12}/C_0$)	Specific surface Area (m^2/g)
Pure *m*-BiVO$_4$	87.0%	2.34
Au0.3%	88.9%	2.31
Au0.5%	95.0%	2.24
Au1.0%	99.5%	2.29
Au2.0%	71.8%	1.57
Au4.0%	57.6%	0.93
Au8.0%	57.3%	0.46

The photocatalytic activities of the as-prepared Au/*m*-BiVO$_4$ composite nanoparticles were evaluated by the photodegradation of RhB under visible light irradiation. The results were compared with that of the pure *m*-BiVO$_4$ octahedral crystals in Figure 7.7 (a). The overall degradation efficiencies for each sample, after 12 hours reaction, were also calculated and listed in Table 7.2. It was clearly seen that small amount of Au-loading could effectively improve the visible-light photocatalytic activity. However, if Au-loading was higher than 2%, the photocatalytic performance became worse than the pure *m*-BiVO$_4$ crystals. The overall degradation efficiency of the composite Au/*m*-BiVO$_4$ samples, after 12 h degradation of RhB, were plotted as the function of Au content, as illustrated in Figure 7.7 (b). Obviously, among these samples, Au1.0% exhibited the best photocatalytic performance with the highest degradation efficiency, and photochemical oxidation of RhB dye could almost be completed after 12 h of irradiation.

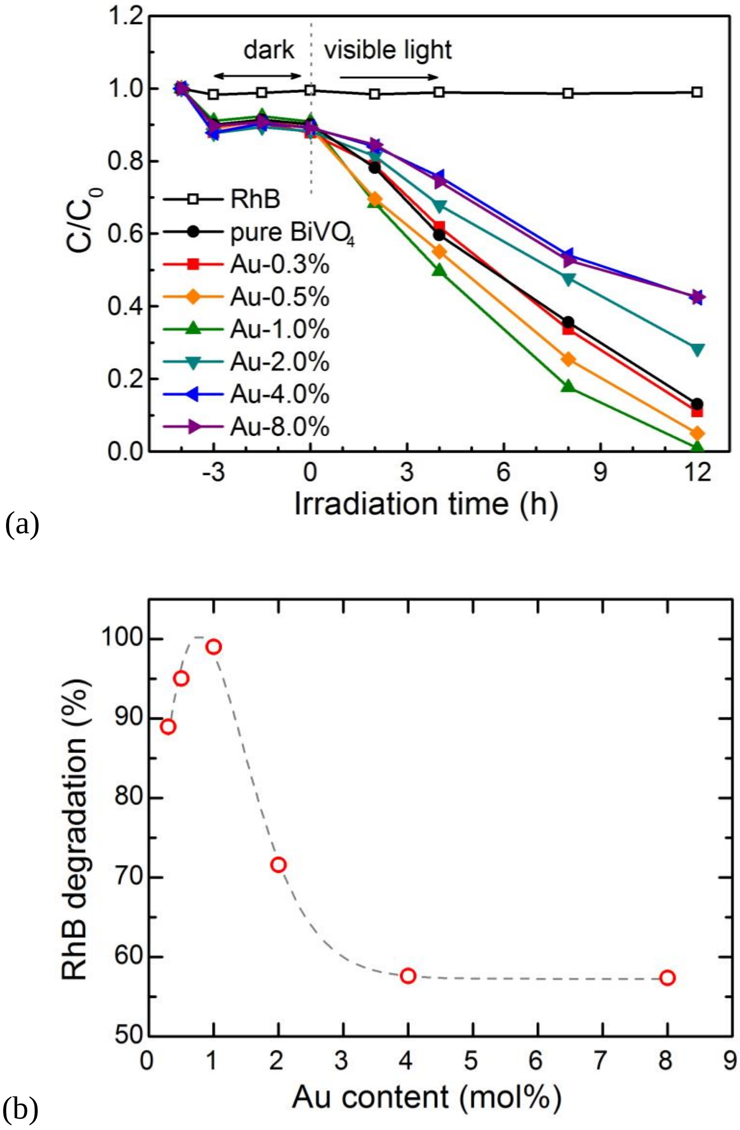

Figure 7.7 (a) The photocatalytic degradation of RhB and (b) 12-h degradation efficiency of the An/*m*-BiVO$_4$ composite samples.

The photodegradation test on organic dye clearly indicated the photocatalytic enhancement of *m*-BiVO$_4$ nanocrystals through the surface modification of gold nanoparticles. This could be attributed to the promoted charge carrier separation, which is detailed in the next section. The worse photocatalytic performance of heavily Au-loaded *m*-BiVO$_4$ crystals could be attributed to several factors. Firstly, if exceeds the optimum content, Au can also act as recombination centers and reduce the charge separation efficiency, as suggested by Ge [108]. Secondly, excess Au may cover the active sites of m-BiVO$_4$ for the photo-oxidation as reported by Zhang et al [110]. Thirdly, too much Au loading may also form thick Au shell that hindered the light absorption of m-BiVO$_4$ core. Last but not the least, according to our study, abundant Au photosynthesis could result in significant agglomeration of the m-BiVO$_4$-based nanoparticles as well as the abnormal growth of gold crystal. As shown in Figure 7.8, m-BiVO$_4$ nanoparticles were united by Au, and resulted in large particle agglomeration, about 10 micron in diameter. In addition, some m-BiVO$_4$ crystals were fully covered by fast grown gold species. Eventually, the specific surface area of the nanoparticles was greatly reduced, as listed in Table 7.2, thereby decreasing the photocatalytic activity.

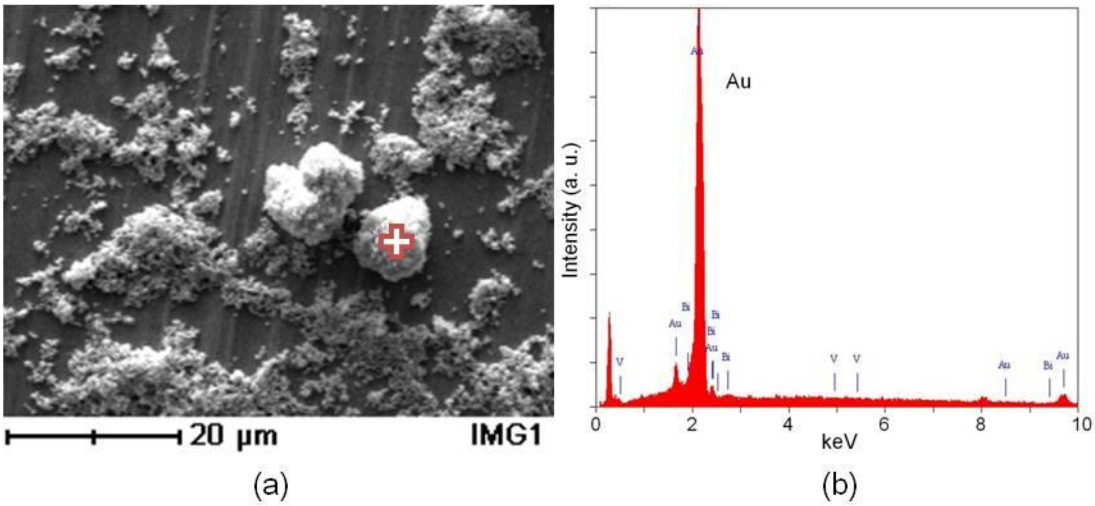

Figure 7.8 (a) SEM image and (b) spot EDX spectrum of Au8.0% derived from the marked point in (a), which indicated significant agglomeration by heavy Au-loading.

7.5 Enhance mechanism of metal loading

The photocatalytic performance of these m-BiVO$_4$ nanoparticles was successfully improved by a small amount loading of Au particles as surface modification. Based on our results, this could be mostly attributed to the enhanced separation of photogenerated electron-hole pairs by the Schottky junction at Au/m-

$BiVO_4$ interfaces. It is known that the Fermi level of Au is around 0.5 eV (versus NHE) [113,149], which is larger than the conduction band (CB) edge of n-type *m*-$BiVO_4$ (0.3 ~ 0.4 eV versus NHE). When Au nanoparticles were prepared on *m*-$BiVO_4$ surface through the photochemical reduction, electron migrated from the oxide to Au until the two Fermi levels were equal and a thermodynamic equilibrium was reached. At this time, the ohmic contact has formed a Schottky junction with the establishment of a Schottky barrier, as illustrated in Figure 7.9 (a). The barrier height (Φ_b) is the energy difference between the work function of gold (Φ_{Au}) and the electron affinity of *m*-$BiVO_4$ (E_χ) [150]:

$$\Phi_b = \Phi_{Au} - E_\chi \qquad (7\text{-}1)$$

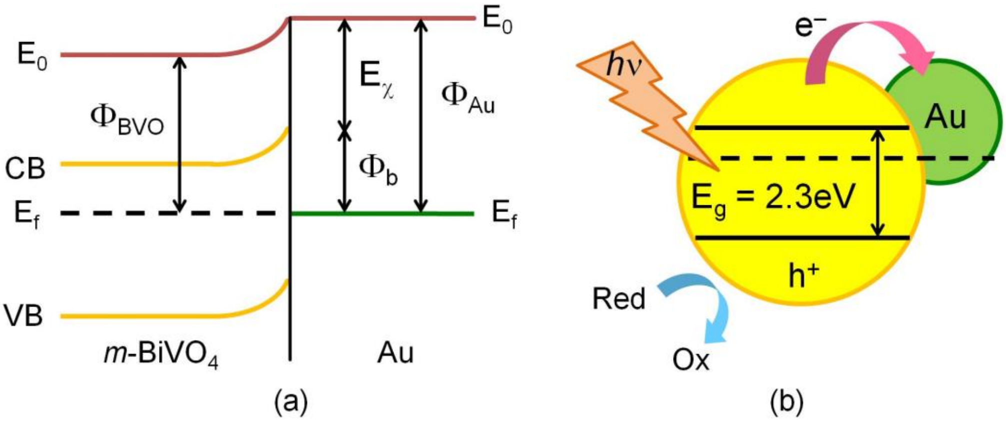

Figure 7.9 Schematic illustration of (a) the Schottky barrier between *m*-$BiVO_4$ and Au and (b) the enhanced separation of electron-hole pair at the interface of Au/*m*-$BiVO_4$ composite.

As a result, when *m*-$BiVO_4$ was irradiated by visible light with photon energy larger than its band gap, electrons in the valance band (VB) were excited to the CB, while the holes remained in the VB. Under the effect of Schottky barrier at the interface, the photogenerated electrons would continuously migrate across the junction to gold, while holes were diffused to the *m*-$BiVO_4$ surface for the oxidation reaction, as shown in Figure 7.9 (b). Such an electron transfer process could effectively limit the electron-hole recombination and thereby enhance the photocatalytic performance.

To validate the above analysis, we also performed the photoluminescence (PL) analysis for these Au/*m*-$BiVO_4$ photocatalysts, which has been widely applied to disclose the migration, transfer, and recombination processes of the photogenerated electron-hole pairs in semiconductors [90]. Figure 7.10 represents the PL spectra of pure and Au-loaded *m*-$BiVO_4$ nanoparticles with the excitation wavelength of 350 nm.

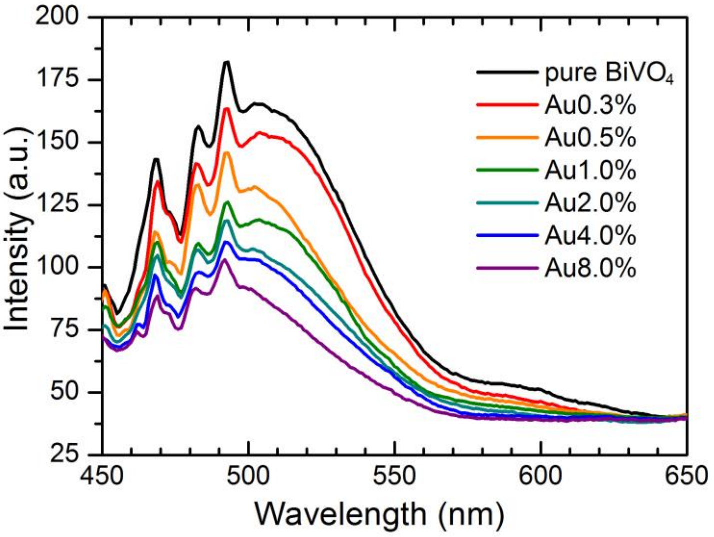

Figure 7.10 Photoluminescence (PL) spectra of Au/*m*-$BiVO_4$ nanoparticles.

It was found that the PL emission spectra of all the samples showed the main peaks at 468 nm, 482 nm and 491 nm as well as a big hump at around 500 nm. In addition, as the Au loading content increased, the PL peak intensities were significantly reduced, which clearly indicated that the recombination of the hole formed in the O 2p band and the electron in the V 3d band was effectively suppressed by the Au-loading onto the *m*-$BiVO_4$ surface.

Besides the charge separation enhancement through Au/*m*-$BiVO_4$ heterogeneous junction, other mechanisms were also proposed in noble metal loaded semiconductor photocatalysts. For example, it has been recently reported that noble metal nanoparticles exhibit strong absorption in the range of visible light due to surface plasmon resonance (SPR) effect, which can boost the photocatalytic activity of TiO_2 [142,151]. In our experiment, light absorption peak at around 630 nm could also be found, as indicated in Figure 7.6 (a), which could be attributed to the SPR of Au nanoparticles. However, pronounced SPR absorption peak could only be found in heavily Au-loaded sample, Au8.0%. Thus, SPR effect may not be dominant in the photocatalytic improvement of *m*-$BiVO_4$ nanoparticles. In other reported work on Pt/*m*-$BiVO_4$ composite photocatalyst, $PtCl_4$ was found in the final products, and was considered to contribute photocatalytic activity through photosensitization effect. Nevertheless, this mechanism should not be involved in our Au/*m*-$BiVO_4$ nanoparticles (as well as the Pt/*m*-$BiVO_4$ samples in the latter sections), since Cl species was not present in our samples as indicated by the XPS analysis.

In summary, the significant photocatalytic enhancement in these Au/*m*-$BiVO_4$ nanoparticles in our work was mostly attributed to the improved separation of photogenerated electron-hole pairs resulting from the formation of Schottky junction at the Au/*m*-$BiVO_4$ interface.

7.6 Synthesis and Characterization of Pt/m-$BiVO_4$

Based on the previous study, heavy Au loading leaded to the agglomeration of *m*-$BiVO_4$ nanocrystals, thus, limited the enhancement on photocatalytic performance. It is well known that Pt has better dispersion performance in coating and surface modification of nanoparticles. Thus, it is quite promising to use Pt instead of Au in the surface modification of *m*-$BiVO_4$ nanoparticles towards higher photocatalytic performance. In this part of work, Pt/*m*-$BiVO_4$ nanoparticles were prepared by similar photocatalytic reduction method, and studied as follows.

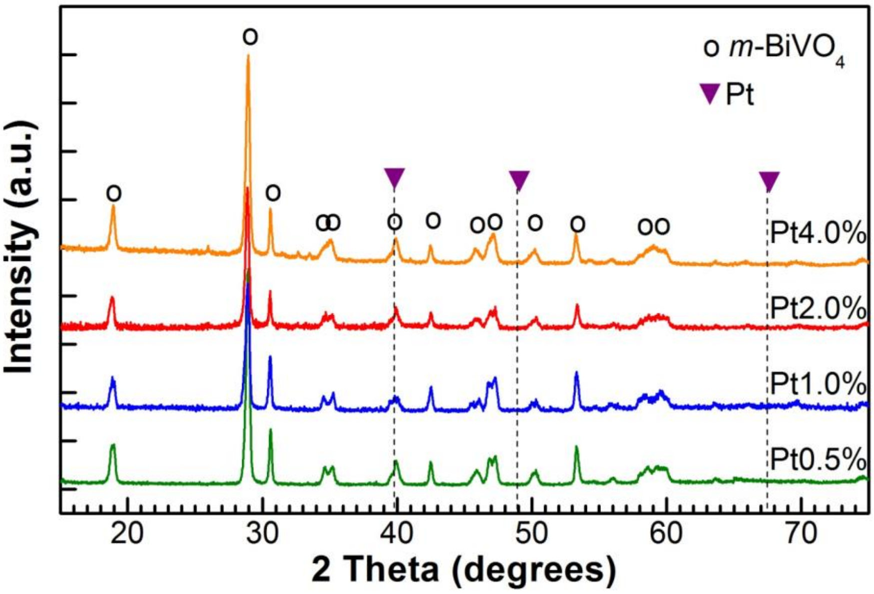

Figure 7.11 XRD patterns of the as-prepared Pt/*m*-$BiVO_4$ nanoparticles.

Figure 7.11 represents the XRD patterns of the as-prepared Pt/*m*-$BiVO_4$ nanoparticles with 0.5 % to 4.0 % Pt loadings. It can be seen that all the samples are well crystallized, and the $BiVO_4$ still maintained the monoclinic structure (JCPDC No. 14-0688). Similar to the Au-loading results, no diffraction peak shift could be found for the Pt-loaded samples, which indicated the absence of Pt-doping into the *m*-$BiVO_4$ crystal structure. Due to the very low content of Pt phase among *m*-$BiVO_4$ crystals, the diffraction peaks of cubic Pt (JCPDC No. 65-2868) were very weak in these XRD patterns. Especially, the strongest one, Pt (111) at $2\theta = 39.8°$, was not obvious due to the overlap with the (211) peak of *m*-$BiVO_4$.

In contrast, Pt could be easily found under SEM/TEM observation combined with EDX analysis. The typical SEM image, as shown in Figure 7 12 (a) and (b), revealed that many Pt nanoparticles, with particle size around 10 ~ 30 nm, were homogenously deposited on the octahedral *m*-$BiVO_4$ nanocrystals.

The TEM observation and EDX line scan further confirmed the formation of Pt phase and the heterogeneous nanostructure. As indicated in Figure 7.13, some Pt nanoparticles, with less than 10 nm size, were found on the surface of *m*-$BiVO_4$ octahedra. In addition, these Pt particles were well crystallized and were firmly attached onto *m*-$BiVO_4$ crystal surface. The chemical state of Pt species in these Pt/*m*-$BiVO_4$ composite nanoparticles was also studied by XPS analysis, as shown in Figure 7.14. The XPS fine scan spectra of Pt 4f doublet on the sample Pt2.0% demonstrated only the pronounced signal of Pt with binding energy of 71.25 eV and 74.60 eV, as well as a spin energy separation about 3.35 eV, which corresponded to metallic platinum [152]. Thus, similar to the experiment results in gold loaded *m*-$BiVO_4$ samples, all Pt reagents were reduced into metallic platinum nanoparticles on the surface of on *m*-$BiVO_4$ octahedral crystals, and resulted in binary phased Pt/*m*-$BiVO_4$ composite.

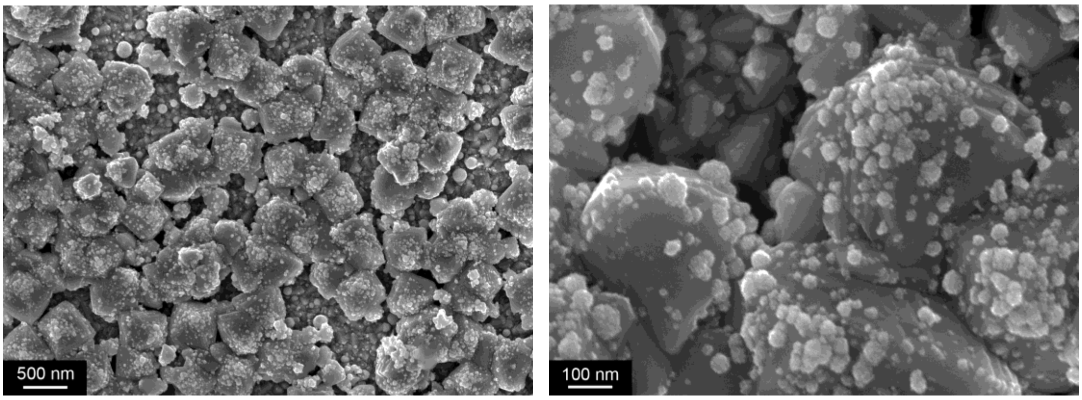

(a) (b)

Figure 7.12 (a) Low and (b) high magnification SEM images of Pt2.0%.

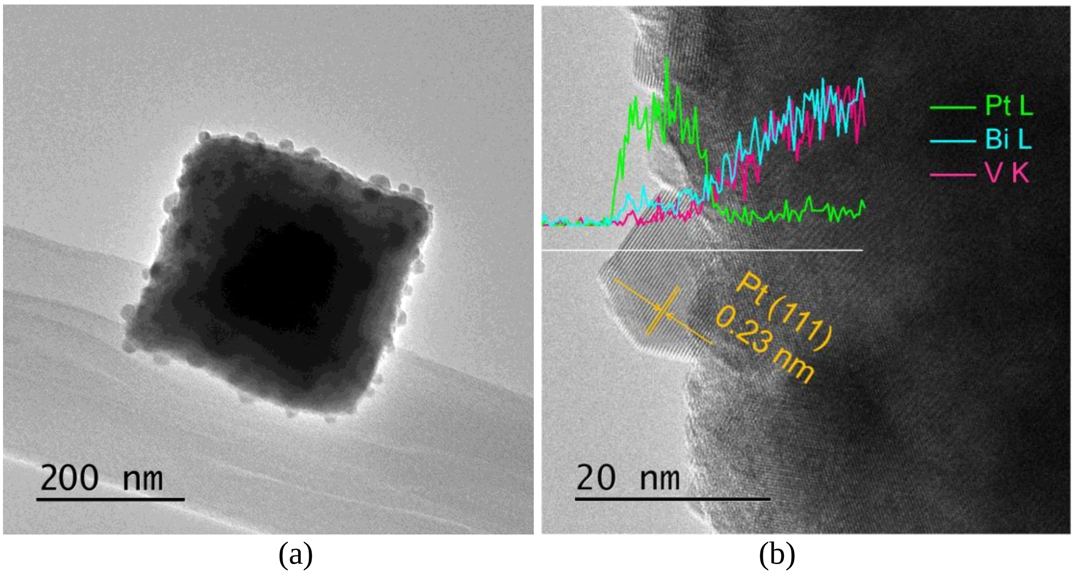

Figure 7.13 (a) TEM image and (b) STEM line scan analysis of a Pt/*m*-BiVO$_4$ composite crystal in Pt2.0%.

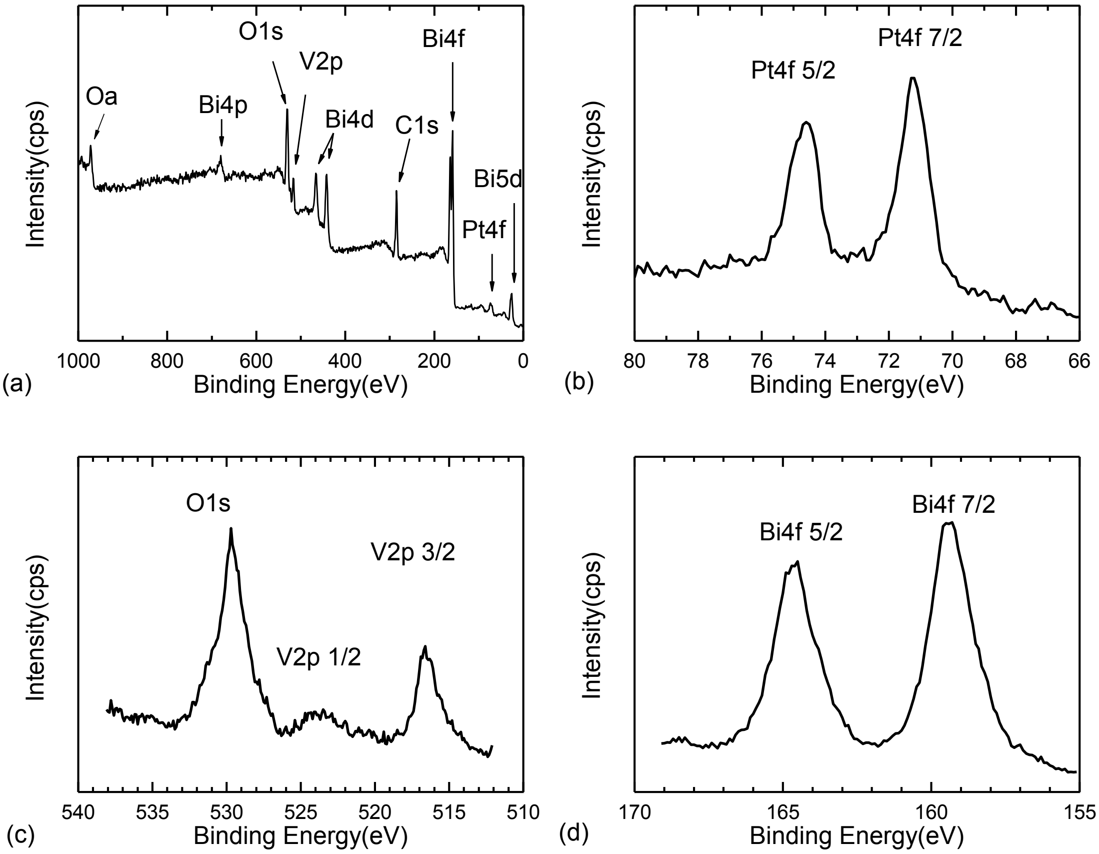

Figure 7.14 (a) XPS full scan spectrum of Pt2.0% with (b), (c) and (d) fine scan spectra on main elements.

7.7 The photo-physical properties of Pt/m-BiVO$_4$

Figure 7.15 shows the UV-Vis diffused reflectance spectra of four as-synthesized Pt/*m*-BiVO$_4$ composite nanoparticles, as compared with that of the pure *m*-BiVO$_4$ sample. All the four modified samples showed absorption bands in the visible light region around 530 nm. Thus, within the investigated range of Pt loading content, the optical property of Pt/*m*-BiVO$_4$ nanoparticles remained almost unchanged.

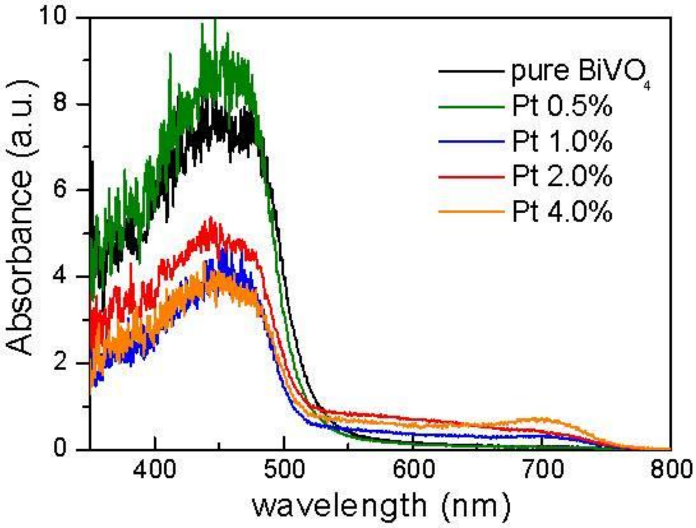

Figure 7.15 UV-Vis diffused reflectance spectra of the as prepared pure and Pt-loaded *m*-BiVO$_4$ nanoparticles.

The Pt/*m*-BiVO$_4$ nanoparticles showed superior photocatalytic performance under visible light, where the degradation of RhB could be mostly completed after 10 hours irradiation. The results were compared with the pure *m*-BiVO$_4$ nanoparticles, as plotted in Figure 7.16, and the overall degradation efficiencies of each sample are listed in Table 7.3. Especially, the sample Pt2.0% exhibited the highest degradation activity among these samples, and the degradation time could be reduced to around 7 hours. Further investigation on these nanoparticles indicated that the specific surface area did not affect much by the Pt nanoparticles load. Thus, different from the formation of Au nanoparticles, the loading of Pt onto *m*-BiVO$_4$ crystals did not result in severe particle agglomeration. Therefore, improvement of photocatalytic performance could be observed in all these Pt/*m*-$BiVO_4$ nanoparticles, including the heavily loaded sample, Pt4.0%. Nevertheless, the optimum loading amount of Pt nanoparticles was found to be 2%, while the slight worse photocatalytic performance of Pt4.0% might due to the over high coverage of Pt nanoparticles that blocked the active site of *m*-$BiVO_4$ in the photoinduced oxidation reaction.

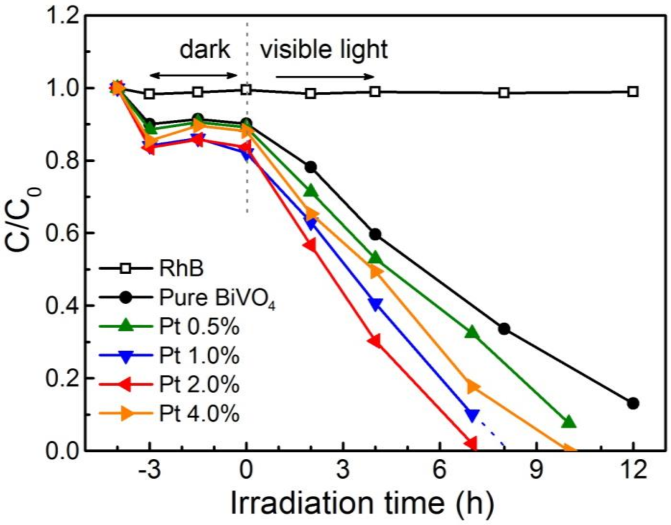

Figure 7.16 The photocatalytic degradation of RhB for as-prepared Pt/*m*-$BiVO_4$ composite samples.

Table 7.3 RhB degradation efficiencies after 10 hours irradiation (12 hours for pure *m*-$BiVO_4$) and specific surface area (BET) of the as-prepared Pt/*m*-$BiVO_4$ composite samples.

Sample Name	Degradation Efficiency $1-C_{10}/C_0$	Specific surface Area (m^2/g)
Pure *m*-$BiVO_4$	87%	2.34
Pt0.5%	99%	2.33
Pt1.0%	100%	2.34
Pt2.0%	100%	2.30
Pt4.0%	95%	2.25

The photoluminescence (PL) analysis was also performed for these Pt/*m*-$BiVO_4$ nanoparticles. The spectra in Figure 7.17 clearly showed that the main PL peaks of these Pt/*m*-$BiVO_4$ nanoparticles were still located at 468 nm, 482 nm and 491 nm as well as a big hump at around 500 nm, which was the same as the pure *m*-$BiVO_4$ sample. As the Pt-loading content was increased, the PL peak intensities were significantly decreased. Especially for Pt4.0%, the PL hump at around 500 nm disappeared, and most PL phenomenon was inhibited. The PL spectra of these Pt/*m*-$BiVO_4$ nanoparticles were consistent with the results from Au-loaded samples, which clearly indicated the improved charge transfer through the metal-oxide heterojunction, thus the suppressed recombination of electron-hole pairs in the photocatalytic reaction. As discussed in previous Section 7.4, this was considered as one of the most important mechanism in the enhancement of photocatalytic activity in these surface modified *m*-$BiVO_4$ nanocrystals.

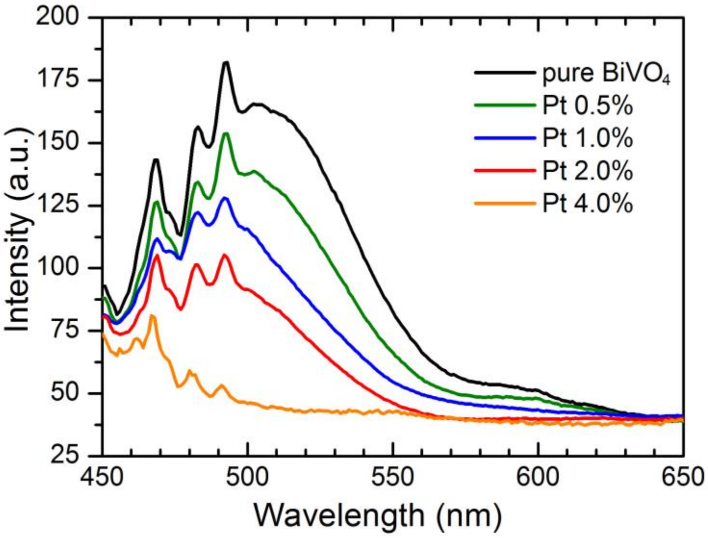

Figure 7.17 Photoluminescence (PL) spectra of Pt/*m*- $BiVO_4$ nanoparticles.

7.8 Comparison of Au- and Pt-loading

The photocatalytic performance of the two best Pt-loaded *m*-$BiVO_4$ samples were compared with two Au-loaded counterparts, as shown in Figure 7.18 (a). Obviously, Pt1.0% and Pt2.0% exhibited higher photocatalytic activity by much faster RhB degradation. Further, the degradation efficiencies of all these composite samples were plotted against the metal loading contents, which could clearly illustrate the different influences of the two loading metals, as shown in Figure 7.18 (b). It is found that all the Pt-loaded *m*-$BiVO_4$ nanoparticles showed better photocatalytic performance than Au-loaded samples with the same metal contents. In addition, the optimum loading amount of Pt was around 2.0%, which was higher than the best Au-loaded sample, ~1.0%.

Based on our experiments, these differences were most likely originated from the different growth behavior of Au and Pt nanoparticles on *m*-$BiVO_4$ nanoparticles. As indicated in Figure 7.19, Pt nanoparticles exhibited better dispersion on the surface of *m*-$BiVO_4$ crystals, while Au could agglomerate into much larger particles. Hence, in Pt-loaded nanoparticles, more metal-oxide heterojunction could be created, which contributed more to the electron-hole separation. However, for Au-loaded samples, over-large gold particles would hinder the visible light irradiation onto junctions, as well as block the active sites of *m*-$BiVO_4$ for dye oxidation. Moreover, the great agglomeration of gold was also able to unit *m*-$BiVO_4$ crystals through further Au formation and growth. As a consequence, heavily Au-loaded *m*-$BiVO_4$ nanoparticles resulted in dramatically decreased specific surface area. On the contrary, as compared in Figure 7.18 (c), the BET results of Pt-loaded samples were not affected too much. Therefore, slightly heavy Pt loading only served higher coverage of *m*-$BiVO_4$ surface, and the optimum Pt-loading sample was found with higher metal content, 2.0%.

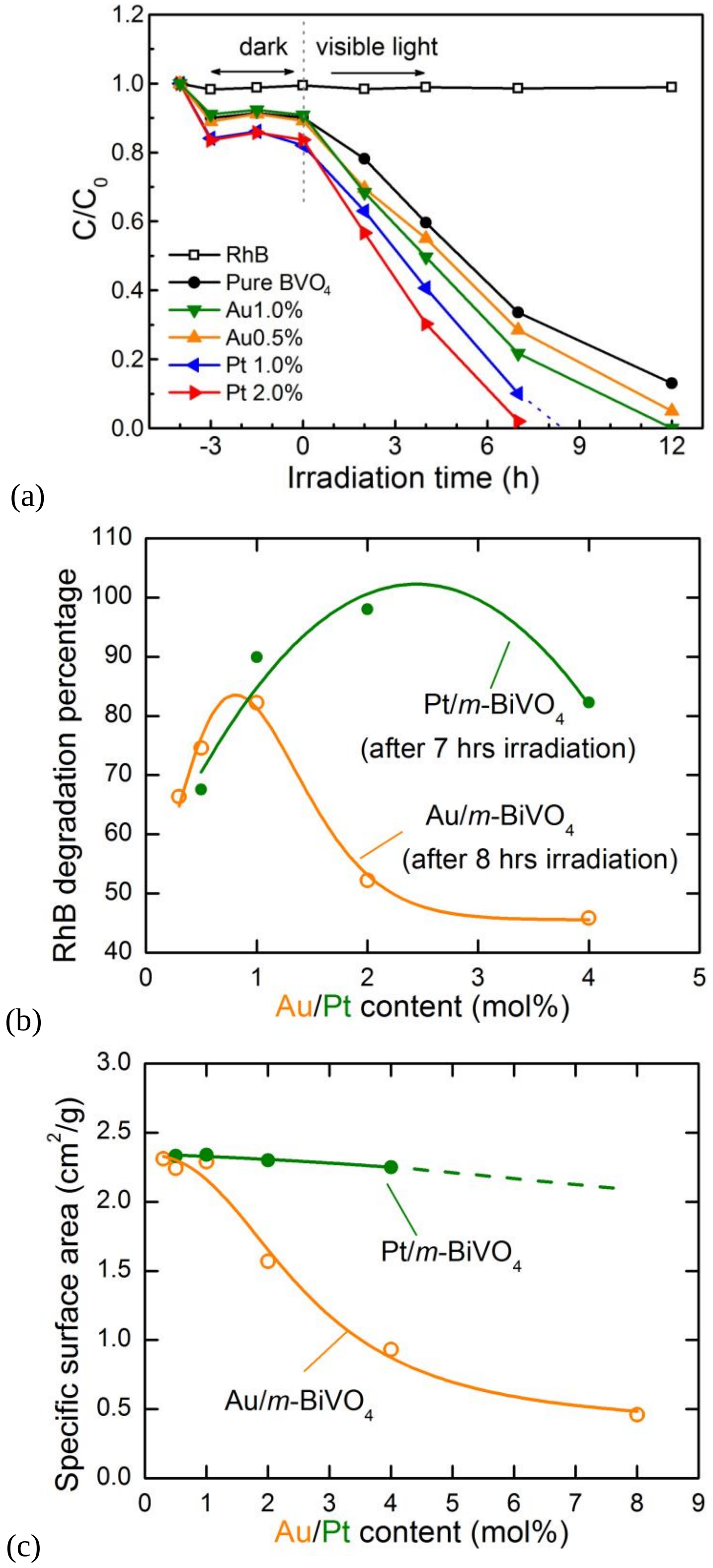

Figure 7.18 Comparison between Au- and Pt-loading on *m*-BiVO$_4$ crystals in (a) the photocatalytic degradation of RhB along irradiation time, (b) the photocatalytic enhancement in terms of degradation efficiency and (c) the influences on specific surface area.

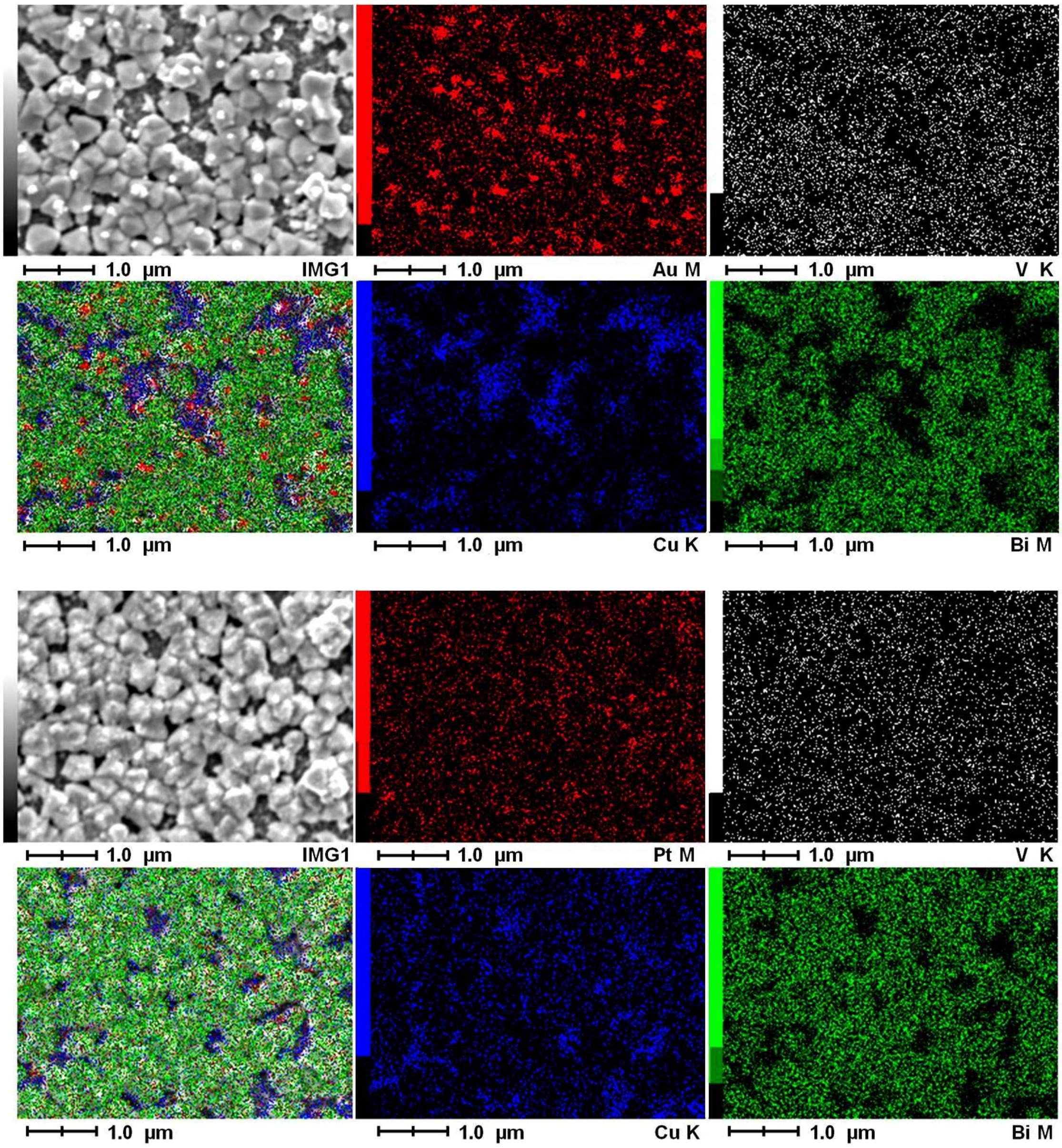

Figure 7.19 SEM mapping results of Au1.0% (up) and Pt1.0% (down) composite nanoparticles.

In this section, both specific surface area and heterogeneous structure are important in determining the photocatalytic performance of the *m*-$BiVO_4$-based crystals. High specific surface area ensures large amount of photo-induced electron-hole pairs, while surface modification with Au/Pt can help on the separation of these electron-hole pairs. In one case, for Pt-loaded *m*-$BiVO_4$ samples and lightly Au-loaded ones, the specific surface area is only decreased slightly. Thus, the negative influence on photocatalytic property is limited. In contrast, the formation of heterojunction can effectively improve the charge separation, and can provide more significant contribution to the photocatalytic performance. So the influence of specific surface area is compensated and cannot be reflected in degradation results. In another case, for the heavily Au-loaded samples (Au > 2%), the specific surface area is found to decrease dramatically. Hence the negative influence becomes significant, and these samples resulted in lower degradation efficiency.

7.9 m-$BiVO_4$/γ-Bi_2O_3/Pt composite

The successful two approaches, by forming heterojunction structure with γ-Bi_2O_3 and surface modification with noble metals, respectively, are actually possible to be combined to further improve the photocatalytic performance of *m*-$BiVO_4$ nanocrystals. Very recently, multiple modification of $BiVO_4$ has been attempted for photocatalysis enhancement. Li Can's group reported that *m*-$BiVO_4$ micron-sized particles loaded with Pt and RuO_2 co-catalysts exhibit better photocatalytic activity in thiophene oxidation [103]. In the study done by Long's group, micron-sized $BiVO_4$ was modified by Ag/AgCl composite [102]. The coupling Ag-AgCl composite was found beneficial in $BiVO_4$ photocatalytic degradation of methyl orange. In another works, cobalt-phosphate has been used to modify W- or Mo-doped $BiVO_4$ electrode, which was claimed to improve the water oxidation performance [153,154]. In our previous study, it was quite successful to enhance the separation of electron-hole pairs, hence improve the photocatalytic performance of *m*-$BiVO_4$, by forming heterojunction structure with γ-Bi_2O_3 and surface modification with noble metals. In this part, both approaches are combined together by loading Pt on *m*-$BiVO_4$@γ-Bi_2O_3 composite for further photocatalytic improvement.

A multi-composite sample, named as BBPt, was prepared based on the optimized compositions: BB03 and Pt2.0%, in Chapter 6 and 7, respectively. Firstly, through the “etch” reaction in alkaline as developed in Chapter 6, *m*-$BiVO_4$/γ-Bi_2O_3 heterogeneous nanostructure were prepared based on *m*-$BiVO_4$ octahedral nanoparticles with crystal size around 400~500 nm. Then certain amount of Pt nanoparticles (2 mol%) were synthesized on the resultant *m*-$BiVO_4$@γ-Bi_2O_3 composite nanoparticles by using the photochemical reaction mentioned in this Chapter 7. The final product, BBPt, was investigated in comparison with BVO (the pure *m*-$BiVO_4$ octahedral nanocrystals around 400~500 nm, in Chapter 5) and BPt (the Pt2.0% in this Chapter 7).

The XRD pattern of BBPt in Figure 7.20 clearly indicated the formation of γ-phased Bi_2O_3 (JCPDC No. 45-1344) among the monoclinic $BiVO_4$ structure (JCPDC No. 14-0688). Similar to the XRD pattern of BPt, neither the diffraction peaks of *m*-$BiVO_4$ were shifted by Pt-loading, as compared to the pattern of BVO, nor the cubic Pt phase (JCPDC No. 65-2868) could be observed, since the loading amount was small.

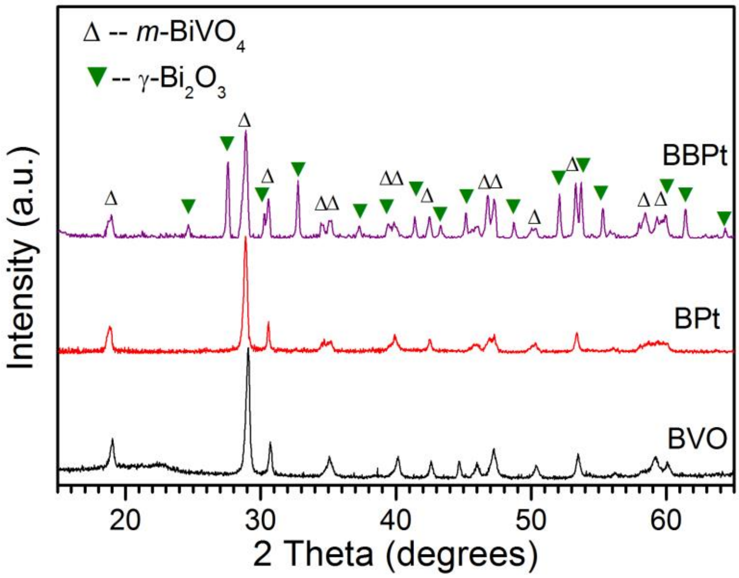

Figure 7.20 XRD patterns of the as-prepared m-$BiVO_4$/γ-Bi_2O_3/Pt composite nanoparticles.

The state and location of Pt species were disclosed by STEM observation combined with EDX analysis, as shown in Figure 7.21. The results clearly indicated the *m*-$BiVO_4$@γ-Bi_2O_3 core-shell heterogeneous nanostructure of the main particle, where some of the outside part (the grey area in Figure 7.21) corresponded to γ-Bi_2O_3 phase, and the inside region (the dark body in Figure 7.21) represented the *m*-$BiVO_4$ core crystal. In addition, some nanoparticles, around 10~20 nm, could be found on the surface of either Bi_2O_3 or $BiVO_4$ phase, and they were recognized as Pt species by EDX analysis. Thus, from the STEM-EDX investigation, it was concluded that the *m*-$BiVO_4$/γ-Bi_2O_3/Pt composite nanostructure has been successfully fabricated, where the step-by-step synthesis route as well as the morphology evolution of the nanostructure could be schematically illustrated in Figure 7.22.

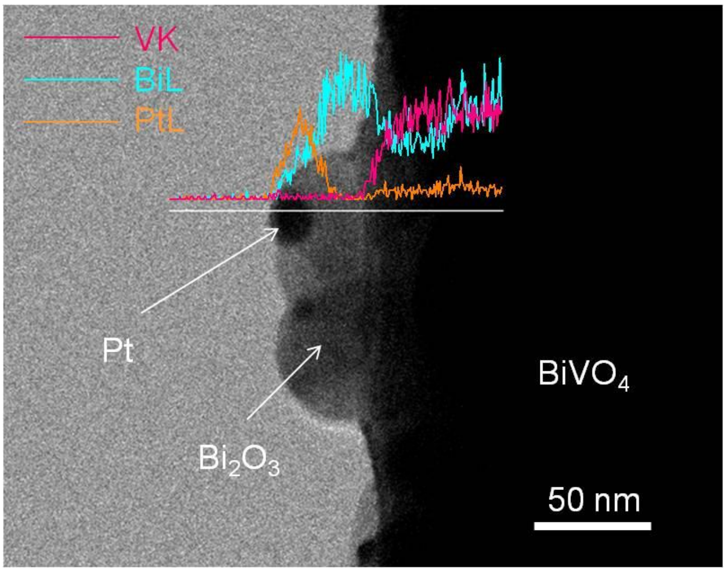

Figure 7.21 STEM image and EDX line scan on one of the *m*-$BiVO_4$/γ-Bi_2O_3/Pt composite nanoparticles.

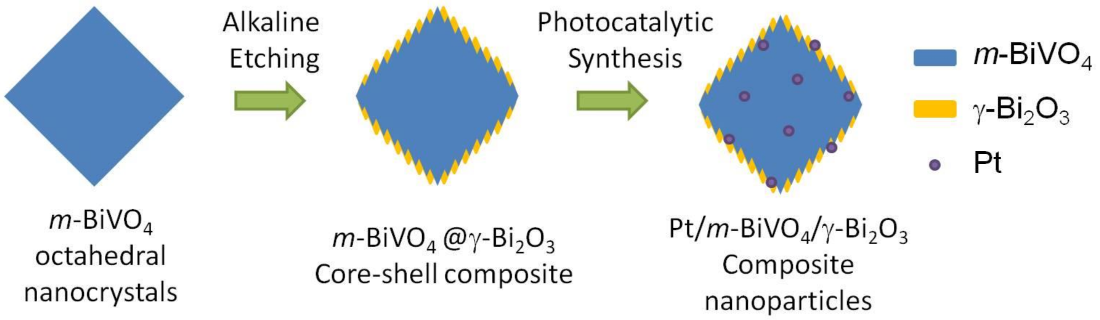

Figure 7.22 Schematic illustration on the synthesis route and the morphology evolution of the *m*-BiVO$_4$/γ-Bi$_2$O$_3$/Pt composite nanoparticles.

After characterization on the composite nanostructure, the visible light photocatalytic activity of these BBPt composite nanoparticles was examined through RhB degradation. The result was compared with BVO and BPt, as plotted in Figure 7.23. Just as expected, BBPt exhibits even faster degradation rate, where the oxidation of RhB could be completed around 4 hours irradiation. Thus, as compared with Pt-modified crystals, the formation of *m*-BiVO$_4$/γ-Bi$_2$O$_3$/Pt composite nanostructure further improved the photocatalytic performance. As discussed in Chapter 6 and 7, both heterogeneous structures, p-n junction formation of *m*-BiVO$_4$@γ-Bi$_2$O$_3$ and surface modification into *m*-BiVO$_4$/Pt, could effectively separate the photogenerated electron-hole pairs, thus improved the photocatalytic performance. Nevertheless, it was also found that too much γ-Bi$_2$O$_3$ phase or noble metal loading would result in significant agglomeration of the composite crystals. Here, by combining the two strategies, the charge separation mechanism could be strengthened through the synergistic effect from multi-heterogeneous nanostructure, while the agglomeration phenomena could be largely avoided. Therefore, the significance of this part of work was not only the further enhancement in photocatalytic performance, but also lies in the successful demonstration of the synergistic strategy, which could guide the materials development for photocatalysis and photoinduced energy conversion applications.

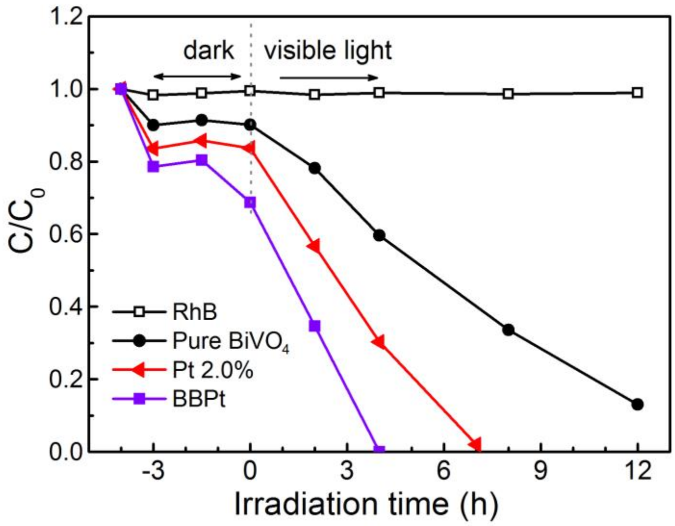

Figure 7.23 The photocatalytic degradation of RhB for as-prepared m-$BiVO_4$/γ-Bi_2O_3/Pt composite nanoparticles.

7.10 Concluding remarks

In summary, metal-oxide heterogeneous nanostructures have been successfully prepared through surface modification of the *m*-$BiVO_4$ octahedral nanocrystals with Au and Pt nanoparticles, respectively, by a simple photochemical reduction method. The experimental results revealed that the *m*-$BiVO_4$ particles maintained monoclinic structures after loading with Au and Pt species. Au and Pt would be reduced into metallic phase and crystallized as nanoparticles on the *m*-$BiVO_4$ crystal surface. Due to the formation of such heterogeneous nanostructure, these Au/- and Pt/*m*-$BiVO_4$ composite nanoparticles exhibited much higher visible-light photocatalytic activities than the pure *m*-$BiVO_4$ crystals. Especially, Pt2.0% resulted in the best photocatalytic performance, and the RhB photodegradation could be completed around 7 hours. Based on the extensive discussion, the enhanced photocatalytic performance was mostly attributed to the effective electron transfer from *m*-$BiVO_4$ to the attached noble metal nanoparticles. In addition, it was also found that Pt/*m*-$BiVO_4$ composite nanoparticles exhibited better photocatalytic performance than the Au-loaded counterparts. And this lied in the better dispersion of Pt nanoparticles than Au species on the surface of *m*-$BiVO_4$ crystals. In the end, a multi-composite sample BBPt with *m*-$BiVO_4$/γ-Bi_2O_3/Pt nanostructure was successfully synthesized by loading Pt nanoparticles on the resultant *m*-$BiVO_4$@γ-Bi_2O_3 composite crystals. The STEM-EDX characterization revealed the location of Pt nanoparticles was mostly on the γ-Bi_2O_3 shell. As expected, the RhB degradation test indicated the further improved photocatalytic performance of these *m*-$BiVO_4$/γ-Bi_2O_3/Pt composite nanoparticles, which could be attributed to the strengthened charge separation promotion through the synergistic effect from the multi-heterogeneous nanostructure.

Chapter 8. Conclusions and future work

8.1 Conclusions

This thesis investigated the synthesis and development of *m*-$BiVO_4$-based materials for photocatalytic applications. Based on the fundamental investigations on the chemical synthesis and photocatalytic mechanisms, novel synthesis method was developed and modified in order to control the particle size as well as crystal morphology and to establish heterogeneous nanostructures towards the improvement in photocatalytic performance.

The present work started from the mechanism investigation in the chemical synthesis of *m*-$BiVO_4$ particles by hydrothermal method. It was found that the $pH \leq 9$ was essential in the formation of *m*-$BiVO_4$ phase. In addition, due to different reaction mechanism involved under various pH values, the state and morphology of Bi-precursor played crucial roles in determining the particle size and morphology of the final *m*-$BiVO_4$ products. With the suitable band gap values, 2.26 ~ 2.40 eV, these as-prepared *m*-$BiVO_4$ powders showed superior photocatalytic performance under visible light irradiation in the degradation of RhB. Furthermore, the degradation efficiency was found to be greatly influenced by both specific surface area and local structure variation of the materials. Among these samples, BVO-0, synthesized in pH = 0.4 aqueous solution, exhibited the highest degradation efficiency. And for BVO-3 and BVO-5, despite larger specific surface area, their shorter V–O bond corresponded to less distortion of the VO_4^{3-} tetrahedron in the local structure, which resulted in lower photocatalytic performance.

After the investigation of pH value effect on $BiVO_4$ structure and morphology control, mono-dispersed *m*-$BiVO_4$ octahedral single crystals have been synthesized in aqueous solution with $pH < 1$, with the addition of SDBS surfactant. These single crystals showed uniform sizes and preferred {120} and {021} crystalline facets with good crystallization. The formation and growth of the octahedral shape was considered to be a typical supersaturation process combined with Ostwald ripening process. The crystal size of *m*-$BiVO_4$ octahedra could be facially adjusted in a broad range from 5 μm to less than 200 nm. Moreover, these octahedral single crystals showed superior high photocatalytic performance in the degradation of RhB under visible light irradiation.

Subsequently, based on the *m*-$BiVO_4$ octahedral single crystals, *m*-$BiVO_4$@γ-Bi_2O_3 composite crystals with core-shell heterostructure have been synthesized under alkaline hydrothermal condition. Such reaction could be considered as a simple “etching” process that the surface V ions of *m*-$BiVO_4$ octahedra dissolve in strong alkaline solution, while the Bi ions precipitate as γ-Bi_2O_3 phase on the *m*-$BiVO_4$ core. It was found that the degree of etching, corresponding to the phase ratio of Bi_2O_3 to $BiVO_4$, was determined by the alkaline concentration and reaction time. In addition, the specific surface area could be increased at the beginning of Bi_2O_3 formation, because the smooth surface of $BiVO_4$ crystals became rough. In the latter reaction, the specific surface area would decrease promptly, which was due to the rapid ripening of Bi_2O_3 phase. Importantly, these composite powders showed superior photocatalytic performance in the degradation of RhB under visible light irradiation. The degradation efficiency of RhB after 10 hours reached 86% for the sample BB03, which was 31% higher than pure *m*-$BiVO_4$ octahedral nanocrystals. Besides the increase in specific surface area, such enhancement could be mostly attributed to the p-n heterojunction structure that can promote the charge carrier transfer and reduce their recombination probability. This was confirmed by the surface photovoltage spectra analysis.

In parallel, metal-oxide heterogeneous nanostructures were also prepared through surface modification of the *m*-$BiVO_4$ octahedral nanocrystals with Au and Pt nanoparticles, respectively. In this part, a simple photochemical reduction method was conducted, by which metallic Au and Pt nanoparticles were successfully synthesized and loaded onto the surface of *m*-$BiVO_4$ nanocrystals, resulting in metal/*m*-$BiVO_4$ heterogeneous nanostructure. As a consequence, the properly loaded Au/- and Pt/*m*-$BiVO_4$ composite nanoparticles exhibited much higher visible-light photocatalytic activities than the pure *m*-$BiVO_4$ crystals. Especially, Pt2.0% resulted in the best photocatalytic performance, and the RhB photodegradation could be almost completed within 7 hours. The possible enhancing mechanisms were extensively discussed. The improved photocatalytic performance in these Au- and Pt-loaded *m*-$BiVO_4$ nanoparticles was mostly attributed to the effective electron transfer from *m*-$BiVO_4$ to the attached noble metal nanoparticles. In addition, the results from Pt/*m*-$BiVO_4$ composite nanoparticles were also compared with those from Au-loaded samples. It was concluded that the superior photocatalytic activity of Pt/*m*-$BiVO_4$ composite nanoparticles lied in the better dispersion of Pt nanoparticles than Au species on the surface of *m*-$BiVO_4$ crystals.

Last but not the least, as a combination of the achievements in the p-n composite formation and Pt nanoparticles loading, *m*-$BiVO_4$/γ-Bi_2O_3/Pt multi-composite nanoparticles (BBPt) were synthesized by loading Pt nanoparticles on the as-prepared *m*-$BiVO_4$/γ-Bi_2O_3 composite crystals. The *m*-$BiVO_4$/γ-Bi_2O_3/Pt heterogeneous nanostructure was evidenced through XRD and STEM-EDX characterization. As expected, these composite nanoparticles exhibited a further improved photocatalytic performance in RhB degradation test, which could be attributed to the strengthened charge separation promotion through the synergistic effect from the multi-heterogeneous nanostructure.

8.2 Recommended future work

The results of the present work have inspired the following interesting future work based on the current material system:

8.2.1 Synthesis-scale-up of *m*-$BiVO_4$ octahedral nano-crystals

Although the hydrothermal method proposed in Chapter 5 for the synthesis of *m*-$BiVO_4$ octahedral single crystals is quite stable and well repeatable, the synthesis production of this method is relatively low, about 0.5 g product each time. Meanwhile, the increase in precursor concentration would give rise to difficulty in the crystal size control. Nevertheless, due to the high pressure reaction involved, large autoclaves always require intricate design and are seldom used. Thus, the hydrothermal synthesis cannot be simply scaled up. At this point, we are also seeking for other approaches towards high-yield synthesis for practical application, while trying to maintain the octahedral morphology with small particle size.

A modified synthesis was conducted in normal glass beaker in open system by using a temperature controlled hot plate magnetic stirrer instead of a hydrothermal autoclave. Figure 8.1 (a) gives the schematic illustration of the reaction setup. In such open system, large volume synthesis was feasible by simply choosing large beaker size. The raw materials could be multiplied while maintaining the same precursor concentration as those in the hydrothermal method. In a typical scale-up synthesis, 10 mmol reagents were prepared in 350 ml solution, and around 4 g *m*-$BiVO_4$

nanocrystals could be obtained in the final product from a single pot. The production was nearly 10 times of the hydrothermal route.

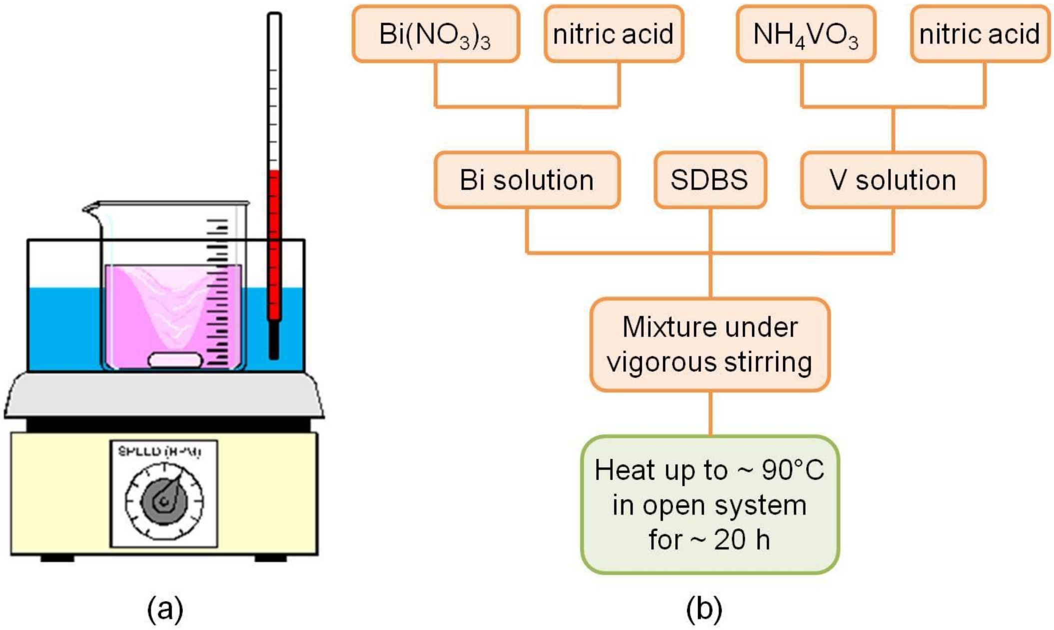

Figure 8.1 Schematic illustration of (a) the setup and (b) the procedure of the scale-up synthesis of *m*-$BiVO_4$ octahedral nanocrystals.

The XRD result in Figure 8.2 clearly indicated that the resultant powders were still composed of monoclinic phase with good crystallization. Moreover, these *m*-$BiVO_4$ nanocrystals preserved the octahedral morphology, as indicated in the SEM image in Figure 8.3. The crystal size of these *m*-$BiVO_4$ nanocrystals were found in the range from 50 nm to 500 nm. As discussed in Chapter 5, these well crystallized nanoparticles crystals could exhibit high specific surface area, which ensures the superior photocatalytic performance. By comparison of the particle size distribution, as shown in Figure 8.4, it was noticed that these octahedral particles through scale-up synthesis were not as uniform as the product from hydrothermal route. By hydrothermal synthesis, the crystal size could be well controlled around 500 nm. On the contrary, in the final product of a scale-up fabrication, a great amount of small crystal seeds, about 60 nm, were preserved among the larger crystals around 330 nm.

Actually, although large amount of powders could be obtained after a 20-hours open-system synthesis, the reaction was not fully completed. This could be evidenced from the colorful solution after liquid-solid separation that some reagents were still remained. It was thus deducted that when the synthesis was stopped, some small crystals were just nucleated and had not experienced extensive crystal growth.

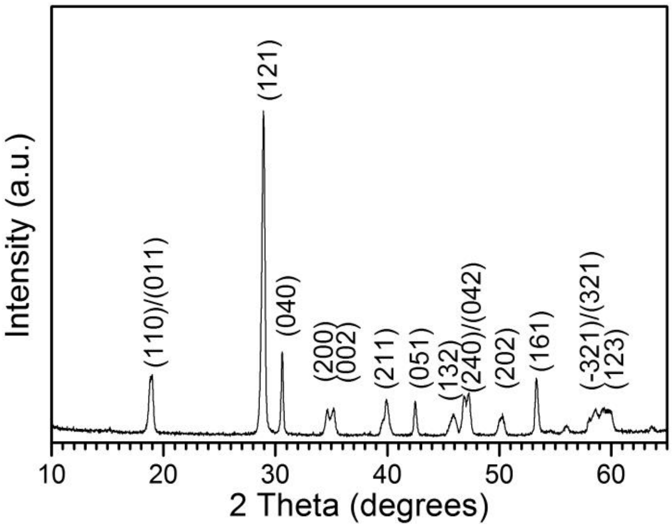

Figure 8.2 XRD pattern of as-prepared *m*-$BiVO_4$ nanoparticles by the scale-up open system synthesis.

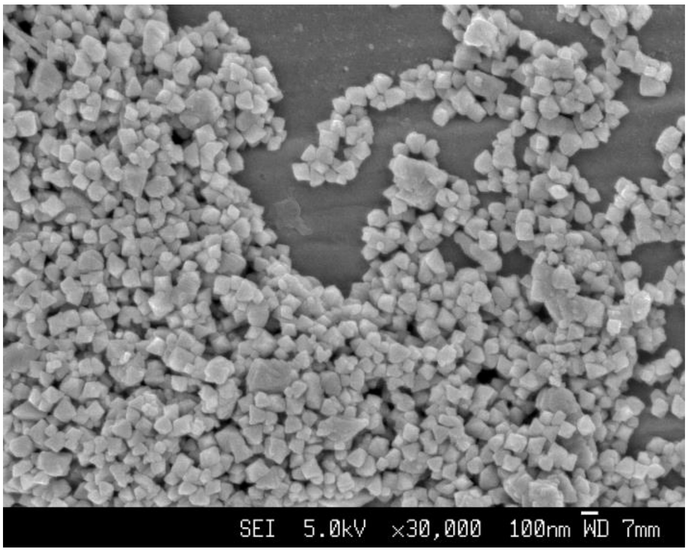

Figure 8.3 Typical SEM image of as-prepared *m*-$BiVO_4$ octahedral nanocrystals by the scale-up open system synthesis.

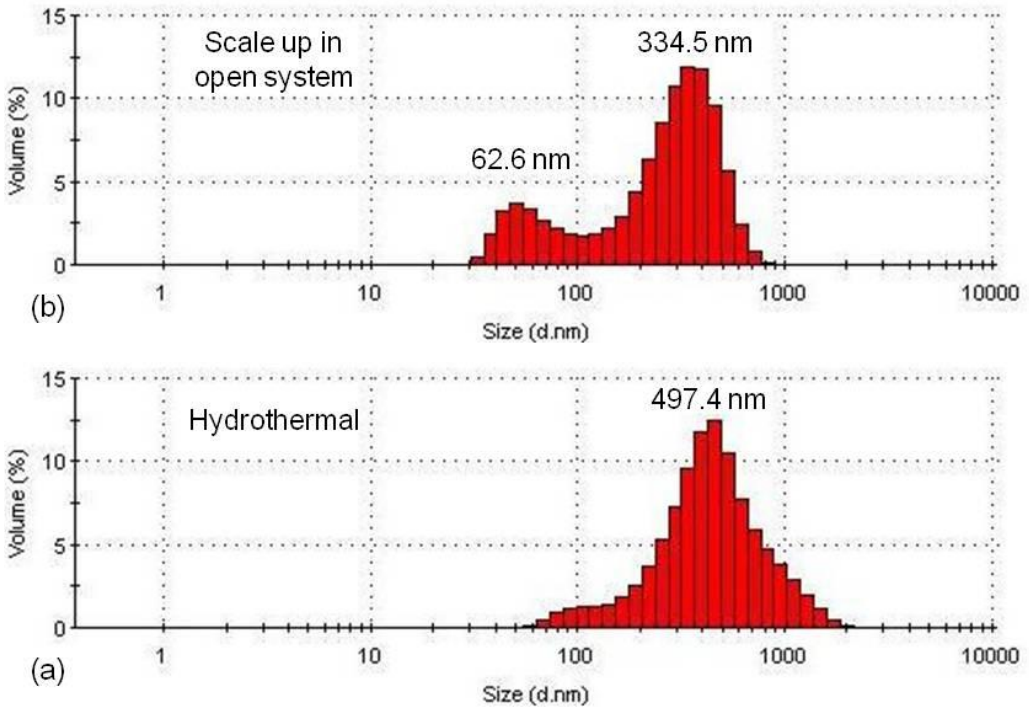

Figure 8.4 Comparison of particle size distribution of *m*-BiVO$_4$ nanocrystals between (a) hydrothermal synthesis and (b) scale-up in open-system.

The main differences between hydrothermal synthesis and the open system route are the pressure and temperature during the reaction, which leads to different influences on phase formation and crystal growth control. In our work, the phase formation of *m*-BiVO$_4$ could be considered as a co-precipitation process from homogeneous solution. According to our experiment, if the open-system synthesis were conducted at room temperature or with heating lower than 80 °C, hardly any precipitates could be collected from the transparent solution. Thus, the heating above 90 °C was required for the *m*-BiVO$_4$ phase formation. However, compared to open-system synthesis, the high temperature above boiling point and high pressure environment in hydrothermal route were not necessary. Instead, they could contribute to higher reaction rate and benefit fast nucleation and sufficient crystal growth. Therefore, in a hydrothermal synthesis, most reaction could be completed within 20 hours and homogeneous crystal size could be achieved, whereas the open-system fabrication requires longer reaction duration.

8.2.2 Preliminary development of *m*-$BiVO_4$ film

As we know, photocatalytic nanopowders always face the great challenge in the particle recycling in practical utilization. The separation and post-recovery of such tiny particles from the large volume of water solution involve further processing and expense. On the other hand, the developments in thin film growth techniques enable us to fabricate high quality thin films in recycled photocatalytic application, and this thin film facilitates the various surface and photoelectrochemical analysis, which can provide detailed experimental data as well as further insight on the mechanism. Recent *m*-$BiVO_4$ thin films have been fabricated through electrochemical synthesis [155], spin-coating [156], dip-coating [157], combustion synthesis [158] etc. However, these approaches require high temperature annealing, around 400~500 °C, which may not be suitable for pre-deposition processing in device fabrication. Hence based on our successful synthesis of nanocrystals, we are trying to develop a fabrication technique for *m*-$BiVO_4$ thin films by using hydrothermal assisted chemical bath deposition. Dense and well crystallized *m*-$BiVO_4$ thin films could be achieved at low temperature fabrication, around 150 °C. Some preliminary results on the *m*-$BiVO_4$ thin films were discussed.

A hydrothermal chemical bath deposition method has been developed to prepare *m*-$BiVO_4$ thin films on Fluorine doped Tin Oxide (FTO) glass substrate. As indicated in Figure 8.5, separately prepared bismuth and vanadate solutions were mixed and transferred into an autoclave. Then a piece of FTO substrate, cleaned and sonicated in ethanol and rinsed with DI water, was loaded in the autoclave before sealing and heating. After the hydrothermal reaction, the film sample was washed with DI water followed by drying in air.

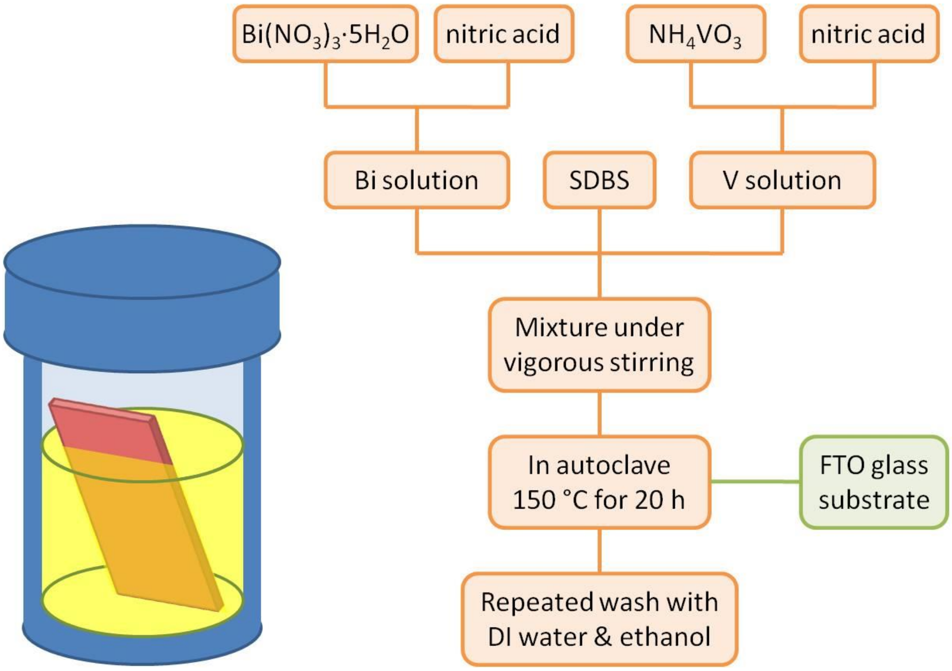

Figure 8.5 Schematic illustration and procedure of *m*-BVO$_4$ film preparation by hydrothermal chemical bath deposition.

The XRD pattern of the as-prepared thin film is shown in Figure 8.6. All diffraction peaks could be indexed with *m*-BiVO$_4$ phase and the cubic structure of FTO. Thus, the XRD pattern clearly indicated the good crystallization of *m*-BiVO$_4$ phase as well as the absence of other impurity phases. It was also observed that the diffraction peaks of (020), (040), (060) and (080) exhibited higher intensity than those indicated in JCPDC card (No. 14-0688). Especially, the peak intensity of (040) has exceeded the doublet (-121) and (121), although the latter corresponds to the strongest peak for randomly oriented polycrystals. Therefore, the XRD pattern indicated the preferred orientation of the *m*-BiVO$_4$ thin film in [010] direction.

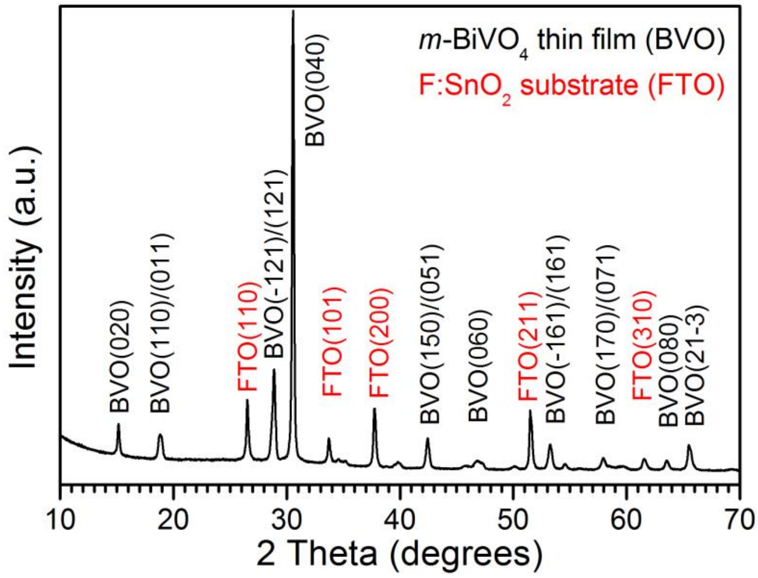

Figure 8.6 XRD pattern of *m*-BVO$_4$ thin film on FTO substrate.

Typical SEM images of the as-prepared *m*-BiVO$_4$ film are shown in Figure 8.7. It could be clearly seen that all surface of the FTO substrate has been covered by dense and homogeneous *m*-BiVO$_4$ film. Moreover, the octahedral morphology could also be preserved in the *m*-BiVO$_4$ film with one of the corners normal to the substrate surface. This was consistent with the preferred orientation in XRD pattern and the octahedral characterization in Chapter 5 that the octahedral corner pointed to the [010] direction.

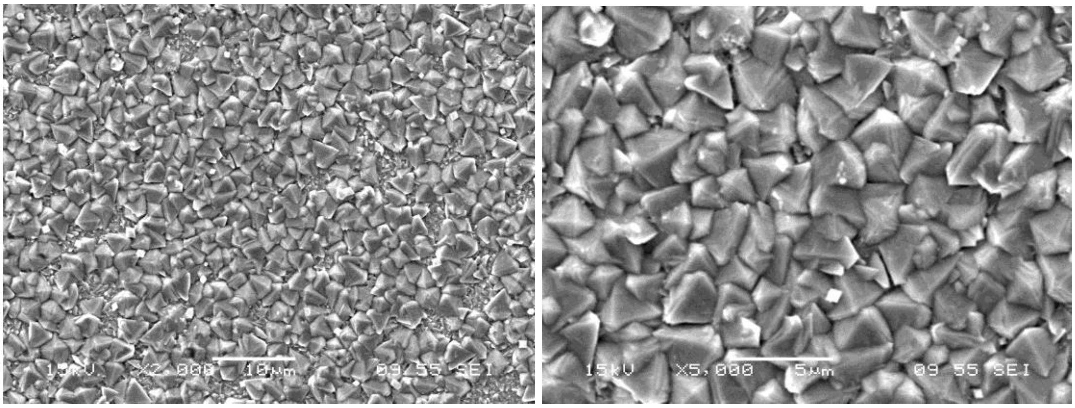

(a) (b)

Figure 8.7 (a) low and (b) high magnification SEM images of *m*-BVO$_4$ thin film on FTO substrate.

The flat band potential of a semiconductor is a very important thermodynamic parameter in the interfacial electron transfer steps occurring in a photocatalytic reaction. For a n-type semiconductor, it can be assumed that the position of the flat band potential is very close to the bottom of the conduction band, and normally can be considered to be located just under the conduction band [159]. Hence, the investigation on flat band potential provides accurate assessment of the band structure, and thus further insight on the redox capability in photocatalytic application. Generally, the flat band potential can be estimated by Mott-Schottky method through the electrochemical analysis [160,161]. Meanwhile, thin film format of a semiconductor on conductive substrate offers the easy access to electrochemical investigation. In this part of work, electrochemical impedance spectroscopy (EIS) measurements were performed on the *m*-$BiVO_4$ thin film and the resultant Mott-Schottky (MS) plots are given in Figure 8.8. Firstly, the positive slope of MS plots from the as-prepared *m*-$BiVO_4$ film is consistent with the n-type conduction behavior. Secondly, the estimated flat band potential is around –0.7 V vs Ag/AgCl (–0.49 V vs NHE), which is consistent with the reported *m*-$BiVO_4$ electrodes [126,159]. The preliminary work here provides the useful experimental information on band structure. This was of great significance because in realistic conditions the surface band structure would be much different from ideal bulk material, due to the presence of nanostructures, interfaces, and impurities etc. Nevertheless, the present work should be followed up by more experimental investigations, especially in combination with other spectral and photoelectrochemical techniques, in order to achieve further insight on the thermodynamic and kinetic mechanisms in photocatalysis process.

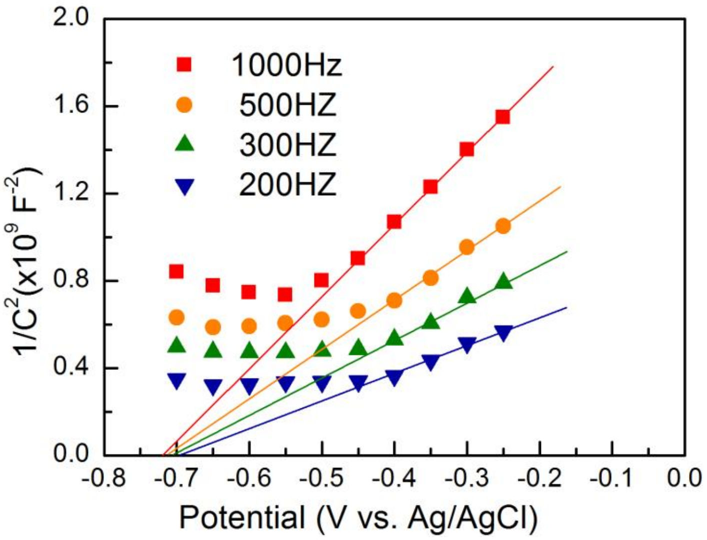

Figure 8.8 Mott-Schottky plots of the *m*-BVO$_4$ thin film recorded at different frequencies.

Moreover, compared to nanoparticles, film may differ a lot in particle size, morphology, interactions and stability, a dense thin film provides a better platform to conduct spectral, electrical and photoelectrochemical characterizations. Thus, based on *m*-BiVO$_4$ thin films, more experimental analysis could be performed in the investigation of band structure, surface states, charge carrier transport behaviors, etc. These experimental information and possible discovery are essential to reveal the underlying mechanisms, and are beneficial to the further development of both film and powder photocatalysts.

The *m*-BiVO$_4$ thin films can also be further explored by morphology control in order to increase the specific surface area. Recently, TiO$_2$ nano-arrays have been successfully prepared by hydrothermal method. The specific surface area is very high, which could significantly contribute to the improved photocatalytic and photoelectric performance [162]. This could be an interesting direction in the development of *m*-BiVO$_4$ thin films in photocatalytic applications.

8.2.3 Magnetization of *m*-$BiVO_4$ octahedral nanocrystals for recycling

Generally, photocatalytic nanoparticles can be employed in the suspended state in liquids in the water treatment and purification. However, the difficulty in nanoparticles cycling will significantly increase the cost in realistic processing. The ease of powder recovery could be achieved by synthesizing the photocatalytic materials as functional shell on magnetic core materials. With regards to this issue, many core-shell structures have been synthesized, such as Fe_3O_4/TiO_2, $BiFeO_3/TiO_2$, $ZnFe_2O_4/TiO_2$ and $MnFe_2O_4/TiO_2$ [123,163-165]. For *m*-$BiVO_4$ materials, synthesis developments of magnetic core-shell nanocrystals will be of great interest towards the practical water treatment application.

8.2.4 Other morphologies of *m*-$BiVO_4$ nanoparticles

Mono-dispersed *m*-$BiVO_4$ octahedral single crystals have been successfully obtained by hydrothermal method with the addition of SDBS surfactant, which was proven to be a novel and effective morphology for the enhancement of photocatalytic performance. Meanwhile, some other morphologies, such as nanowires, nanoporous, hollow spheres, etc, benefit a high specific surface area, thus further improvement in the photocatalytic activity. In recent studies, synthesis of *m*-$BiVO_4$ hollow spheres, rod-like, tubular [116] have been reported. Further reducing the micron sized crystals into nanometer grade is promising for even higher photocatalytic performance. On the other hand, the pursuit of small particle size should not be achieved at the expense of crystallization. If nanoparticles are prepared with poor crystallization or amorphous outer layer, the electronic band structure can be affected and the photo-generation of the electron-hole pairs can be greatly influenced. In addition, the impurity sites can act as the recombination centers that significantly reduce the photocatalytic property [166-

169]. Therefore, contributions from crystal morphology, particle size and crystallization have to be well balanced in the design and development of synthesis methods in *m*-$BiVO_4$ and other photocatalytic materials.

Publication List

Journal Papers:

1. **M. D. Han**, T. Sun, X. F. Chen, O. K. Tan and M. S. Tse, Morphology Control of Hydrothermal Synthesized $BiVO_4$ Particles with Enhanced Photocatalytic Performance. *J. Nanoeng. Nanomanuf.* **4**, 146-152 (2014)
2. **M. D. Han**, T. Sun, P. Y. Tan, X. F. Chen, O. K. Tan and M. S. Tse, *m*-$BiVO_4$@γ-Bi_2O_3 core-shell p-n heterogeneous nanostructure for enhanced visible-light photocatalytic performance. *RSC Adv.* **3**, 24964-24970 (2013).
3. **M. D. Han**, X. F. Chen, T. Sun, O. K. Tan and M. S. Tse, Synthesis of mono-dispersed *m*-$BiVO_4$ octahedral nano-crystals and enhanced visible light photocatalytic properties. *CrystEngComm*. **13**, 6674-6679 (2011).

International Conferences:

1. **M. D. Han**, X. F. Chen, T. Sun, O. K. Tan and M. S. Tse, Synthesis and modification of *m*-$BiVO_4$ nano-crystals with enhanced photocatalytic performance. 19th International Conference on the Conversion and Storage of Solar Energy (IPS-19), Pasadena, CA, USA, 29 Jul-03 Aug 2012.
2. **M. D. Han**, X. F. Chen, T. Sun, Q. Luo, O. K. Tan and M. S. Tse, Synthesis and Size Control of *m*-$BiVO_4$ nano crystals with Enhanced Photocatalytic Performance. 5th MRS-S Conference on Advanced Materials, Singapore, 20-22 Mar 2012.
3. **M. D. Han**, T. Sun, X. F. Chen, O. K. Tan and M. S. Tse, pH-directed morphology control and photocatalytic performance of hydrothermal synthesized $BiVO_4$. International Conference on Materials for Advanced Technologies (ICMAT 2011), Symposium JJ, Singapore, 26 Jun-01 Jul 2011 (oral).

References

[1] A. Fujishima and K. Honda, "Electrochemical photolysis of water at a semiconductor electrode" *Nature* **238**, 37 (1972).

[2] Akira Fujishima, Xintong Zhang, and Donald A. Tryk, "TiO_2 photocatalysis and related surface phenomena" *Surf. Sci. Rep.* **63**, 515 (2008).

[3] R. Asahi, T. Morikawa, T. Ohwaki, K. Aoki, and Y. Taga, "Visible-light photocatalysis in nitrogen-doped titanium oxides" *Science* **293**, 269 (2001).

[4] S. U. M. Khan, M. Al-Shahry, and W. B. Ingler, "Efficient photochemical water splitting by a chemically modified n-TiO_2" *Science* **297**, 2243 (2002).

[5] S. Sakthivel and H. Kisch, "Daylight photocatalysis by carbon-modified titanium dioxide" *Angewandte Chemie-International Edition* **42**, 4908 (2003).

[6] J. C. Yu, G. S. Li, X. C. Wang, X. L. Hu, C. W. Leung, and Z. D. Zhang, "An ordered cubic Im3m mesoporous Cr-TiO_2 visible light photocatalyst" *Chem. Commun.*, 2717 (2006).

[7] S. Klosek and D. Raftery, "Visible light driven V-doped TiO_2 photocatalyst and its photooxidation of ethanol" *J. Phys. Chem. B* **105**, 2815 (2001).

[8] Q. R. Deng, X. H. Xia, M. L. Guo, Y. Gao, and G. Shao, "Mn-doped TiO_2 nanopowders with remarkable visible light photocatalytic activity" *Mater. Lett.* **65**, 2051 (2011).

[9] Y. Liu, J. H. Wei, R. Xiong, C. X. Pan, and J. Shi, "Enhanced visible light photocatalytic properties of Fe-doped TiO_2 nanorod clusters and monodispersed nanoparticles" *Appl. Surf. Sci.* **257**, 8121 (2011).

[10] Akihiko Kudo and Yugo Miseki, "Heterogeneous photocatalyst materials for water splitting" *Chem. Soc. Rev.* **38**, 253 (2009).

[11] Guangcheng Xi and Jinhua Ye, "Synthesis of bismuth vanadate nanoplates with exposed {001} facets and enhanced visible-light photocatalytic properties" *Chem. Commun.* **46**, 1893 (2010).

[12] Donge Wang, Hongfu Jiang, Xu Zong, Qian Xu, Yi Ma, Guoling Li, and Can Li, "Crystal Facet Dependence of Water Oxidation on $BiVO_4$ Sheets under Visible Light Irradiation" *Chem. Eur. J.* **17**, 1275 (2011).

[13] Zhiqiang Wang, Wenjun Luo, Shicheng Yan, Jianyong Feng, Zongyan Zhao, Yisi Zhu, Zhaosheng Li, and Zhigang Zou, "$BiVO_4$ nano-leaves: Mild synthesis and improved photocatalytic activity for O_2 production under visible light irradiation" *CrystEngComm* **13**, 2500 (2011).

[14] F. Seker, K. Meeker, T. F. Kuech, and A. B. Ellis, "Surface chemistry of prototypical bulk II-VI and III-V semiconductors and implications for chemical sensing" *Chem. Rev.* **100**, 2505 (2000).

[15] J. Yu and A. Kudo, "Effects of Structural Variation on the Photocatalytic Performance of Hydrothermally Synthesized $BiVO_4$" *Adv. Funct. Mater.* **16**, 2163 (2006).

[16] A. Mills and S. LeHunte, "An overview of semiconductor photocatalysis" *Journal of Photochemistry and Photobiology a-Chemistry* **108**, 1 (1997).

[17] M. Anpo, T. Shima, S. Kodama, and Y. Kubokawa, "Photocatalytic hydrogenation of CH_3CCH with H_2O on small-particle TiO_2 - size quantization effects and reaction intermediates" *J. Phys. Chem.* **91**, 4305 (1987).

[18] G. Mills and M. R. Hoffmann, "Photocatalytic degradation of pentachlorophenol on TiO_2 particles - identification of intermediates and mechanism of reaction" *Environmental Science & Technology* **27**, 1681 (1993).

[19] Y. Ohko, K. Hashimoto, and A. Fujishima, "Kinetics of photocatalytic reactions under extremely low-intensity UV illumination on titanium dioxide thin films" *J. Phys. Chem. A* **101**, 8057 (1997).

[20] C. Minero, G. Mariella, V. Maurino, and E. Pelizzetti, "Photocatalytic transformation of organic compounds in the presence of inorganic anions. 1. Hydroxyl-mediated and direct electron-transfer reactions of phenol on a titanium dioxide-fluoride system" *Langmuir* **16**, 2632 (2000).

[21] C. Minero, G. Mariella, V. Maurino, D. Vione, and E. Pelizzetti, "Photocatalytic transformation of organic compounds in the presence of inorganic ions. 2. Competitive reactions of phenol and alcohols an a titanium dioxide-fluoride system" *Langmuir* **16**, 8964 (2000).

[22] A. L. Linsebigler, G. Q. Lu, and J. T. Yates, "Photocatalysis on TiO_2 surfaces - principles, mechanisms, and selected results" *Chem. Rev.* **95**, 735 (1995).

[23] O. Legrini, E. Oliveros, and A. M. Braun, "Photochemical processes for water-treatment" *Chem. Rev.* **93**, 671 (1993).

[24] R. M. Alberici and W. E. Jardim, "Photocatalytic destruction of VOCs in the gas-phase using titanium dioxide" *Applied Catalysis B-Environmental* **14**, 55 (1997).

[25] S. B. Kim, H. T. Hwang, and S. C. Hong, "Photocatalytic degradation of volatile organic compounds at the gas-solid interface of a TiO_2 photocatalyst" *Chemosphere* **48**, 437 (2002).

[26] C. Belver, R. Bellod, S. J. Stewart, F. G. Requejo, and M. Fernandez-Garcia, "Nitrogen-containing TiO_2 photocatalysts - Part 2. Photocatalytic behavior under sunlight excitation" *Applied Catalysis B-Environmental* **65**, 309 (2006).

[27] D. Vildozo, C. Ferronato, M. Sleiman, and J. M. Chovelon, "Photocatalytic treatment of indoor air: Optimization of 2-propanol removal using a response surface methodology (RSM)" *Applied Catalysis B-Environmental* **94**, 303 (2010).

[28] C. Karunakaran, A. Vijayabalan, G. Manikandan, and P. Gomathisankar, "Visible light photocatalytic disinfection of bacteria by Cd-TiO_2" *Catal. Commun.* **12**, 826 (2011).

[29] C. Pablos, R. van Grieken, J. Marugan, and B. Moreno, "Photocatalytic inactivation of bacteria in a fixed-bed reactor: Mechanistic insights by epifluorescence microscopy" *Catal. Today* **161**, 133 (2011).

[30] W. P. Sung, T. T. Tsai, M. J. Wu, H. J. Wang, and R. Y. Surampalli, "Removal of Indoor Airborne Bacteria by Nano-Ag/TiO_2 as Photocatalyst: Feasibility Study in Museum and Nursing Institutions" *Journal of Environmental Engineering-Asce* **137**, 163 (2011).

[31] C. Renz, "Light reactions of the oxides of titanium, cerium and earth acids" *Helv. Chim. Acta* **4**, 961 (1921).

[32] E. Baur and A. Perret, "On the action of light on dissolved silver salts in the presence of zinc oxide" *Helv. Chim. Acta* **7**, 910 (1924).

[33] E. Baur and C. Neuweiler, "On the photolytic formation of hydroperoxide" *Helv. Chim. Acta* **10**, 901 (1927).

[34] C. Renz, "The effects of silver nitrate oxides and gold chloride oxides in light" *Helv. Chim. Acta* **15**, 1077 (1932).

[35] C. F. Goodeve and J. A. Kitchener, "Photosensitisation by titanium dioxide" *Transactions of the Faraday Society* **34**, 0570 (1938).

[36] M. C. Markham, M. C. Hannan, R. M. Paternostro, and C. B. Rose, "Oxidation of alcohols catalyzed by zinc oxide and light" *J. Am. Chem. Soc.* **80**, 5394 (1958).

[37] M. C. Markham, M. C. Hannan, and S. W. Evans, "Factors influencing the oxidation of phenols, catalyzed by zinc oxide and light" *J. Am. Chem. Soc.* **76**, 820 (1954).

[38] M. C. Markham and K. J. Laidler, "A kinetic study of photo-oxidations on the surface of zinc oxide in aqueous suspensions" *J. Phys. Chem.* **57**, 363 (1953).

[39] D. R. Kennedy, M. Ritchie, and J. Mackenzie, "The photosorption of oxygen and nitric oxide on titanium dioxide" *Transactions of the Faraday Society* **54**, 119 (1958).

[40] U. Diebold, "The surface science of titanium dioxide" *Surf. Sci. Rep.* **48**, 53 (2003).

[41] M. R. Ranade, A. Navrotsky, H. Z. Zhang, J. F. Banfield, S. H. Elder, A. Zaban, P. H. Borse, S. K. Kulkarni, G. S. Doran, and H. J. Whitfield, "Energetics of nanocrystalline TiO_2" *Proc. Nat. Acad. Sci. U.S.A.* **99**, 6476 (2002).

[42] J. Arbiol, J. Cerda, G. Dezanneau, A. Cirera, F. Peiro, A. Cornet, and J. R. Morante, "Effects of Nb doping on the TiO_2 anatase-to-rutile phase transition" *J. Appl. Phys.* **92**, 853 (2002).

[43] W. W. So, S. B. Park, K. J. Kim, C. H. Shin, and S. J. Moon, "The crystalline phase stability of titania particles prepared at room temperature by the sol-gel method" *J. Mater. Sci.* **36**, 4299 (2001).

[44] J. A. Gamboa and D. M. Pasquevich, "Effect of chlorine atmosphere on the anatase rutile transformation" *J. Am. Ceram. Soc.* **75**, 2934 (1992).

[45] G. Riegel and J. R. Bolton, "Photocatalytic efficiency variability in TiO_2 particles" *J. Phys. Chem.* **99**, 4215 (1995).

[46] R. I. Bickley, T. Gonzalezcarreno, J. S. Lees, L. Palmisano, and R. J. D. Tilley, "A structural investigation of Titanium-dioxide photocatalysts" *J. Solid State Chem.* **92**, 178 (1991).

[47] Catherine B. Almquist and Pratim Biswas, "Role of Synthesis Method and Particle Size of Nanostructured TiO_2 on Its Photoactivity" *J. Catal.* **212**, 145 (2002).

[48] C. Hariharan, "Photocatalytic degradation of organic contaminants in water by ZnO nanoparticles: Revisited" *Appl. Catal. A-Gen.* **304**, 55 (2006).

[49] H. Zhang, R. L. Zong, and Y. F. Zhu, "Photocorrosion Inhibition and Photoactivity Enhancement for Zinc Oxide via Hybridization with Monolayer Polyaniline" *J. Phys. Chem. C* **113**, 4605 (2009).

[50] Michio Matsumura, Yukinari Saho, and Hiroshi Tsubomura, "Photocatalytic hydrogen production from solutions of sulfite using platinized cadmium sulfide powder" *J. Phys. Chem.* **87**, 3807 (1983).

[51] M. A. Pena and J. L. G. Fierro, "Chemical structures and performance of perovskite oxides" *Chem. Rev.* **101**, 1981 (2001).

[52] T. R. N. Kutty and M. Avudaithai, "Photocatalysis on fine powders of perovskite oxides" in *Properties and applications of perovskite-type oxides*, edited by L.G. Tejuca and J.L.G. Fierro (Dekker, New York, 1993), p. 307.

[53] V. A. Trepakov, Z. Potucek, M. V. Makarova, A. Dejneka, P. Sazama, L. Jastrabik, and Z. Bryknar, "$SrTiO_3$: Cr nanocrystalline powders: size effects and optical properties" *J. Phys. Condens. Matter* **21**, 375303 (2009).

[54] Jean Marie Herrmann, Marie Noëlle Mozzanega, and Pierre Pichat, "Oxidation of oxalic acid in aqueous suspensions of semiconductors illuminated with UV or visible light" *J. Photochem.* **22**, 333 (1983).

[55] H. Y. Chen, A. Nambu, W. Wen, J. Graciani, Z. Zhong, J. C. Hanson, E. Fujita, and J. A. Rodriguez, "Reaction of NH_3 with titania: N-doping of the oxide and TiN formation" *J. Phys. Chem. C* **111**, 1366 (2007).

[56] M. Miyauchi, A. Nakajima, K. Hashimoto, and T. Watanabe, "A highly hydrophilic thin film under 1 $\mu W/cm^2$ UV illumination" *Adv. Mater.* **12**, 1923 (2000).

[57] I. Nakamura, N. Negishi, S. Kutsuna, T. Ihara, S. Sugihara, and E. Takeuchi, "Role of oxygen vacancy in the plasma-treated TiO_2 photocatalyst with visible light activity for NO removal" *J. Mol. Catal. A-Chem.* **161**, 205 (2000).

[58] S. Livraghi, M. C. Paganini, E. Giamello, A. Selloni, C. Di Valentin, and G. Pacchioni, "Origin of photoactivity of nitrogen-doped titanium dioxide under visible light" *J. Am. Chem. Soc.* **128**, 15666 (2006).

[59] N. Serpone, "Is the band gap of pristine TiO_2 narrowed by anion- and cation-doping of titanium dioxide in second-generation photocatalysts?" *J. Phys. Chem. B* **110**, 24287 (2006).

[60] H. Irie, Y. Watanabe, and K. Hashimoto, "Nitrogen-concentration dependence on photocatalytic activity of $TiO_{2-x}N_x$ powders" *J. Phys. Chem. B* **107**, 5483 (2003).

[61] H. Irie, Y. Watanabe, and K. Hashimoto, "Carbon-doped anatase TiO_2 powders as a visible-light sensitive photocatalyst" *Chem. Lett.* **32**, 772 (2003).

[62] X. B. Chen, L. Liu, P. Y. Yu, and S. S. Mao, "Increasing Solar Absorption for Photocatalysis with Black Hydrogenated Titanium Dioxide Nanocrystals" *Science* **331**, 746 (2011).

[63] Z. G. Zou, J. H. Ye, K. Sayama, and H. Arakawa, "Direct splitting of water under visible light irradiation with an oxide semiconductor photocatalyst" *Nature* **414**, 625 (2001).

[64] F. X. Wang, M. W. Shao, L. Cheng, J. Hua, and X. W. Wei, "The synthesis of monoclinic bismuth vanadate nanoribbons and studies of photoconductive, photoresponse, and photocatalytic properties" *Mater. Res. Bull.* **44**, 1687 (2009).

[65] M. Hara, G. Hitoki, T. Takata, J. N. Kondo, H. Kobayashi, and K. Domen, "TaON and Ta_3N_5 as new visible light driven photocatalysts" *Catal. Today* **78**, 555 (2003).

[66] Akihiko Kudo, Keiko Omori, and Hideki Kato, "A Novel Aqueous Process for Preparation of Crystal Form-Controlled and Highly Crystalline $BiVO_4$ Powder from Layered Vanadates at Room Temperature and Its Photocatalytic and Photophysical Properties" *J. Am. Chem. Soc.* **121**, 11459 (1999).

[67] Xianluo Hu, Guisheng Li, and Jimmy C. Yu, "Design, Fabrication, and Modification of Nanostructured Semiconductor Materials for Environmental and Energy Applications" *Langmuir* **26**, 3031 (2009).

[68] Saimi Tokunaga, Hideki Kato, and Akihiko Kudo, "Selective Preparation of Monoclinic and Tetragonal $BiVO_4$ with Scheelite Structure and Their Photocatalytic Properties" *Chem. Mater.* **13**, 4624 (2001).

[69] Guisheng Li, Dieqing Zhang, and Jimmy C. Yu, "Ordered Mesoporous $BiVO_4$ through Nanocasting: A Superior Visible Light-Driven Photocatalyst" *Chem. Mater.* **20**, 3983 (2008).

[70] L. Ren, L. Jin, J. B. Wang, F. Yang, M. Q. Qiu, and Y. Yu, "Template-free synthesis of $BiVO_4$ nanostructures: I. Nanotubes with hexagonal cross sections by oriented attachment and their photocatalytic property for water splitting under visible light" *Nanotechnology* **20** (2009).

[71] A. W. Sleight, H. y Chen, A. Ferretti, and D. E. Cox, "Crystal growth and structure of $BiVO_4$" *Mater. Res. Bull.* **14**, 1571 (1979).

[72] A. R. Lim, S. H. Choh, and M. S. Jang, "Prominent ferroelastic domain-walls in $BiVO_4$ crystal" *J. Phys. Condens. Matter* **7**, 7309 (1995).

[73] Xi Zhang, Zhihui Ai, Falong Jia, Lizhi Zhang, Xiaoxing Fan, and Zhigang Zou, "Selective synthesis and visible-light photocatalytic activities of $BiVO_4$ with different crystalline phases" *Mater. Chem. Phys.* **103**, 162 (2007).

[74] Jianqiang Yu and Akihiko Kudo, "Hydrothermal Synthesis of Nanofibrous Bismuth Vanadate" *Chem. Lett.* **34**, 850 (2005).

[75] Li Zhang, Dairong Chen, and Xiuling Jiao, "Monoclinic Structured $BiVO_4$ Nanosheets:Hydrothermal Preparation, Formation Mechanism, and Coloristic and Photocatalytic Properties" *J. Phys. Chem. B* **110**, 2668 (2006).

[76] M. C. Neves and T. Trindade, "Chemical bath deposition of $BiVO_4$" *Thin Solid Films* **406**, 93 (2002).

[77] Lin Zhou, Wenzhong Wang, Shengwei Liu, Lisha Zhang, Haolan Xu, and Wei Zhu, "A sonochemical route to visible-light-driven high-activity $BiVO_4$ photocatalyst" *J. Mol. Catal. A: Chem.* **252**, 120 (2006).

[78] Lin Zhou, Wenzhong Wang, Lisha Zhang, Haolan Xu, and Wei Zhu, "Single-Crystalline $BiVO_4$ Microtubes with Square Cross-Sections: Microstructure, Growth Mechanism, and Photocatalytic Property" *J. Phys. Chem. C* **111**, 13659 (2007).

[79] Lin Zhou, Wenzhong Wang, and Haolan Xu, "Controllable Synthesis of Three-Dimensional Well-Defined $BiVO_4$ Mesocrystals via a Facile Additive-Free Aqueous Strategy" *Cryst. Growth Des.* **8**, 728 (2008).

[80] Wenzong Yin, Wenzhong Wang, Lin Zhou, Songmei Sun, and Ling Zhang, "CTAB-assisted synthesis of monoclinic $BiVO_4$ photocatalyst and its highly efficient degradation of organic dye under visible-light irradiation" *J. Hazard. Mater.* **173**, 194 (2010).

[81] Gang Liu, Lianzhou Wang, Hua Gui Yang, Hui-Ming Cheng, and Gao Qing Lu, "Titania-based photocatalysts-crystal growth, doping and heterostructuring" *J. Mater. Chem.* **20**, 831 (2010).

[82] V. Tjoa, J. Chua, S. S. Pramana, J. Wei, S. G. Mhaisalkar, and N. Mathews, "Facile Photochemical Synthesis of Graphene-Pt Nanoparticle Composite for Counter Electrode in Dye Sensitized Solar Cell" *Acs Applied Materials & Interfaces* **4**, 3447 (2012).

[83] Frank E. Osterloh, "Inorganic Materials as Catalysts for Photochemical Splitting of Water" *Chem. Mater.* **20**, 35 (2007).

[84] J. G. Qu, N. N. Li, B. J. Liu, and J. X. He, "Preparation of $BiVO_4$/bentonite catalysts and their photocatalytic properties under simulated solar irradiation" *Mater. Sci. Semicond. Process.* **16**, 99 (2013).

[85] Y. Hou, F. Zuo, A. Dagg, and P. Y. Feng, "Visible Light-Driven alpha-Fe_2O_3 Nanorod/Graphene/$BiV_{1-x}Mo_xO_4$ Core/Shell Heterojunction Array for Efficient Photoelectrochemical Water Splitting" *Nano Lett.* **12**, 6464 (2012).

[86] X. M. Gao, F. Fu, Y. F. Wu, L. P. Zhang, and W. H. Li, "Preparation of Co-$BiVO_4$ Photocatalyst and Its Application in the Photocatalytic Oxidative Thiophene" *Journal of Inorganic Materials* **27**, 1073 (2012).

[87] N. Wetchakun, S. Chaiwichain, B. Inceesungyorn, K. Pingmuang, S. Phanichphant, A. I. Minett, and J. Chen, "$BiVO_4/CeO_2$ Nanocomposites with High Visible-Light-Induced Photocatalytic Activity" *Acs Applied Materials & Interfaces* **4**, 3718 (2012).

[88] Q. X. Jia, K. Iwashina, and A. Kudo, "Facile fabrication of an efficient $BiVO_4$ thin film electrode for water splitting under visible light irradiation" *Proc. Nat. Acad. Sci. U.S.A.* **109**, 11564 (2012).

[89] K. Hakouk, D. Giaume, P. Barboux, and J. Sablayrolles, "Solution synthesis of $Y_{1-x}Bi_xVO_4$ for optical applications" *J. Lumin.* **132**, 1389 (2012).

[90] Weirong Zhao, Yan Wang, Yong Yang, Jing Tang, and Yanan Yang, "Carbon spheres supported visible-light-driven CuO-$BiVO_4$ heterojunction: Preparation, characterization, and photocatalytic properties" *Applied Catalysis B: Environmental* **115–116**, 90 (2012).

[91] N. Murakami, N. Takebe, T. Tsubota, and T. Ohno, "Improvement of visible light photocatalytic acetaldehyde decomposition of bismuth vanadate/silica nanocomposites by cocatalyst loading" *J. Hazard. Mater.* **211**, 83 (2012).

[92] R. Kontic and G. R. Patzke, "Synthetic trends for $BiVO_4$ photocatalysts: Molybdenum substitution vs. TiO_2 and SnO_2 heterojunctions" *J. Solid State Chem.* **189**, 38 (2012).

[93] L. Lin, Y. C. Yang, L. Men, X. Wang, D. N. He, Y. C. Chai, B. Zhao, S. Ghoshroy, and Q. W. Tang, "A highly efficient TiO_2@ZnO n-p-n heterojunction nanorod photocatalyst" *Nanoscale* **5**, 588 (2013).

[94] L. L. Ren, Y. P. Zeng, and D. L. Jiang, "The improved photocatalytic properties of P-type NiO loaded porous TiO_2 sheets prepared via freeze tape-casting" *Solid State Sciences* **12**, 138 (2010).

[95] H. T. Yu and X. Quan, "Nano-Heterojunction Photocatalytic Materials in Environmental Pollution Controlling" *Progress in Chemistry* **21**, 406 (2009).

[96] B. S. Liu, X. J. Zhao, N. Z. Zhang, Q. N. Zhao, X. He, and J. Y. Feng, "Photocatalytic mechanism of TiO_2-CeO_2 films prepared by magnetron sputtering under UV and visible light" *Surf. Sci.* **595**, 203 (2005).

[97] M. C. Toroker, D. K. Kanan, N. Alidoust, L. Y. Isseroff, P. L. Liao, and E. A. Carter, "First principles scheme to evaluate band edge positions in potential transition metal oxide photocatalysts and photoelectrodes" *PCCP* **13**, 16644 (2011).

[98] Y. Xu and M. A. A. Schoonen, "The absolute energy positions of conduction and valence bands of selected semiconducting minerals" *Am. Mineral.* **85**, 543 (2000).

[99] M. Long, W. M. Cai, J. Cai, B. X. Zhou, X. Y. Chai, and Y. H. Wu, "Efficient photocatalytic degradation of phenol over $Co_3O_4/BiVO_4$ composite under visible light irradiation" *J. Phys. Chem. B* **110**, 20211 (2006).

[100] Hailong Zhou, Yongquan Qu, Tahani Zeid, and Xiangfeng Duan, "Towards highly efficient photocatalysts using semiconductor nanoarchitectures" *Energy Environ. Sci.* **5**, 6732 (2012).

[101] Wenbo Hou and Stephen B. Cronin, "A Review of Surface Plasmon Resonance-Enhanced Photocatalysis" *Adv. Funct. Mater.*, early view online (2012).

[102] Zhijun Zhou, Mingce Long, Weimin Cai, and Jun Cai, "Synthesis and photocatalytic performance of the efficient visible light photocatalyst Ag–AgCl/BiVO4" *J. Mol. Catal. A: Chem.* **353–354**, 22 (2012).

[103] Feng Lin, Donge Wang, Zongxuan Jiang, Yi Ma, Jun Li, Rengui Li, and Can Li, "Photocatalytic oxidation of thiophene on $BiVO_4$ with dual co-catalysts Pt and RuO_2 under visible light irradiation using molecular oxygen as oxidant" *Energy Environ. Sci.* **5**, 6400 (2012).

[104] Suk Joon Hong, Seungok Lee, Jum Suk Jang, and Jae Sung Lee, "Heterojunction $BiVO_4/WO_3$ electrodes for enhanced photoactivity of water oxidation" *Energy Environ. Sci.* **4**, 1781 (2011).

[105] Juan Su, Xiao-Xin Zou, Guo-Dong Li, Xiao Wei, Chang Yan, Yu-Ning Wang, Jun Zhao, Li-Jing Zhou, and Jie-Sheng Chen, "Macroporous V_2O_5−$BiVO_4$ Composites: Effect of Heterojunction on the Behavior of Photogenerated Charges" *J. Phys. Chem. C* **115**, 8064 (2011).

[106] Mei-Li Guan, De-Kun Ma, Sheng-Wei Hu, Yan-Jun Chen, and Shao-Ming Huang, "From Hollow Olive-Shaped $BiVO_4$ to n−p Core−Shell $BiVO_4@Bi_2O_3$ Microspheres: Controlled Synthesis and Enhanced Visible-Light-Responsive Photocatalytic Properties" *Inorg. Chem.* **50**, 800 (2011).

[107] Hui Xu, Huaming Li, Chundu Wu, Jinyu Chu, Yongsheng Yan, Huoming Shu, and Zheng Gu, "Preparation, characterization and photocatalytic properties of Cu-loaded $BiVO_4$" *J. Hazard. Mater.* **153**, 877 (2008).

[108] L. Ge, "Synthesis and characterization of novel visible-light-driven Pd/$BiVO_4$ composite photocatalysts" *Mater. Lett.* **62**, 926 (2008).

[109] Lei Ge, "Novel Pd/$BiVO_4$ composite photocatalysts for efficient degradation of methyl orange under visible light irradiation" *Mater. Chem. Phys.* **107**, 465 (2008).

[110] Aiping Zhang and Jinzhi Zhang, "Synthesis and characterization of Ag/$BiVO_4$ composite photocatalyst" *Appl. Surf. Sci.* **256**, 3224 (2010).

[111] Shigeru Kohtani, Misa Tomohiro, Kunihiro Tokumura, and Ryoichi Nakagaki, "Photooxidation reactions of polycyclic aromatic hydrocarbons over pure and Ag-loaded $BiVO_4$ photocatalysts" *Applied Catalysis B: Environmental* **58**, 265 (2005).

[112] Hui Xu, Huaming Li, Chundu Wu, Jinyu Chu, Yongsheng Yan, and Huoming Shu, "Preparation, characterization and photocatalytic activity of transition metal-loaded $BiVO_4$" *Materials Science and Engineering: B* **147**, 52 (2008).

[113] Shao-Wen Cao, Zhen Yin, James Barber, Freddy Y. C. Boey, Say Chye Joachim Loo, and Can Xue, "Preparation of Au-$BiVO_4$ Heterogeneous Nanostructures as Highly Efficient Visible-Light Photocatalysts" *ACS Applied Materials & Interfaces* **4**, 418 (2011).

[114] A. P. Zhang and J. Z. Zhang, "Characterization and photocatalytic properties of Au/$BiVO_4$ composites" *J. Alloys Compd.* **491**, 631 (2010).

[115] X. F. Chen, Q. Luo, M. D. Han, O. K. Tan, M. S. Tse, and H. Huang, "Mechanochemical synthesis of nanostructured $Sr(Ti_{1-x}Fe_x)O_{3-\delta}$ solid-solution powders and their surface photovoltage responses" *J. Solid State Chem.* **189**, 80 (2012).

[116] X. Meng, L. Zhang, H. X. Dai, Z. X. Zhao, R. Z. Zhang, and Y. X. Liu, "Surfactant-assisted hydrothermal fabrication and visible-light-driven photocatalytic degradation of methylene blue over multiple morphological $BiVO_4$ single-crystallites" *Mater. Chem. Phys.* **125**, 59 (2011).

[117] A. L. Rogach, T. Franzl, T. A. Klar, J. Feldmann, N. Gaponik, V. Lesnyak, A. Shavel, A. Eychmuller, Y. P. Rakovich, and J. F. Donegan, "Aqueous synthesis of thiol-capped CdTe nanocrystals: State-of-the-art" *J. Phys. Chem. C* **111**, 14628 (2007).

[118] J. Kragten, L. G. Decnop-Weever, and P. Gründler, "Mixed hydroxide complex formation and solubility of bismuth in nitrate and perchlorate medium" *Talanta* **40**, 485 (1993).

[119] G. G. Briand and N. Burford, "Bismuth compounds and preparations with biological or medicinal relevance" *Chem. Rev.* **99**, 2601 (1999).

[120] A. P. Zhang and J. Z. Zhang, "Characterization of visible-light-driven $BiVO_4$ photocatalysts synthesized via a surfactant-assisted hydrothermal method" *Spectroc. Acta Pt. A-Molec. Biomolec. Spectr.* **73**, 336 (2009).

[121] Yongfu Sun, Changzheng Wu, Ran Long, Yang Cui, Shudong Zhang, and Yi Xie, "Synthetic loosely packed monoclinic $BiVO_4$ nanoellipsoids with novel multiresponses to visible light, trace gas and temperature" *Chem. Commun.*, 4542 (2009).

[122] Anna McLaren, Teresa Valdes-Solis, Guoqiang Li, and Shik Chi Tsang, "Shape and Size Effects of ZnO Nanocrystals on Photocatalytic Activity" *J. Am. Chem. Soc.* **131**, 12540 (2009).

[123] S. Li, Y. H. Lin, B. P. Zhang, J. F. Li, and C. W. Nan, "$BiFeO_3/TiO_2$ core-shell structured nanocomposites as visible-active photocatalysts and their optical response mechanism" *J. Appl. Phys.* **105**, 054310 (2009).

[124] Akihide Iwase and Akihiko Kudo, "Photoelectrochemical water splitting using visible-light-responsive $BiVO_4$ fine particles prepared in an aqueous acetic acid solution" *J. Mater. Chem.* **20**, 7536 (2010).

[125] J. W. Tang, Z. G. Zou, and J. H. Ye, "Effects of substituting Sr^{2+} and Ba^{2+} for Ca^{2+} on the structural properties and photocatalytic behaviors of $CaIn_2O_4$" *Chem. Mater.* **16**, 1644 (2004).

[126] Long, Cai, and Horst Kisch, "Visible Light Induced Photoelectrochemical Properties of n-$BiVO_4$ and n-$BiVO_4$/p-Co_3O_4" *J. Phys. Chem. C* **112**, 548 (2008).

[127] Noseung Myung, Sunyoung Ham, Seungun Choi, Yujin Chae, Whan-Gi Kim, Young Jin Jeon, Ki-Jung Paeng, Wilaiwan Chanmanee, Norma R. de Tacconi, and Krishnan Rajeshwar, "Tailoring Interfaces for Electrochemical Synthesis of Semiconductor Films: $BiVO_4$, Bi_2O_3, or Composites" *J. Phys. Chem. C* **115**, 7793 (2011).

[128] Hai-qing Jiang, Hiromitsu Endo, Hirotaka Natori, Masayuki Nagai, and Koichi Kobayashi, "Fabrication and efficient photocatalytic degradation of methylene blue over CuO/$BiVO_4$ composite under visible-light irradiation" *Mater. Res. Bull.* **44**, 700 (2009).

[129] A. Kudo and S. Hijii, "H_2 or O_2 evolution from aqueous solutions on layered oxide photocatalysts consisting of Bi^{3+} with $6s^2$ configuration and d^0 transition metal ions" *Chem. Lett.*, 1103 (1999).

[130] B. L. Zhu and X. Z. Zhao, "Study on structure and optical properties of Bi_2O_3 thin films prepared by reactive pulsed laser deposition" *Opt. Mater.* **29**, 192 (2006).

[131] E. J. Li, L. Chen, Q. A. Zhang, W. H. Li, and S. F. Yin, "Bismuth-Containing Semiconductor Photocatalysts" *Progress in Chemistry* **22**, 2282 (2010).

[132] W. Zou, W. C. Hao, X. Xin, and T. M. Wang, "Visible-Light Photocatalytic Degradation of RhB by Bi_2O_3 Polymorphs" *Chinese Journal of Inorganic Chemistry* **25**, 1971 (2009).

[133] Hongyan Deng, Weichang Hao, Huaizhe Xu, and Chunzhong Wang, "Effect of Intrinsic Oxygen Vacancy on the Electronic Structure of γ-Bi_2O_3: First-Principles Calculations" *J. Phys. Chem. C* **116**, 1251 (2011).

[134] Y. D. Shen, Y. W. Li, W. M. Li, J. Z. Zhang, Z. G. Hu, and J. H. Chu, "Growth of Bi_2O_3 Ultrathin Films by Atomic Layer Deposition" *J. Phys. Chem. C* **116**, 3449 (2012).

[135] S. Park, H. Kim, C. Lee, D. H. Lee, and S. S. Hong, "Synthesis of Very Straight Bismuth Oxide Nanowires by Using Thermal Evaporation of Bismuth Powders" *Journal of the Korean Physical Society* **53**, 1965 (2008).

[136] T. Takeyama, N. Takahashi, T. Nakamura, and S. Itoh, "Icicle growth of delta-Bi_2O_3 tips deposited on sapphire substrate by means of the carbothermal method" *Mater. Lett.* **60**, 3416 (2006).

[137] T. Takeyama, N. Takahashi, T. Nakamura, and S. Itoh, "Nucleation and growth of delta-Bi_2O_3 thin films on c-sapphire by means of chemical vapour deposition under atmospheric pressure" *J. Cryst. Growth* **277**, 485 (2005).

[138] Georg Waldner and Josef Krýsa, "Photocurrents and degradation rates on particulate TiO_2 layers: Effect of layer thickness, concentration of oxidizable substance and illumination direction" *Electrochim. Acta* **50**, 4498 (2005).

[139] Hongtao Yu, Xie Quan, Shuo Chen, Huimin Zhao, and Yaobin Zhang, "TiO_2–carbon nanotube heterojunction arrays with a controllable thickness of TiO_2 layer and their first application in photocatalysis" *Journal of Photochemistry and Photobiology A: Chemistry* **200**, 301 (2008).

[140] Leeor Kronik and Yoram Shapira, "Surface photovoltage spectroscopy of semiconductor structures: at the crossroads of physics, chemistry and electrical engineering" *Surf. Interface Anal.* **31**, 954 (2001).

[141] J. G. Yu, G. P. Dai, and B. B. Huang, "Fabrication and Characterization of Visible-Light-Driven Plasmonic Photocatalyst Ag/AgCl/TiO_2 Nanotube Arrays" *J. Phys. Chem. C* **113**, 16394 (2009).

[142] K. Awazu, M. Fujimaki, C. Rockstuhl, J. Tominaga, H. Murakami, Y. Ohki, N. Yoshida, and T. Watanabe, "A plasmonic photocatalyst consisting of sliver nanoparticles embedded in titanium dioxide" *J. Am. Chem. Soc.* **130**, 1676 (2008).

[143] M. Zayats, A. B. Kharitonov, S. P. Pogorelova, O. Lioubashevski, E. Katz, and I. Willner, "Probing photoelectrochemical processes in Au-CdS nanoparticle arrays by surface plasmon resonance: Application for the detection of acetylcholine esterase inhibitors" *J. Am. Chem. Soc.* **125**, 16006 (2003).

[144] L. L. Liang, X. G. Luo, X. Y. Lin, C. G. Xu, and Z. Zhao, "Preparation and Characterization of Fe-doped $BiVO_4$" in *Eco-Materials Processing and Design X*, edited by H. Kim, J. F. Yang, T. Sekino et al. (2009), Vol. 620-622, pp. 655.

[145] Xiao Huang, Xiaoying Qi, Yizhong Huang, Shaozhou Li, Can Xue, Chee Lip Gan, Freddy Boey, and Hua Zhang, "Photochemically Controlled Synthesis of Anisotropic Au Nanostructures: Platelet-like Au Nanorods and Six-Star Au Nanoparticles" *ACS Nano* **4**, 6196 (2010).

[146] Franklin Kim, Jae Hee Song, and Peidong Yang, "Photochemical Synthesis of Gold Nanorods" *J. Am. Chem. Soc.* **124**, 14316 (2002).

[147] S. W. Cao, J. Fang, M. M. Shahjamali, F. Y. C. Boey, J. Barber, S. C. J. Loo, and C. Xue, "Plasmon-Enhanced Hydrogen Evolution on Au-$InVO_4$ Hybrid Microspheres" *Rsc Advances* **2**, 5513 (2012).

[148] C. H. Tseng, M. J. Tambe, S. K. Lim, M. J. Smith, and S. Gradecak, "Position controlled nanowire growth through Au nanoparticles synthesized by galvanic reaction" *Nanotechnology* **21**, 165605 (2010).

[149] Vaidyanathan Subramanian, Eduardo E. Wolf, and Prashant V. Kamat, "Catalysis with TiO_2/Gold Nanocomposites. Effect of Metal Particle Size on the Fermi Level Equilibration" *J. Am. Chem. Soc.* **126**, 4943 (2004).

[150] H. Chen, S. Chen, X. Quan, H. T. Yu, H. M. Zhao, and Y. B. Zhang, "Fabrication of TiO_2-Pt coaxial nanotube array schottky structures for enhanced photocatalytic degradation of phenol in aqueous solution" *J. Phys. Chem. C* **112**, 9285 (2008).

[151] Byoung Koun Min, Jung Eun Heo, Na Kyoung Youn, Oh Shim Joo, Hyunjoo Lee, Jin Hyung Kim, and Hoon Sik Kim, "Tuning of the photocatalytic 1,4-dioxane degradation with surface plasmon resonance of gold nanoparticles on titania" *Catal. Commun.* **10**, 712 (2009).

[152] Chiu-Hsun Lin, Jiunn-Hsing Chao, Chun-Hsuan Liu, Jui-Chun Chang, and Feng-Chieh Wang, "Effect of Calcination Temperature on the Structure of a Pt/TiO_2 (B) Nanofiber and Its Photocatalytic Activity in Generating H_2" *Langmuir* **24**, 9907 (2008).

[153] Satyananda Kishore Pilli, Thomas E. Furtak, Logan D. Brown, Todd G. Deutsch, John A. Turner, and Andrew M. Herring, "Cobalt-phosphate (Co-Pi) catalyst modified Mo-doped $BiVO_4$ photoelectrodes for solar water oxidation" *Energy Environ. Sci.* **4**, 5028 (2011).

[154] D. K. Zhong, S. Choi, and D. R. Gamelin, "Near-Complete Suppression of Surface Recombination in Solar Photoelectrolysis by "Co-Pi" Catalyst-Modified W:$BiVO_4$" *J. Am. Chem. Soc.* **133**, 18370 (2011).

[155] K. J. McDonald and K. S. Choi, "A new electrochemical synthesis route for a BiOI electrode and its conversion to a highly efficient porous $BiVO_4$ photoanode for solar water oxidation" *Energy Environ. Sci.* **5**, 8553 (2012).

[156] X. F. Zhang, Y. B. Zhang, X. Quan, and S. Chen, "Preparation of Ag doped $BiVO_4$ film and its enhanced photoelectrocatalytic (PEC) ability of phenol degradation under visible light" *J. Hazard. Mater.* **167**, 911 (2009).

[157] B. Zhou, J. H. Qu, X. Zhao, and H. J. Liu, "Fabrication and photoelectrocatalytic properties of nanocrystalline monoclinic BiVO(4) thin-film electrode" *Journal of Environmental Sciences-China* **23**, 151 (2011).

[158] M. R. Silva, L. H. Dall'Antonia, L. V. A. Scalvi, D. I. Santos, L. O. Ruggiero, and A. Urbano, "Deposition and characterization of $BiVO_4$ thin films and evaluation as photoanodes for methylene blue degradation" *J. Solid State Electrochem.* **16**, 3267 (2012).

[159] Kazuhiro Sayama, Atsushi Nomura, Takeo Arai, Tsuyoshi Sugita, Ryu Abe, Masatoshi Yanagida, Takashi Oi, Yasukazu Iwasaki, Yoshimoto Abe, and Hideki Sugihara, "Photoelectrochemical Decomposition of Water into H_2 and O_2 on Porous $BiVO_4$ Thin-Film Electrodes under Visible Light and Significant Effect of Ag Ion Treatment" *J. Phys. Chem. B* **110**, 11352 (2006).

[160] H. Ye, J. Lee, J. S. Jang, and A. J. Bard, "Rapid Screening of $BiVO_4$-Based Photocatalysts by Scanning Electrochemical Microscopy (SECM) and Studies of Their Photoelectrochemical Properties" *J. Phys. Chem. C* **114**, 13322 (2010).

[161] S. P. Berglund, D. W. Flaherty, N. T. Hahn, A. J. Bard, and C. B. Mullins, "Photoelectrochemical Oxidation of Water Using Nanostructured $BiVO_4$ Films" *J. Phys. Chem. C* **115**, 3794 (2011).

[162] Hua Wang, Yusong Bai, Qiong Wu, Wei Zhou, Hao Zhang, Jinghong Li, and Lin Guo, "Rutile TiO_2 nano-branched arrays on FTO for dye-sensitized solar cells" *PCCP* **13**, 7008 (2011).

[163] Q. H. He, Z. X. Zhang, J. W. Xiong, Y. Y. Xiong, and H. Xiao, "A novel biomaterial - Fe_3O_4: TiO_2 core-shell nano particle with magnetic performance and high visible light photocatalytic activity" *Opt. Mater.* **31**, 380 (2008).

[164] B. P. Zhang, J. L. Zhang, and F. Chen, "Preparation and characterization of magnetic $TiO_2/ZnFe_2O_4$ photocatalysts by a sol-gel method" *Res. Chem. Intermed.* **34**, 375 (2008).

[165] H. M. Xiao, X. M. Liu, and S. Y. Fu, "Synthesis, magnetic and microwave absorbing properties of core-shell structured $MnFe_2O_4/TiO_2$ nanocomposites" *Compos. Sci. Technol.* **66**, 2003 (2006).

[166] L. Shi and D. Weng, "Formation of impurity bands in iodine cation substitutionally doped TiO_2 and its effects on photoresponse and photogenerated carriers" *Phys. Lett. A* **372**, 5901 (2008).

[167] Z. Q. Liu, X. Yan, W. Chu, and D. D. Li, "Effects of impurities containing phosphorus on the surface properties and catalytic activity of TiO_2 nanotube arrays" *Appl. Surf. Sci.* **257**, 1295 (2010).

[168] R. Long, N. J. English, and D. A. Mooney, "Electronic structures of N- and C-doped NiO from first-principles calculations" *Phys. Lett. A* **374**, 1184 (2010).

[169] M. Khan, J. N. Xu, N. Chen, and W. B. Cao, "First principle calculations of the electronic and optical properties of pure and (Mo, N) co-doped anatase TiO_2" *J. Alloys Compd.* **513**, 539 (2012).